UNIVERSITY OF BRASÍLIA – UnB

FACULTY OF TECHNOLOGY / FACULTY OF GAMA

PROGRAM IN INTEGRITY OF MATERIALS ENGINEERING

MICROSTRUCTURAL ANALYSIS AND MECHANICAL PROPERTIES
CHARACTERIZATION IN A SET OF COMMERCIAL NODULAR CAST IRON

DANIEL DE OLIVEIRA FERNANDES

ADVISOR: PROF. DR. CARLA TATIANA MOTA ANFLOR
CO-ADVISOR: PROF. DR. BESIM BARANOĞLU

UNIVERSITY OF BRASÍLIA – UnB

FACULTY OF TECHNOLOGY / FACULTY OF GAMA

MICROSTRUCTURAL ANALYSIS AND MECHANICAL PROPERTIES CHARACTERIZATION IN A SET OF COMMERCIAL NODULAR CAST IRON

DANIEL DE OLIVEIRA FERNANDES

ADVISOR: PROF. DR. CARLA TATIANA MOTA ANFLOR

CO-ADVISOR: PROF. DR. BESIM BARANOĞLU

MASTER THESIS IN INTEGRITY OF MATERIALS ENGINEERING

ISSUE: 100A/2022

BRASÍLIA/DF, APRIL 2022

University of Brasília – UnB
Faculty of technology / Faculty of Gama
Program in Integrity of Materials Engineering

MICROSTRUCTURAL ANALYSIS AND MECHANICAL PROPERTIES CHARACTERIZATION IN A SET OF COMMERCIAL NODULAR CAST IRON

Daniel de Oliveira Fernandes

Master's thesis submitted to the post graduated Program in Integrity of Materials Engineering at University of Brasília , as part of the requirements for obtaining a master's degree.

APPROVED BY:

PROF. DR. CARLA TATIANA MOTA ANFLOR
ADVISOR

PROF. DR. BESIM BARANOĞLU
CO-ADVISOR - METAL FORMING CENTER OF EXCELLENCE/ ATILIM UNIVERSITY

DR. ARIOSTO BRETANHA JORGE
EXAMINER - FGA/UnB

DR. GUILHERME FERREIRA GOMES
EXAMINER - INSTITUTO DE ENGENHARIA MECÂNICA/UNIFEI

Relatório (ata) de defesa de dissertação assinado eletronicamente pela banca avaliadora, via Sistema Eletrônico de Informações - SEI, documento 7903970, processo 23106.025824/2022-23.

Report (minute) of master thesis defense electronically signed by the examining board, via the Electronic Information System - SEI, document 7903970, process 23106.025824/2022-23.

BRASÍLIA/DF, APRIL 2022

REFERENCE

FERNANDES, D. DE O. (2022). Microstructural Analysis and Mechanical Properties Characterization in a Set of Commercial Nodular Cast Iron. Master's Thesis in Integrity of Engineering Materials, Publication 100A/2022, Postgraduate Program, Faculty of Technology, University of Brasília, Brasília, DF, 92p.

danieldeoliveirafernandes@gmail.com

Brasília, DF – Brazil

"Failure is just an opportunity to start again with more intelligence"
Henry Ford

Dedico esta dissertação a minha mãe, que esteve presente ao meu lado sempre e me ensinou o caminho certo a qual devo seguir. Que se tornou o meu anjo da guarda mais forte e me vigia onde ela estiver.

ACKNOWLEDGMENTS

AGRADECIMENTOS

Aos meus pais, Paulo e Ruth, por todo apoio e amor incondicional, não só durante o período de mestrado, mas em toda a minha vida, por ter me ensinado valores fazendo eu me tornar o homem que sou hoje.

À minha namorada Julia Lins que esteve presente em todos os momentos dessa jornada e me apoiou nos momentos mais difíceis.

A Deus por estar me vigiando e cuidando de cada detalhe.

À Santo Expedito que me deu forças para acreditar.

À minha família por sempre estar ao meu lado e me dar todo o suporte e carinho em momentos difíceis.

À minha orientadora Prof. Dr. Carla Tatiana Mota Anflor, por acreditar no meu trabalho e auxiliar, nos diversos momentos de dúvidas e dificuldades com a pesquisa.

Aos professores da graduação que contribuíram muito na minha formação e que foram minha inspiração para seguir uma carreira acadêmica.

Ao Grupo de Mecânica Experimental e Computacional (GMEC), pelas risadas e por terem me ensinado que é muito melhor trabalhar em equipe.

Aos amigos de que fiz durante o mestrado, especialmente a Beatriz, minha companheira de laboratório e pesquisas.

Aos meus amigos Rodrigo e Mauricio pelas conversas e alegrias vividas desde o nosso primeiro semestre da graduação e que felizmente perduraram até o presente momento.

À banca examinadora, pela disposição em avaliar este trabalho e que certamente contribuirá muito para sua melhoria.

À CAPES, à FAP-DF e ao DPG, pelo apoio financeiro que foram fundamentais no desenvolvimento deste trabalho.

Por fim, a todos que de alguma forma contribuíram para mais esta conquista.

Resumo

O ferro fundido nodular tem sido comumente aplicado na indústria e diversas aplicações de engenharia devido ao baixo custo de produção e a similaridade das propriedades mecânicas quando comparadas aos aços carbonos corriqueiramente utilizados. As propriedades mecânicas do ferro fundido nodular são extremamente dependentes da sua microestrutura e também das características dos nódulos de grafita. Desse modo o principal objetivo foi avaliar e caracterizar o ferro fundido nodular das classes GGG40, GGG 60 e GGG70, sem a presença de tratamentos térmicos. As amostras foram retiradas de blocos e barras sem utilizar o processo de fundição em bloco Y. As propriedades do material foram determinadas através testes mecânicos como ensaio de tração, dureza, efeito Bauschinger e fadiga de baixo ciclo. Foi executada por meio de microscopia ótica a análise da microestrutura do material, de forma a avaliar o padrão de grafita, e posteriormente a quantificação de cada fase presente na amostra. Com o intuito de auxiliar a análise microestrutural, uma rotina baseada em segmentação de imagem foi desenvolvida. A metodologia possibilitou avaliar a influência da microestrutura em relação à posição do espécimen no bloco fundido, e também comparar com as propriedades de corpos de prova retirados de barras circulares. Os resultados comprovaram que a microestrutura, principalmente a densidade de nódulos de grafita no material, tem efeito na resistência do material, sendo assim necessário um controle adequado do processo de fundição para garantir as propriedades especificadas. As propriedades mecânicas dos corpos de prova retirados diretamente do bloco e das barras sem a fundição do bloco em Y apresentaram resultados desconformes com as propriedades disponíveis nos padrões usuais e na literatura. Essa diferença reforça que os ferros fundidos podem sofre alterações mecânicas por conta de alterações no processo de fundição, confirmando a importância de averiguar as características do lote fundido antes da aplicação mecânica do material. Por fim a rotina desenvolvida para a análise da microestrutura foi capaz de quantificar as fases e as propriedades da grafita de cada corpo de prova analisado.

Palavras-chave: Ferro Fundido Nodular, Caracterização mecânica, Microestrutura, Análise de Imagem Computacional.

ABSTRACT

Nodular cast iron has been commonly applied in industry and many engineering applications due to the low production cost and the similarity of its mechanical properties to carbon steel. The mechanical properties of nodular cast iron are very dependent on its microstructure and also on the characteristics of the graphite nodules. In this sense, the main objective was to evaluate and characterise the nodular cast iron grades GGG40, GGG60 and GGG70 in the absence of heat treatment. In addition, specimens were obtained from casted bars and blocks without the Y-block casting process. Through mechanical tests such as tensile, Bauschinger effect and hardness tests, the material mechanical properties were determined. Additionally, the microstructure was analysed by optical microscopy with the support of computational image analysis for determination of the attributes of the graphite nodules and the quantification of each phase present in the microstructure of the nodular cast iron. The developed methodology made it possible to evaluate the influence of the microstructure in relation to the position of the specimen in the cast iron block. The properties of the specimens removed from circular bars were also compared. The results showed that the microstructure has a strong effect on the material's strength, especially the density of graphite nodules in the material. The mechanical properties of the specimens taken directly from the block and bars without the Y-block casting presented results that are not in accordance with the properties available in the usual standards and literature. This difference reinforces that cast iron can undergo mechanical changes due to changes in the casting process, confirming the importance of checking the characteristics of the cast batch before engineering application of the material. Finally, the routine developed for the microstructure analysis was able to quantify the phases and properties of graphite in each analysed specimen.

Keywords: Nodular Cast Iron, Mechanical characterisation, Microstructure, Computational Image Analysis.

Contents

List of Tables

List of Figures

LIST OF NOMENCLATURES AND ABBREVIATIONS

NCI Nodular Cast Iron

WCI White Cast Iron

GCI Gray Cast Iron

MCI Malleable Cast Iron

SF Shape Factor

RSF Roundness Shape Factor

CSF Compactness Shape Factor

SSF Sprericity Shape Factor

ESF Eccentricity Shape Factor

BE Bauschinger Effect

LCF Low Cycle Fatigue

1 INTRODUCTION

Nodular Cast Iron (NCI) has been an alternative to commercial carbon steels due to the similarity of their mechanical properties and the low production cost in relation to steel. NCI has good machinability and approximately 10% lighter than the steel (Karaca & Şimşir, 2019). According to Karaman & Çetinarslan (2010) the present NCI production cost varies at around 20% to 40% less than commercial steel. This type of iron has a lower production cost because of the synthetic melting process, which replaces some of the expensive pig iron with cheaper scrap iron. Normally silicon and carbon are added with the aim of obtaining a higher nodule number.

NCI is not a single material but a class of materials offering a wide range of properties obtained through microstructure control (Al-Ghonamy *et al.*, 2008). NCI presents the graphite in a crack-arresting nodule shape, making it ductile. The spherical shape tends to have a lower stress concentration ($\sigma_{max}/\sigma_{med} = 1, 7$)) while lamellar and flake graphite results in higher stress ($\sigma_{max}/\sigma_{med} = 5, 4$) (Kohout, 2001).

The mechanical properties of NCI are strongly dependent on the microstructure (Vaško *et al.*, 2019; De Santis *et al.*, 2008). The metal matrix can be composed mainly of ferrite, resulting in low strength values associated with high ductility and toughness values. In a ferritic matrix, NCI presents a strength limit of 350–450 MPa, associated with 10–22% elongation. Another composition is that the matrix is constituted by pearlite, which implies good mechanical strength values associated with relatively low ductility values. In a pearlitic matrix, the NCI strength limit can reach 900 MPa associated with 2% elongation, and, by then producing mixtures of ferrite and pearlite, different classes of cast iron are obtained, with diverse combinations of properties, each suitable for a specific application (Chiaverini, 2008). The adopted nomenclature in this work is the GGG-Grade, the grade number reefers to the material rupture limit according to the standard. For example, the GGG40 as the cast has a rupture limit of 400 MPa according to the NCI's standards.

Due to the combination of excellent properties, the NCI family has been increasingly applied in various engineering fields and has become a research material (Meena & El Mansori, 2012). Given the properties and machinability of this material, NCI has been replacing grey cast iron, malleable cast iron, cast and forged steel, and welded structures (Guesser, 2019).Typical applications of nodular cast iron mainly include components such as pulleys, shafts, sprockets, valves, and hydraulic components, pinions, gears, bearings, brake discs, brake calipers, and supports, crankshafts, camshafts, and suspension parts of vehicles, among others.

The NCI manufacturing process comprises many variables, each of which affects the mechanical properties of the final material. Graphite has low mechanical strength when compared to the metallic matrix (Goodrich, 2003). The presence of graphite can be regarded as a mechanical discontinuity and a stress concentration point in the matrix. In addition, the graphite shape also has a marked influence on the material's mechanical properties. All the aforementioned characteristics intensify the search for understanding the mechanical properties of NCI and their variations.

Çetinarslan & Karaman Genç (2014) investigated the mechanical properties depending on the cross-section thickness in GGG40 NCI. Šamec *et al.* (2011) analysed the Low Cycle Fatigue (LCF) behaviour of NCI GGG50 subject to high temperatures of 300℃ and 400℃, with application to railway brake disks.

The properties of NCI are strictly dependent on the material microstructure, size, shape, and nodule distribution, and the presence of defects resulting from the manufacturing process has a direct impact on the material properties. With great application in the industry, this material is commonly applied to components that are subject to compressive loads, since it has a high compressive capacity due to its graphite nodules, resulting in a compressive hydrostatic pressure, unlike grey cast iron. The use of NCI in the most varied engineering systems makes it necessary to carry out a more detailed study of the plastic strain behaviour and the presence of defects in this type of material. Guillemer-Neel *et al.* (1999) evaluate the cyclic deformations and Bauschinger effect in ductile cast iron, and determine that NCI is characterised by high internal stress levels and a non-usual hysteresis cycle.

The Bauschinger Effect (BE) is a significant mechanical behaviour related to the loading condition, where the yield stress limit of the material is changed when the strain direction is inverted (Lemoine & Aouafi, 2008). Plastic deformations could interfere in the use of an engineering component, causing permanent deflections. Furthermore, plastic strain can frequently generate residual tension that remains after unloading. This tension may entail an increase or decrease in material strength (Dowling, 2013).

NCI is more often applied in high cycle fatigue cases according to Lukhi *et al.* (2018). In the literature, there is a lack of material about LCF for nodular cast iron.

It is worth mentioning that several researches concern NCI obtained from Y-blocks or U-blocks, a different scenario from the small and medium foundries. Important engineering components are manufactured from casted materials, and with the increased use of NCI special attention is necessary to the mechanical and microstructural properties from components cast directly in blocks, bars, or in the final shape component. As is well known, NCI has a range of mechanical properties that vary greatly with the cast control, leakage temperature, cooling rates, chemical composition, and cast shape.

The mechanical properties of nodular cast irons are intimately related to their microstructure, and parameters such as the nodule count, nodularity, and phase content are preponderant factors in the final mechanical properties (Grenier *et al.*, 2014). Despite the mechanisms regarding the microstructure are well known in the literature, the academic community is aware

that the mechanical properties may vary widely away from the usual parameters specified in the standards. These deviations in mechanical and microstructure properties ensure that NCI becomes an open research subject.

A good support that has been used in microstructural analysis is image segmentation. Image processing techniques have been widely employed in many fields, such as robot automatisation (Greggio *et al.*, 2010), vehicle detection (Audebert *et al.*, 2017), medical procedures and diagnosis (Sund & Eilertsen, 2003; Filho *et al.*, 2019), and in the and in the analysis of mechanical materials (Bulgarevich *et al.*, 2018).

Image segmentation has an auxiliary purpose in the microstructural characterisation, and generally the mechanical material analysis involves microstructure characterisation done manually through optical microscopes. The computational image processing method has assisted in the characterisation of the microstructure of NCI and other materials (de Albuquerque *et al.*, 2009), and some software is devoted to this type of analysis. The influence of the microstructure on the NCI mechanical properties has therefore led researchers to analyse this material through computational image analysis.

Image segmentation allows the measurement, count, and size of the graphite nodules. Segmentation based on thresholding of greyscale images is possible to binarise the image. In many cases, this is enough for evidencing the domains (Sparavigna, 2017). Computational image analysis can be a robust tool with the capacity to define the cast iron class also in the presence of dust, scratches, and measurement noise (De Santis *et al.*, 2017).

The present work aims to present a comprehensive study concerning the mechanical behavior of commercial NCI GGG40, GGG60, and GGG70, targeting the Brazilian industry problem of large variations in mechanical properties of the obtained cast iron. As aforementioned, the nodular cast irons present a wide variety of mechanical properties due to several factors resulting from the casting process. In this sense, the efforts rely on the material characterization of blocks and bars from the same batch. The study was carried out through mechanical tests and microstructural analysis using micrograph images with the aid of digital image segmentation.

1.1 OBJECTIVES

1.1.1 General Objective

This work has the main objective of characterising commercial nodular cast iron GGG40, GGG60, and GGG70 in the absence of heat treatment by evaluating the mechanical properties through mechanical tests and correlating these with microstructure parameters such as graphite nodule counting, size, and shape.

1.1.2 Specific Objectives

In the development of this work, some specific objectives were necessary in order to achieve the main objective of the research.

1. Perform mechanical tests such as tensile, Bauschinger effect, and hardness tests in order to obtain information on a great number of mechanical properties.

2. Analyse the microstructure of commercial nodular cast iron available in block and round bars and the impact of the specimen position on the microstructure.

3. Identify and count the graphite nodules and characterise the nodule distribution, size, and shape of graphite particles.

4. Evaluate the nodule distribution in relation to the position of the specimen in the cast iron block or bar.

5. Investigate the graphite nucleation in round bars and evaluate the graphite nodules along the cross-section area by counting and characterising the size and shape. In addition, the hardness test was also performed at certain points.

1.2 ORGANISATION OF TEXT

This work is divided into six chapters. The first presents a brief introduction to the principles, concepts and the main contributions in this research field. It also introduces the main and specific objectives.

The second chapter introduces the concepts of the plastic deformation behaviour and the phenomenon that involves cyclic stress–strain behaviour.

Chapter three discusses the cast iron generalities and presents the concepts about nodular cast iron and its characteristics as a material.

Chapter four discusses the methods used in the development of this work, and presents the mechanical tests and the configurations used in the tests. It presents the methodology developed for the metallographic analyses on the nodular cast iron and how the computational image analysis was performed, presenting the model developed by the author.

Chapter five presents the results and discussion.

Finally, in chapter six, the conclusions of the work are presented, and some considerations for future works are proposed.

2 PLASTIC DEFORMATION BEHAVIOR

This chapter has the objective to present the principle concepts of the plasticity theory and cast iron which can facilitate the comprehension about the experimental tests used on this work development.

2.1 THE CYCLIC STRESS-STRAIN BEHAVIOUR

The stress strain behaviour could be described by the typical phenomenon: Baushinger effect, cyclic hardening/softening, masing or non masing behaviour, non proportional hardening and ratcheting.

The cyclic hardening or softening behaviour is described by the evolution of the stress amplitude in a strain controlled cyclic test. The material will be hardened when the stress amplitude become higher over the time and the softening is opposite behaviour. The stress amplitude will be less over the time. Most materials have cyclic hardening or softening. Material such as stainless steels and pure cooper, exhibit very significant hardening while some other materials display less significant. As a rule soft material cyclically hardens and hard materials cyclically softens. As described by Jiang & Zhang (2008) the hardening or softening behavior depends on the material, loading magnitude and loading history.
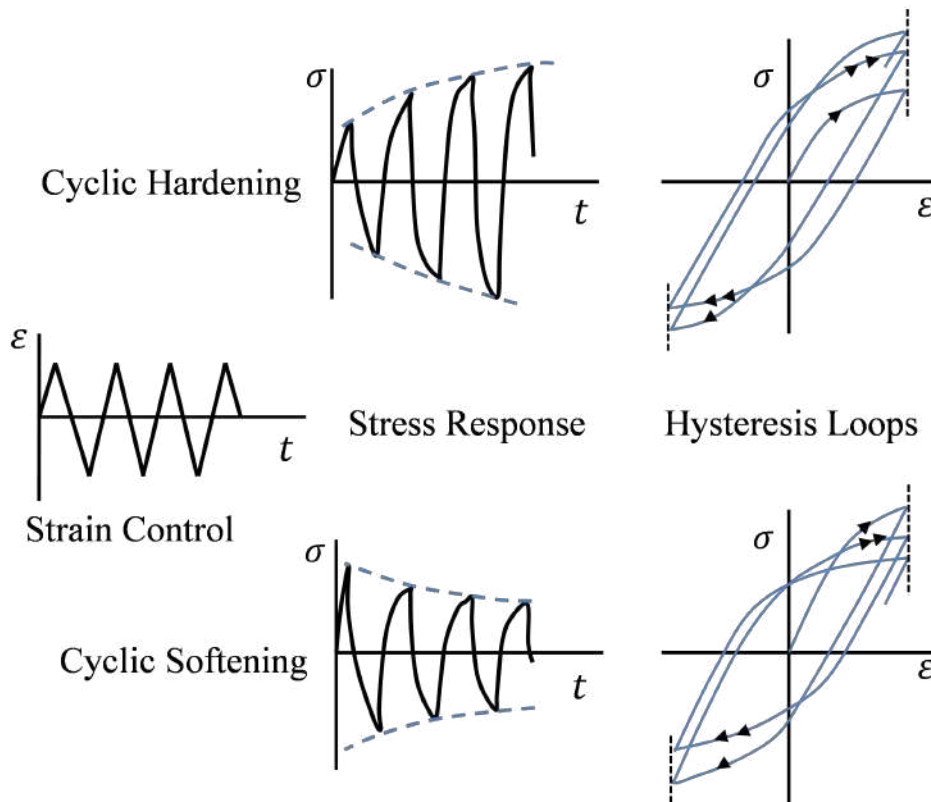
Figure 2.1. Completely reversed controlled strain test and two possible stress responses, cycle-dependent hardening and softening (Dowling, 2013) (From [Landgraf 70]).

Generally, nodular cast iron are submmited to heat treatment by the industry in order to increase the strenght and improve the behavior when cyclic load are under consideration. Among classic heat treatments an more often employed to NCI one can cite the following process: austempering, quenching and tempering, annnealing, austenitizing and normalizing. Annealed materials have a small amount of discordance, with the plastic strain the amount of the discordance increase fast. The movement of discordance creates a barrier that makes the movement of future discordance more difficult causing the material hardening as far as the load is acting in the material. In contrast the materials hardened by mechanical process have great amount of discordance. The cyclic strain causes in this type of material the rearrangement of the discordance structures, making the discordance number decreases and causing softening (Ye *et al.*, 2006). Dynamic recovery is related to the ability of discordance to migrate between one slip plane and another. This mechanism is stimulated by the movement of structures during cyclic loading (Plumtree, 1987).

2.2 PLASTICITY THEORY

The plasticity theory is defined by de Souza Neto *et al.* (2008) where plasticity theory provides a general description of the constitutive evolution of the material behavior. Generally, plasticity theory is the field of mechanics that deals with the calculation of stress and strain in ductile materials that have been permanent deformed by a set of applied forces. Almost all real

materials will undergo permanent deformation, which remains after removal of load. In metals the permanent deformations will usually occur when the stress reaches the critical value called yield stress.

An easy way to explain the principles of plasticity theory is from a strain-stress graph, provided from a tensile test as illustrated in figure 2.2. The specimen in tensile test is subjected to traction forces until the specimen failure.
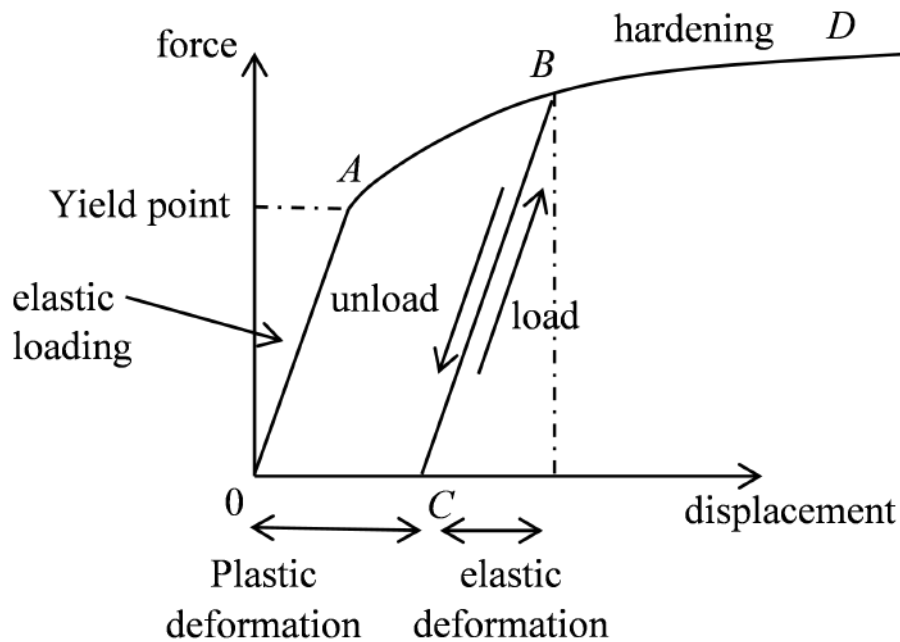
Figure 2.2. A generalized force-displacement curve for tension test of metallic materials (Kelly, 2020).

In the elastic zone, the behavior for most engineering materials is linear. After point A the material reaches the yield strength and becomes the plastic flow behavior. Increase the load is necessary to maintain the plastic flow, this phenomenon is known as work hardening or strain hardening. In some materials, the behavior after an initial plastic flow and hardening, the force-displacement curve decreases, and the material are in the softening process. If the specimen is unloaded from a plastic strain B, the strain will return along the BC patch, parallel to the elastic original line. This is an elastic recovery, the strain which remains in the specimen is the permanent strain. If the material has been loaded again the stress-strain curve will follow the CB patch until it reaches the plastic zone again. Addiction loading after the point B will cause the curve to follow the BD patch.

At last, establish that the basic components of an elastoplastic constitutive model are expressed by Hooke's law Eq. 2.1 and additive decomposition of deformations Eq. 2.2. Being complimented by a yield criterion and a plastic flow rule, which defines the evolution of plastic deformation; and a hardening law, which characterizes the evolution of the yield limit.

$$\sigma = \mathbb{D}^e : \varepsilon^e \tag{2.1}$$

7

Where σ is the Cauchy stress tensor, $\mathbb{D}$ is the material constitutive matrix tensor and ε^e is the elastic part of the strain tensor.

$$\varepsilon = \varepsilon^e + \varepsilon^p \qquad (2.2)$$

Where ε of the tensor of the deformations being, its elastic and plastic portions expressed respectively by ε^e and ε^p

2.3 IDEAL PLASTICITY

A description of perfect plastic hardening is when the material does not allow strain hardening. This means that the yield stress level does not have any relation with the applied strain level. The yield field remains fixed independent from the load applied, in this case the elastoplastic modulus will be null (de Souza Neto *et al.*, 2008).
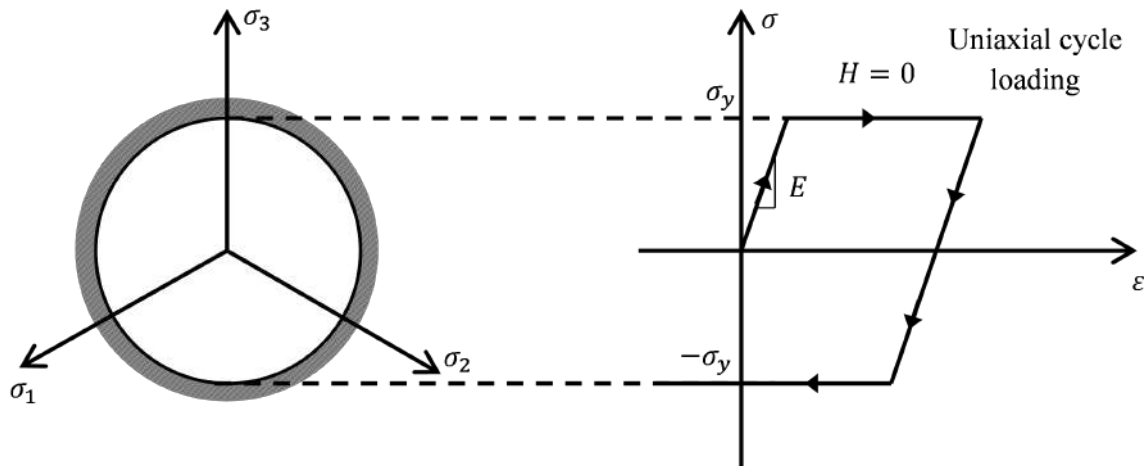
Figure 2.3. Ideal plasticity description. (Adapted from Lou & Yoon (2017)).

Where H is the hardening coefficient and E is the Young's modulus, σ_1, σ_2 and σ_3 is the principles tension plane. For ideal plasticity the hardening coefficient remains null, with no evolution in the initial flow field, regardless of the applied deformation.

2.4 ISOTROPIC HARDENING

Even though most materials exhibit a strong, hardening induced anisotropic, the isotropic hardening representation is very often used, because of simplicity and is a very good representation in case of proportional loading.

Isotropic hardening is used to described the deformation hardening behaviour for a material under monotonic loading (Lee & Barkey, 2012). The isotropic hardening occurs when the evolution of the yield surface corresponding to the expansion of the initial yield surface without

translation. The uniaxial model described in figure 2.2 is a typical representation of isotropic hardening.
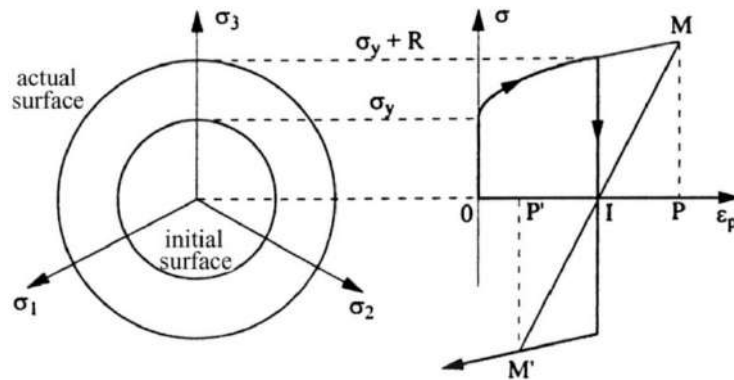
Figure 2.4. Schematic representation isotropic hardening (Chaboche, 2008).

In the isotropic model the elastic domain expands equal in tension and in compression during the plastic flow as represented by figure 2.4 . The isotropic hardening model does not take into count the baushinger effect. If only room temperature is considered, the size of the yield surface is governed by the accumulated plastic work or accumulated plastic strain.

$$\sigma_{eq} = K p^{\frac{1}{m}} \dot{p}^{\frac{1}{n}} \tag{2.3}$$

Where K is the initial value of the drag stress, p is the accumulated plastic strain, and n is the strain hardening exponent.

2.5 KINEMATIC HARDENING

Kinematic hardening assumes neither expansion/contraction nor distortion of the yield surface in stress space. Rather, the yield surface translates to accommodate the latest loading increment of stress (Pattillo, 2018). A very useful schematic way to represent anisotropic hardening is that of linear kinematic hardening in which the elastic domain retains a constant size but moves about in the stress space translation, the center of subsequent yield surface represent the internal stress of the neutral state or back stress (Lemaitre & Chaboche, 1990).

The Bauschinger effect is a phenomenon that happens subject cyclic loading. The reversal loading influence the yield limit in the opposite direction of the initial load direction which ensure that the yield surface being constantly translating.

Figure 2.5 shows a description of the Kinematic hardening model on the uniaxial stress-strain curve.

9
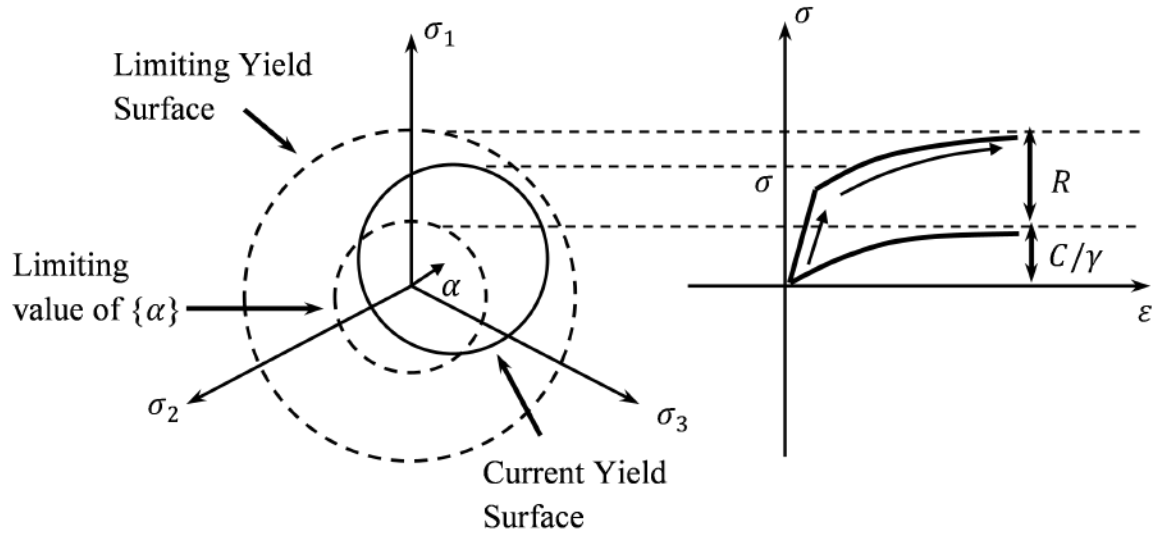
Figure 2.5. Kinematic hardening. (Adapted from Chaboche (2008)).

In the kinematic hardening the stress changes due to the translation of the yield surface, the uniaxial behavior that produces Bauschinger effect can be modeled with kinematic hardening (Pattillo, 2018).

The yield function for linear kinematic hardening can be represented by:

$$F = \sqrt{\frac{3}{2}(\{s\} - \{\alpha\})^T [M](\{s\} - \{\alpha\})} - \sigma_y \tag{2.4}$$

The back stress is linearly related to plastic strain via:

$$\Delta\alpha = \frac{3}{2}C\Delta\epsilon_{pl} \tag{2.5}$$

Where s is the deviatoric stress, σ_y is the uniaxial yield stress, and α is the back stress (location of the center of the yield surface).

2.6 BAUSCHINGER EFFECT

The Bauschinger effect is an important mechanical phenomenon that is occurs in metallic materials. This phenomenon is associated to a specimen when is subjected to a traction load followed by a compression load (Lemaitre & Chaboche, 1990). According to Mataya & Carr (1983) if the load is sufficient to cause a plastic deformation in one direction, re-straining the material in the opposite direction result in a lower elastic limit than would have been tested for re-straining in the same direction. This loading sequence results in higher yield stress in traction (hardening) but softening in compression.

Figure 2.6 shows a scheme for the Baushinger effect. The yield strength under tension is σ_{ot}, if the same material is ductile and have been tested for compression, the yield strength

under compression would be σ_{oc}. When the specimen is subjected to tension followed by compression, the yield strength will change in reversal loading A.
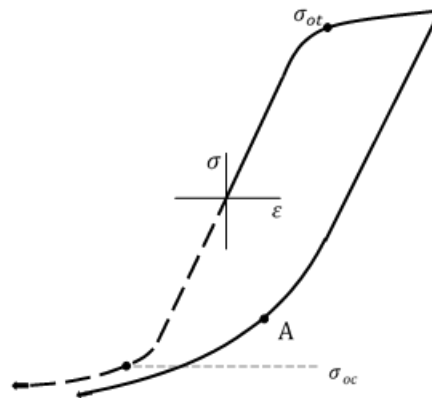
Figure 2.6. Baushinger effect description (Dowling, 2013).

The Bauschinger effect occurs due to the presence of residual stress resulting from the manufacturing process. The pile-up and discordance of grain boundaries would facilitate the dislocation of discordance in the opposite direction to the initial deformation. As the deformations occurs the dislocation will be accumulated. In softening local back stresses could be remaining in the material, what helps the dislocation at the reversal direction, and consequently the yield strength of the material is lower.

In hardening, the reversal loading direction could produces dislocation with opposite signal from the same source that produce the slip-causing dislocation in the initial direction. Discordance with opposite signal generates by the reversal loading would annul the discordance initially formed, so the hardening is associated to increase the displacement density. Reduce the dislocation number means reduces the strength, the yield stress is results lower in the opposite direction compared to the strain obtained if the test had been continued in the initial direction (Han *et al.*, 2005).

Wilson (1965) states that in a single phase alloys, exhibit little permanent softening. In contrast, two-phase alloys, like iron containing cementite particles, showed a large amount of softening, and the softening was proportional to the volume of fraction of the second phase and to the inverse of second phase particle size, as related by Mataya & Carr (1983).

The characterization of Bauschinger effect can be carried out through the equation the Eq. 2.6 and Eq. 2.7. Where BE is the Bauschinger Effect and BEF is the Bauschinger Effect Factor.

$$BE = \frac{|A| - |\sigma_o|}{|A|} \tag{2.6}$$

$$BEF = \frac{|\sigma_o|}{|A|} \tag{2.7}$$

Equation 2.6 regards to the difference between the stress at reversal point and the yield stress

at the reversal loading. A 0.05 % offset strain was used to determine the yield stress on reversal, because it is provide a better correlation than the conventional 0.2% (Han *et al.*, 2005).

The Eq. 2.6 and Eq. 2.7 allow quantifying the Bauschinger effect and it is important to remark as closer σ_{ot} (yielding stress) and A (stress at reversal point) lower will be the magnitude of the Bauschinger effect. In spite of Eq. 2.6 and Eq. 2.7 characterizes the Baushinger effect, both are similar at the end.

3 CAST IRON

3.1 GENERAL ASPECTS ABOUT CAST IRON

Among the iron-carbon alloys cast iron represents a fundamental alloy group for the industry. Due to the mechanical characteristics of the cast iron as well the addition of alloy elements, application of heat treatments and the development of the nodular cast iron It is have been viable the application of this material on occasions that previously were exclusive to steel. In this way the study of the cast iron and nodular cast iron are fundamental to mechanical engineering that have one more option in the sense of material selection for several applications (Chiaverini, 2008).

By the iron-carbon phase diagram, the iron casting alloys is usually defined as Fe-C alloys that have more than 2,0% of carbon in the material composition. The silicon has significant influence because of the presence and high concentration in this alloy. Silicon is often present at levels greater than carbon, being the cast iron alloy formed by Fe-C-Si.

Chiaverini (2008) in his book "Aços e Ferros Fundidos" defines cast iron as:

> *"Cast iron is the Fe-C-Si alloy with carbon level usually higher than 2%, in superior quantity to be retained in solid solution in the austenite so as to produce partially free carbon in lamellar or nodular graphite shape".*

The cast iron is classified in different types according to the graphite shape and the matrix structure that can be ferritic, perlitic, ferritic-perlitic, austenitic, martensitic (Rebouças *et al.*, 2016). Each matrix will generate different properties and distinct material classes (Callister & Rethwisch, 2009). According to Guesser (2019) the cast iron classes could be characterized in the following types: gray cast iron, white cast iron malleable cast iron, graphite compacted cast iron and nodular cast iron.

> **Gray Cast Iron (GCI)** - The fracture of gray cast iron shows a dark color, characterized by present carbon and silicon as essential alloy elements and a structure were a large portion of carbon is in free state (lamellar graphite) and other portion is the combined state Fe_3C.
>
> The gray cast iron is commonly used in industrial applications, because of the low production cost (20% - 40 % less than steel), corrosion resistance, machinability and low melting point. This material is widely used in the machines components manufacturing such as, disk brake rotors, gear bearings and hydraulic valves (Behnam *et al.*, 2010).

The microstructure of GCI is characterized by graphite lamellas dispersed into the ferrous matrix. Figure 3.1 shows the microstructure of the gray cast iron.
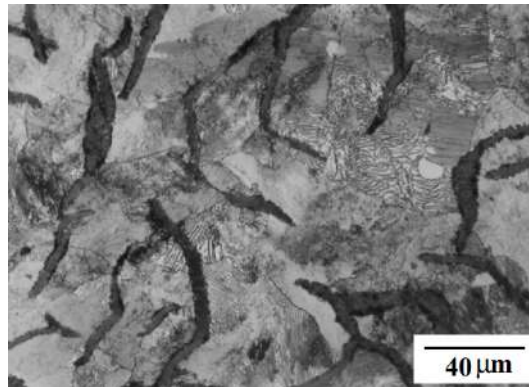
Figure 3.1. Gray cast iron microstructure (Yescas-González, 2001).

White Cast Iron (WCI) - Characterized by present carbon an silicon as primary alloy elements, shows a clear color when fractured. The WCI is usually applied in situation that requires a high abrasion resistance as in the mining and mineral ore processing industry, ball mills and cement mixers (Mohammadnezhad *et al.*, 2013).The structure of white cast iron have the carbon in a combination form (Fe_3C) due to the manufacturing conditions and less silicon amount. Due to the high amount of iron carbide, this material have high abrasion resistance although does not have good machinability. Figure 3.2 shows the microstructure of the white cast iron.
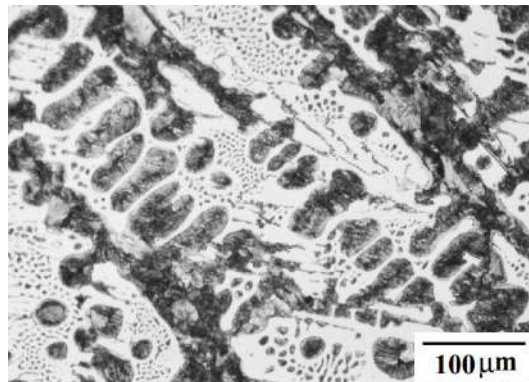
Figure 3.2. White cast iron microstructure (Yescas-González, 2001).

Malleable Cast Iron (MCI) - Malleable iron is produced by first casting the iron as a white iron and then heat treating the white cast iron to convert the iron carbide into the irregularly shaped nodules of graphite instead lamellar graphite shapes (Keough & Hayrynen, 2017). Over the years the industry in Europe and in United States were obtaining high technology in the development of MCI. In Europe the malleabilization process is distinguished by a structure that contain ferrit and carbon in the combined state. In the American process have an uniform ferritic structure with free carbon nodules (Chiaverini, 2008). Figure 3.3 shows the microstructure of the malleable cast iron.

14
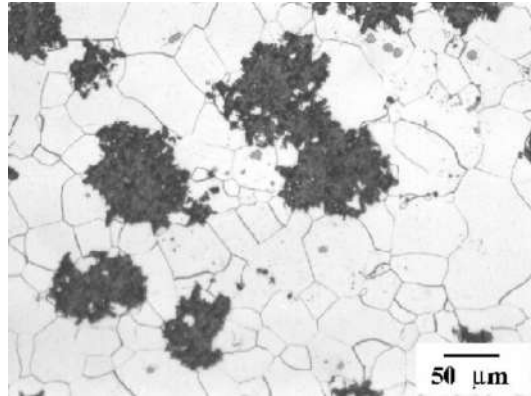
Figure 3.3. Malleable cast iron microstructure (Yescas-González, 2001).

Compacted graphite cast iron - Characterized by the vermicullar graphite shape, the compacted graphite iron as the nodular cast iron require addition of others specifics elements. In compacted graphite iron the addition of titanium decrease the formation of spherical graphite (Chiaverini, 2008). This type of iron could be considered as an intermediary material between gray cast iron and nodular cast iron. In relation to the GCI the vermicullar cast iron have higher strength and better surface finish. In relation to the NCI the VCI have higher shock absortion and superior thermal conductivity. The compacted graphite cast iron is often applied in exhaustion manifold and cylinder block of new generation diesel engines (Guesser, 2019). Figure 3.4 shows the microstructure of the compacted graphite cast iron.
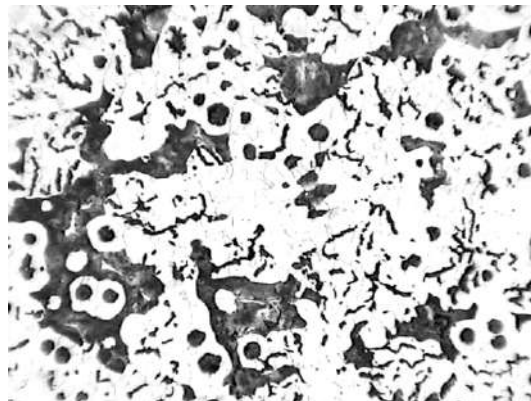
Figure 3.4. Compacted graphite cast iron microstructure (Mocellin *et al.*, 2004).

Nodular cast iron (NCI) - Also called ductile iron the nodular cast iron present graphite in spherical shape. Because the spheroids interrupt the matrix much less than graphite flakes, nodular cast iron has higher strength and toughness than gray cast iron. Also because the free carbon in graphite spherical shape the nodular iron have good ductility. The formation of nodules or spheroids occurs when eutectic graphite separates from the molten iron during solidification. The separation of graphite in nodular form is similar to separation of graphite in gray cast iron except that the additives facilitate the graphite to take nodular shape (Singh, 2016). Figure 3.5 shows the microstructure of the nodular cast iron.

15
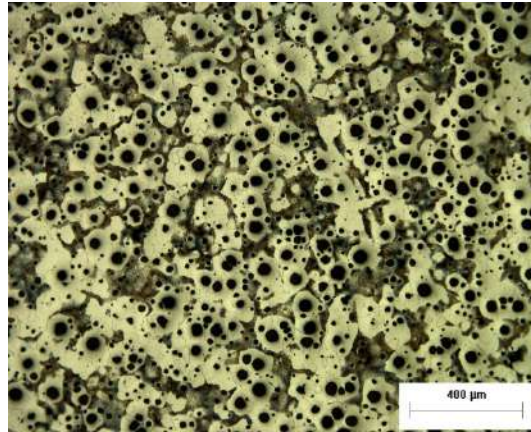
Figure 3.5. Nodular cast iron microstructure (Koerich & Al-Rubaie, 2012).

The chemical composition range of the main cast iron types without alloy elements is indicated in table 3.1

Table 3.1. Chemical composition range of common cast iron types.

| Type | Chemical element % | | | | |
	C	Mn	Si	S	P
White	1,8 - 3,6	0,5 - 1,9	0,25 - 0,80	0,06 - 0,20	0,06 - 0,20
Malleable	2,2 - 2,9	0,9 - 1,9	0,15 - 1,20	0,02 - 0,20	0,02 - 0,20
Gray	2,5 - 4,0	1,0 - 3,0	0,20 - 1,00	0,01 - 0,03	0,01 - 0,10
Nodular	3,0 - 4,0	1,8 - 2,8	0,10 - 1,00	0,01 - 0,03	0,01 - 0,10

The cast iron elastic modulus covers a wide range of values from 60 GPa to 180 GPa depending mainly on the graphite characteristics, as size, shape, and particles number by area unit. (Wolfensberg, 1987 apud (Guesser, 2019)). The effect of graphite characteristic could be considered through the dimensionless parameter shown in Eq. 3.1.
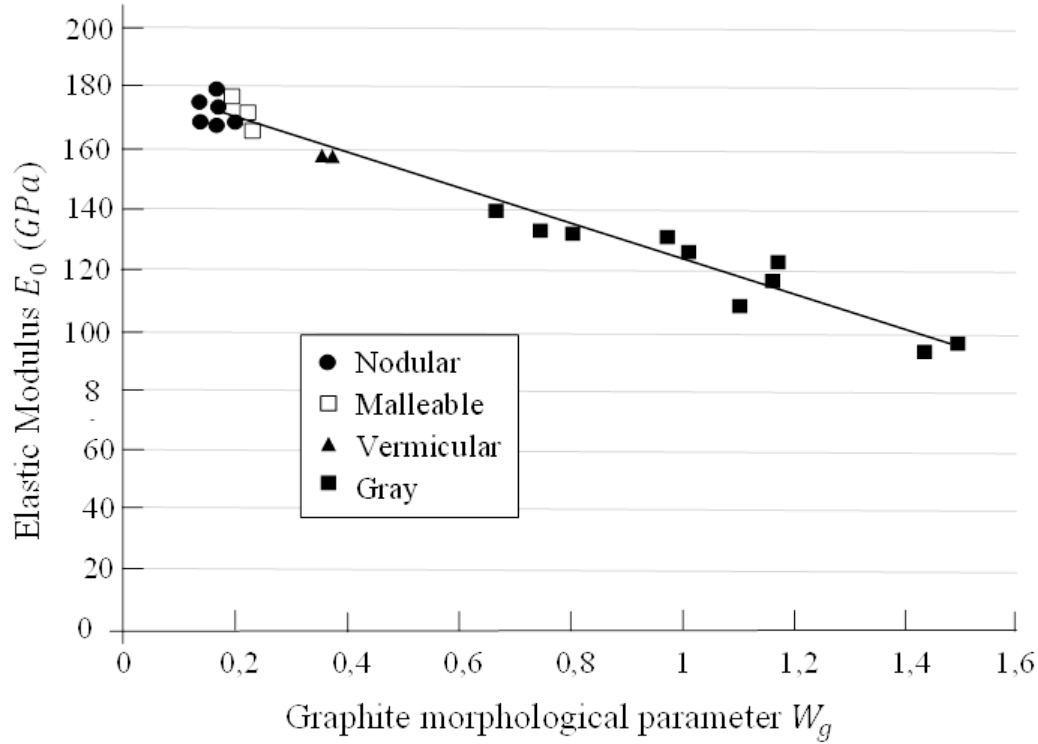
Figure 3.6. Elastic modulus as a function of graphite morfological parameter (Guesser, 2019).

$$W_g = (S_{max})^2 * N_a \tag{3.1}$$

where $Smax$ is the greater measure of graphite particles dimension, and Na is the number of graphite particles by area unit. This effect could be applied for several cast iron types with different matrix, and could be described by Eq. 3.2.

$$E_0 = 190 - 60 * W_g \tag{3.2}$$

Cast iron has a singular characteristic that is the effect of geometry thickness on mechanical properties. This effect is seen with severe impact on gray cast iron but is also noted in other cast iron types. In nodular cast iron with the increased section thickness occurs the cold rate decrease in solidification. The graphite nodules get bigger but due to the spherical shape, the effect is not so critical about the mechanical properties (Guesser, 2019). However, the separation of the alloy elements occurs making the properties in the microstructure heterogeneous, and mainly segregation of impurities, affect the nodularity of the particles in the thermal centers of the parts.

This effect is evaluated in some works, Guzel Guzel *et al.* (2014) concluded that the ferritic matrix has increased, nodule count and hardness has decreased with higher section thickness. Other authors (Megahed *et al.*, 2019; Bočkus *et al.*, 2008) reached similar conclusions, although Megahed Megahed *et al.* (2019) has analyzed compacted graphite cast iron. The

17

separation of carbides (Cr, Mo, Mn) can also lead to the formation of intercellular carbides, mainly reducing elongation. The standards EN 1563 and ISO 1083 provide for the variation of mechanical properties (resistance limit, elastic limit, and elongation) with increasing thickness.

3.2 NODULAR CAST IRON

Nodular cast iron, also known as ductile cast iron, has been a material widely used in industry today, which is characterized by ductility, toughness and mechanical resistance (Souza *et al.*, 2014). These characteristics are linked to the mechanical strength of the material. Nodular cast iron has a higher yield limit than gray iron, malleable iron and even ordinary carbon steels without the addition of an alloying element. The nodular cast iron is a Fe-C-Si alloy were the carbon is in spherical shape. Due to the high amount of carbon the graphite particles are founded in the metallic matrix microstructure. The nodular term refers to the graphite shape that is obtained by the addiction of some alloy elements, as magnesium.

In comparison to the GCI that have lamellar graphite shape, the spherical shape of the graphite in NCI raise the mechanical strength and toughness. In this way the NCI can be compared with many steel classes. In addition, the NCI manufacturing is cost-effective, what allows a high flexibility in the production, which makes NCI being widely used in the industry (Hütter *et al.*, 2015).

The mechanical properties of NCI with ferritic and perlitic matrix are affected by the variables showed in figure 3.7.

The mechanical properties of NCI with ferritic and perlitic matrix are affected by the variables showed in figure 3.7. For the NCI the first variable to be considered is the graphite shape. Graphite without spherical shape, in particular different from shape V and VI in figure 3.8, contribute to mechanical strength and elongation reduction.
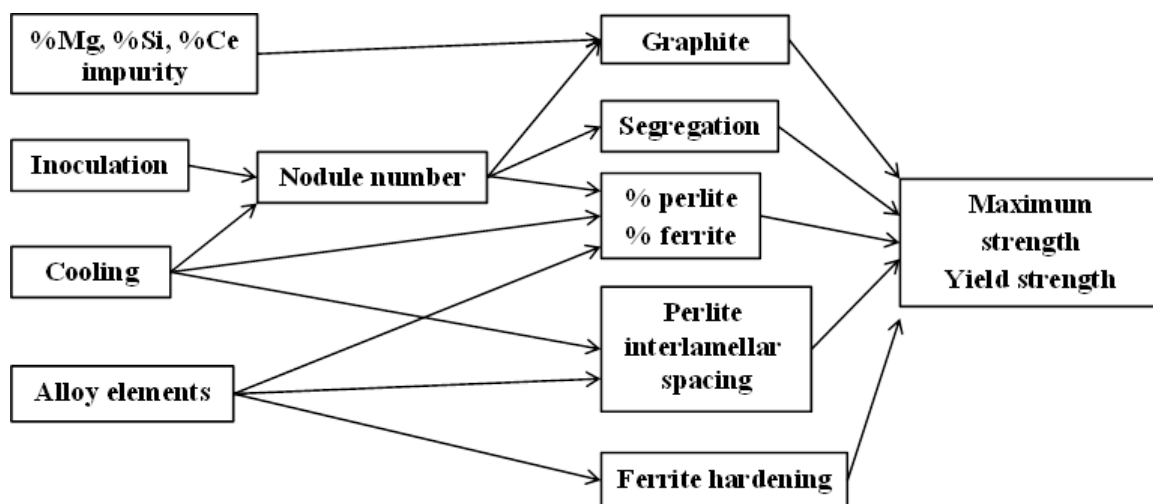
Figure 3.7. Microstrucutre variable effects in the nodular cast iron mechanical properties with ferritic perlitic matrix (Guesser, 2019).
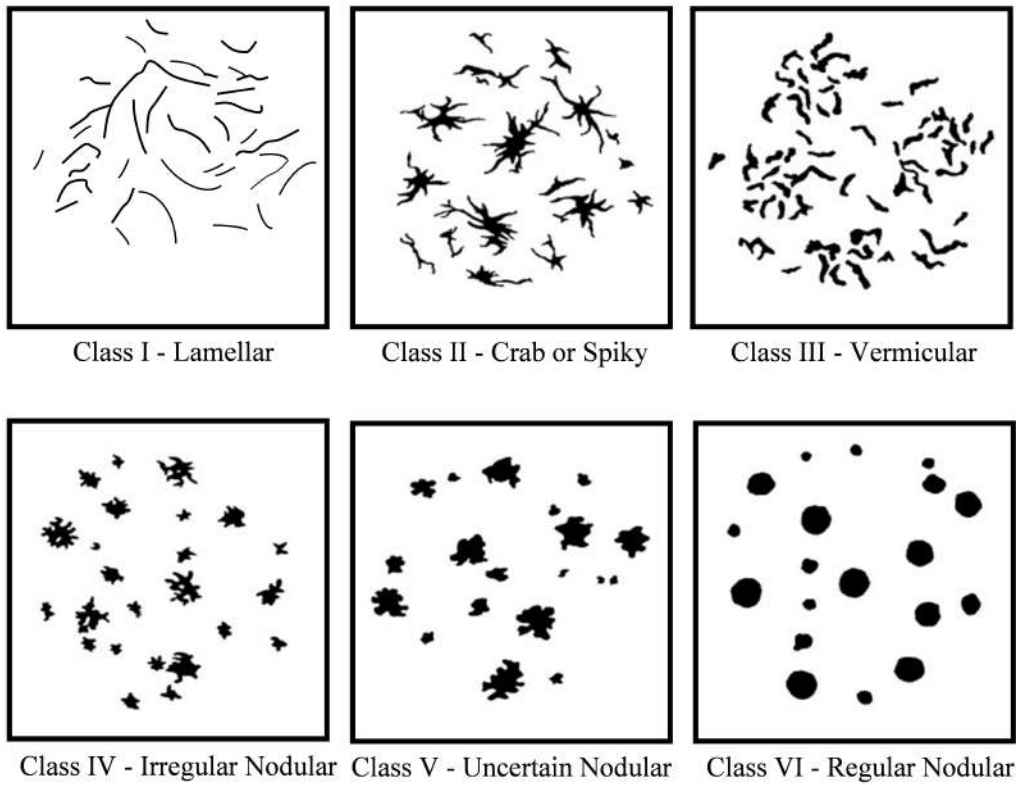
Figure 3.8. Graphite types found in Iron Castings

Since the graphite shape interferes with the nodular cast iron strength. Sofue *et al.* (1978) report that the nodularity, or in other words the percentual particles with a spherical shape, affects the material mechanical properties. The lower the nodularity percentage the lower the strength linked to it the size of the nodule will also have an impact, since the greater the average size of the graphite nodules, the lower the resistance will be. This corroborates with more current works such as Gangasani (2007); hua Wang *et al.* (2019); Benedetti *et al.* (2019). Figure 3.9 exemplifies the interference of graphite in the mechanical properties of nodular cast iron.
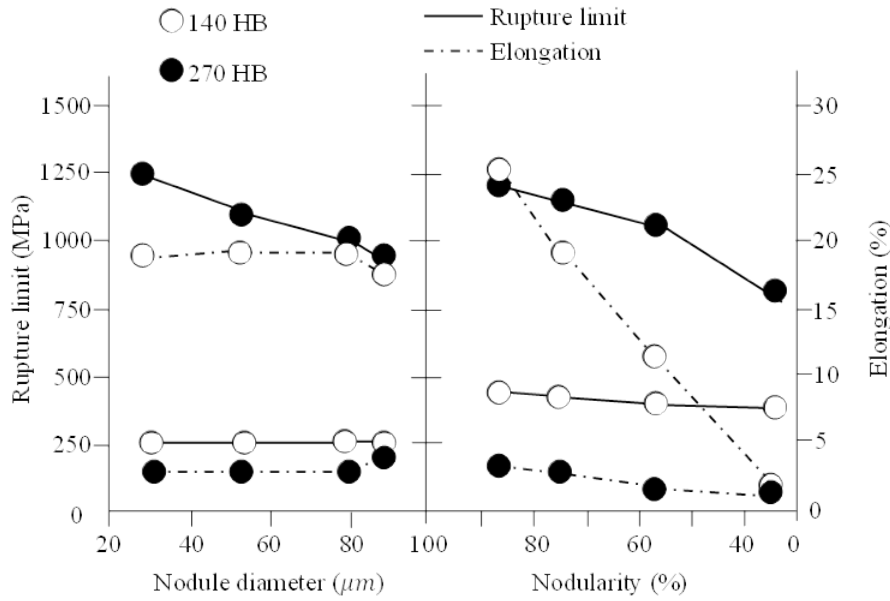
Figure 3.9. Relation between mechanical properties and microstructure parameters in nodular cast iron (Guesser, 2019).

A good inoculation increase the graphite nodule number, which enhances spherical nodules formation distributes the alloy elements' segregation and impurity. The ferrite formation is also affected by inoculation. A good inoculation boosts the ferrite formation, to the detriment of the pearlite, explained due to the decrease of diffusion distance. The number of nodules is still influenced in the solidification by the cooling rate. However, the thickness effect on the mechanical properties is much less in the nodular than in the gray cast iron. The effect of the number of nodules in increasing the resistance is noticeable in the nodular cast irons of high resistance (Sofue *et al.*, 1978) due to the preponderant effect of the distribution of segregations.

When the graphite shape is predominant circular, which means greater than 85%, the most significant variable is the relation between pearlite and ferrite. Various nodular cast iron classes are obtained mainly by the variation of the pearlite/ferrite ratio as table 3.2 indicates. The most preferred ductile irons are respectively GGG 40, 50, 60, and 70, according to microstructure in the industry (Çetinarslan & Karaman Genç, 2014).

Table 3.2. Classifications of ductile iron according to micro structure (Çetinarslan & Karaman Genç, 2014).

Material Type	GGG 40	GGG 50	GGG 60	GGG 70	GGG 80
Micro Structure	Predominant ferritic	Ferritic/ Perlitic	Perlitic/ Ferritic	Predominant perlitic	Perlitic

Pearlite refinement is important in classes with high strength as GGG 70 and superiors. In other hand the ferrite hardness is important in classes as GGG 40 and GGG 50. Alloy elements could improve the pearlite formation and reduce the interlamellar spacing (fig 6.40)

or stimulate ferrite formation.

An important aspect to be considered is that the alloy element's effect depends on the initial matrix. For example, in a ferritic matrix obtained by heat annealing treatment, an increase of Si raise the mechanical strength besides the decrease of elongation due to the ferrite hardening effect by solid solution. In a fully perlitic matrix, the raise in Cu and Mn concentration results in the pearlite refinement, which contributes to mechanical strength raises (Vernugopalan and Alagarsamy, 1990 apud (Guesser, 2019).

The cooling rate also affects the matrix. The increase of the cooling speed hinders ferrite formation and results in pearlite with less interlamellar space. An alternative to enhance pearlite without use alloy elements is the use of high cooling rates. This alternative is appropriated in cases where the presence of small residual stresses is not a problem.

The combined effect of hardening mechanism by pearlite percent raise, pearlite hardening by interlamellar distance decreasing, and ferrite hardening by solid solution is demonstrated in Venugopalan e Alagarsamy work. The mechanical properties are correlated to ferrite and pearlite percent and by the microhardness of these microconstituents.

$$MDM = \frac{(DF \times \%F + DP \times \%P)}{100} \tag{3.3}$$

$$LR = 0,7 + 2,53(MDM) \tag{3.4}$$

$$LE = 84,4 + 1,27(MDM) \tag{3.5}$$

$$Along = 37,8 - 0,093(MDM) \tag{3.6}$$

4 METHODOLOGY

This chapter will present the procedures used in the development of this work. This work aims to evaluate and characterise the nodular cast iron grades GGG40, GGG60, and GGG70. Mechanical tests such as a tensile test hardness test and Bauschinger effect test were performed based on the test standard. In order to complement the material characterization, mechanical tests were performed, together with microscopy analysis, allowing the (proper) identification of the nodules and phases of the NCI. With the microstructure analysis, a MAT-LAB routine capable of counting and characterising the nodules was developed.

4.1 MATERIALS

For the development of this research on the mechanical and metallographic analysis of nodular cast iron, 6 different batches of material were required. The batches of nodular cast iron are divided into round bars and blocks. All batches were purchased from the Metalrens foundry located in Extrema, Minas Gerais.

The division was done so that the influence of the initial geometry on the mechanical properties of the specimen manufactured later could be verified. Each material has different behaviour when subject to load conditions. In order to evaluate the differences between the different types of nodular cast iron, three types of material were required, GGG40, GGG60, and GGG70. The aim was to analyse the microstructure and its influence on the material strength. Table 4.11 presents the chemical composition of the GGG40 purchased from Metralrens foundry used in the test procedures.

Table 4.1. Chemical composition of GGG40.

Chemical element	C	Mn	Si	S	P	Mg	Cu	Cr
%	3.54	0.20	2.30	0.011	0.060	0.038	0.090	*

Table 4.2 presents the chemical composition of the GGG60 purchased from Metalrens foundry.

Table 4.2. Chemical composition of GGG60.

Chemical element	C	Mn	Si	S	P	Mg	Cu	Cr
%	3.68	0.30	2.39	0.022	0.070	0.045	0.055	0.080

Table 4.3 presents the chemical composition of the GGG70 purchased from Metralrens foundry.

Table 4.3. Chemical composition of GGG70.

Chemical element	C	Mn	Si	S	P	Mg	Cu	Cr
%	3.45	0.31	2.88	0.030	0.075	0.045	0.75	0.010

Each material depends on the analysis of the cast iron bars and blocks. The cast iron blocks have dimensions of $300 \times 150 \times 150$ (dimension in mm). The test specimens were arranged in the block in such a way that there were 5 test rounds for each material. The rounds were divided into 4 tests: traction test, compression test, Bauschinger effect test, and cyclic test. The side face was chosen for the removal of the specimens; in this way it is possible to evaluate the amount of graphite and its influence in each section, similar to the methodology adopted by Vokál *et al.* (2008). The graphite nodules have a lower density than iron, so the nodules of graphite tend to fluctuate during the cooling period.

The top of the block has a higher concentration of graphite due to the graphite nodules density. Through this division by zones it is possible to evaluate the specimens from a lower zone (lower concentration of graphite nodules) to a higher one (higher concentration of graphite nodules). The specimens were properly identified and then subjected to mechanical tests. The division of the material block and the arrangement of the specimens in it are shown in Figure 4.1.
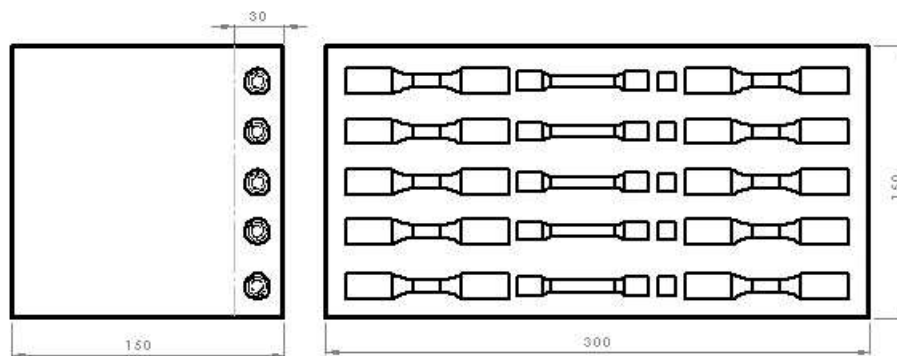
Figure 4.1. Arrangement of the specimens in the solid material block (dimensions in mm).

Figure 4.2 shows the arrangement of the specimens in the massive material block. The top section has a tendency to have more graphite nodules due to the density.
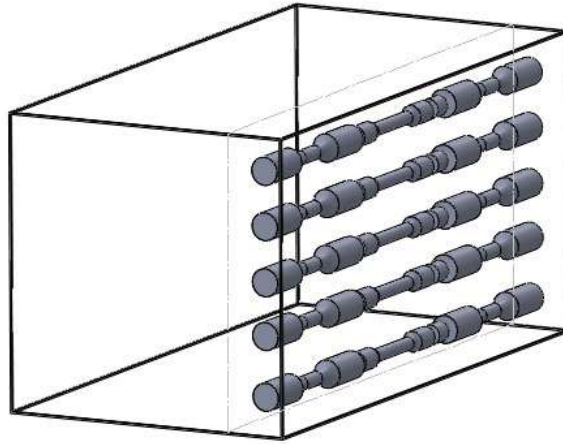
Figure 4.2. Isometric view of the arrangement of the specimens in the solid material block.

Figure 4.3. Manufactured specimens. From left to right: Bauschinger effect, tensile test and compression test.

Following the same methodology for all the manufactured specimens, the tensile, and Bauschinger effect tests were performed. Samples were manufactured from cast iron of different geometries to evaluate the mechanical behaviour and microstructure. The reason is that the cooling rate and the geometry shape could affect the microstructure, as well as the graphite shape and distribution, thus affecting the mechanical properties (Çetinarslan & Karaman Genç, 2014).

4.2 MECHANICAL TESTS

For the tests, the equipment used belonged to the materials laboratory and the Group of Experimental and Computational Mechanics (GMEC) of the Faculty of Gama at University of Brasilia (UnB). For the development of the mechanical tests, the Instron 8801 universal traction

servo-hydraulic machine was used. The machine has a load cell with a 100 kN load capacity and devices that allow tensile, compression, and fatigue testing. The tests were carried out using an Instron uniaxial extensometer with a 12 mm deformation range so that the results are more reliable concerning the capture of displacements in the region of interest. All the tests were performed using the control software developed by Instron. The setup contains two types of software that make it possible to perform the tests, and control of all the parameters is set in the software in order to perform the test according to the specific methodology. Bluehill software was used for quasi-static tests and WaveMatrix software for the cyclic fatigue tests. It is worth noting that all the tests were guided by international standards and complied with the specified requirements. Figure 4.4 shows the Instron 8801 performing a tensile test.

Figure 4.4. Universal Fatigue Testing Machine Instron 8801.

4.2.1 Tensile testing

The tensile test is based on the ASTM E8 (2010) and consists of the application of axial forces; this type of test allows the extraction of various information from the material. According to Askeland *et al.* (2010), from this test we can obtain important quantitative and qualitative data on the resistance, stiffness and ductility of the material tested. The most important information in this study was the yield stress and the rupture stress, taken from the stress–strain graph generated from the data collected during the test.

Through a tensile test it was possible to obtain the mechanical properties of the nodular cast iron. In total, 24 specimens were tested, 15 being from the block and 9 from the round bars. The tests were performed in the Instron 8801 universal traction servo-hydraulic machine. Some parameters were set, such as the test velocity, stop criterion, and specimen geometry.

As related by Guillemer-Neel *et al.* (2000), tensile tests for all specimens were performed at a displacement speed of 1 mm/min. The stop criterion chosen was the differential ratio loading, set to 40%, which is a safe value to work; when reached, this means that the specimens have ruptured.

The tensile test specimen was designed according to ASTM E8 (2010). All the specimen information was input in the Bluehill software and the measurement of the diameter of the region of interest was taken using a manual pachymeter. The specimen geometry is displayed in Figure 4.5.
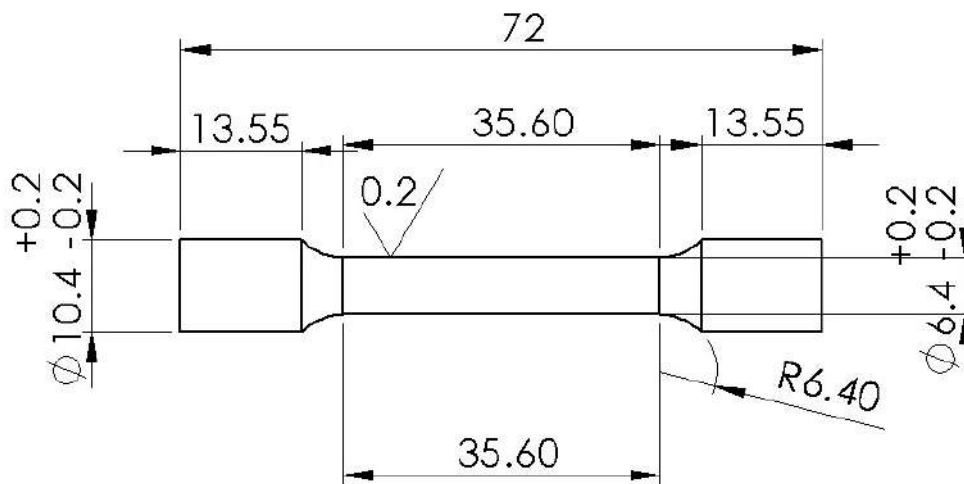
Figure 4.5. Tensile test specimen ASTM E8 (dimensions in mm).

The stress–strain curves related to each specimen were generated in MATLAB using the data generated during the test. It was possible to calculate the Young's modulus, elongation, rupture stress, and yield stress.

4.2.2 Hardness test

The hardness test is a simple and effective method for determining mechanical characteristics of the material, according to Li *et al.* (2002). The Vickers hardness test performed as recommended in ASTM E92 (2017). A ZHU250 ZwickRoell was used for the universal hardness test. The HV number is an expression of hardness obtained by dividing the force applied to a Vickers indenter by the surface area of the permanent impression made by the indenter.

A Vickers indenter is a four-sided pyramid diamond indenter with face angles of 136º. The hardness definition is given by:

$$HV = \frac{F}{S} = \frac{2F sin(136°/2)}{d^2}, \tag{4.1}$$

where F is the applied force (kgf), S is the surface area of indentation (mm^2) and d is the

mean diagonal length of the indentations (mm).

The microhardness test was performed to obtain the ferrite, pearlite, and graphite hardness. The test consists of the use of a calibrated machine to force a Diamond indenter into the surface of the material evaluated. In this test, it was used the DuraScan G5 - EMCO-TEST for microindentation hardness test. The test forces range from 1 to 1000 gf, and the diagonals are measured after load removal. For any microindentation hardness test, it is assumed that the indentation does not undergo elastic recovery after force removal. The test have followed the ASTM E394 (2017) recommendations.

The specimens were the same used for the metallographic procedure. After the image acquisition for metallographic analysis, the specimens were subjected to the hardness test. First, it was performed the microhardness procedure and subsequently the universal hardness test.

4.2.3 Bauschinger effect and cyclic test

The Bauschinger effect tests were carried out with the Instron 8801 and tests were strain controlled. To reveal the cyclic characteristics of each material, 5 specimens were tested for the Bauschinger effect from the block material; and 2 specimens for the Bauschinger effect from the round bar material. Specimens were manufactured according to ASTM E606 (2013), and for both tests the specimen had the same geometry. Undesirable buckling could appear during testing in the compression loading phase. ASTM E606 (2013) mentions the ratio between the radius-of-curvature and the minimum radius-of-specimen. Lower ratio limits will increase the stress concentration and may affect the fatigue life; higher ratios limit the specimen's buckling resistance. The specimen geometry is represented in Figure 4.6.
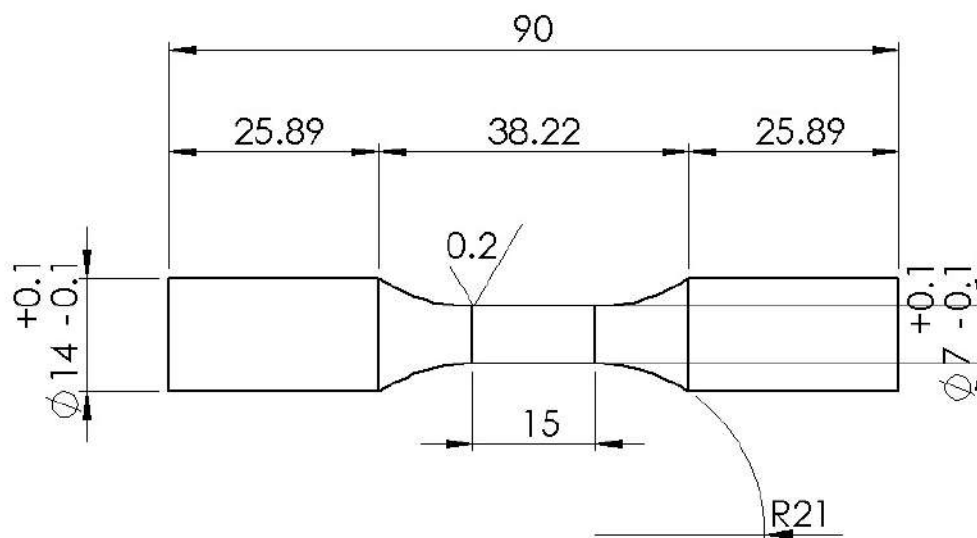
Figure 4.6. Bauschinger effect and cyclic test specimen ASTM E606 (dimensions in mm).

In the Bauschinger effect test, the specimen was subject to traction–compression load as performed by Han *et al.* (2005). The test was done by applying an absolute value in tension and compression at a constant displacement rate of 1 mm/min. The upper and lower load limits in each test were determined from the cast iron flow curves obtained from tensile tests (Toribio *et al.*, 2020).

4.3 METALLOGRAPHIC PROCEDURE

The metallographic process is extremely important in engineering. This process aims to verify the quality of the material in question in terms of its microstructural properties. The metallographic process seeks to relate the material's intimate structure with its mechanical properties and the performance of its function.

In this work, the metallographic analysis procedure in the nodular cast irons GGG40, GGG60 and GGG70 was carried out. The metallography procedure followed the ASTM E3 (2012) recommendations. The metallographic specimens were removed from an NCI block and bar as demonstrated in Figure 4.2. In the blocks, the samples were taken according to the range represented in Figure 4.2, where sample number 1 belongs to the upper face and sample 5 belongs to the lower face of the block. The samples were separated and properly identified. They were removed from the virgin material so that it was possible to evaluate later if the position from which they were taken influenced the mechanical and microstructural behaviour.

In the cutting process a saw machine was used. The horizontal bandsaw Starrett S3720, with a saw blade RL 27mm 3-4 IT27, made a clean and fast cut possible. This model of blade is indicated for the cutting of aluminium, carbon steel, copper, brass, and cast iron among others.

Figure 4.7. Starrett S3720 bandsaw during cutting procedure.

The metallographic analysis of the circular bars was divided into two stages. The first step was to remove the ends of the bar, thus forming two 2-inch diameter samples. These were named with suffix-1 representing a top sample and suffix-2 representing a bottom sample, e.g. 40-1(top) and 40-2(bottom) for the GGG40 samples. The purpose of this methodology is to quantify and characterise the graphite nodules in 9 different positions in the specimen and evaluate the nodule characteristic in relation to the sample position in the round bar, being the top the nearest to the pouring section. The marking of where the optical micrograph should be performed was divided as follows: in the center of the sample, 4 divisions within a radius of 10 mm and 4 divisions within a radius of 20 mm. It was performed 5 measurements in each demarked zone. These samples were not etched, the objective here is to detect the nodule characteristics in the round bar position. Five measurements were performed in each demarked zone. These samples were not etched, as the objective here is to detect the nodule characteristics in the round bar position. Figure 4.8(a) shows how the marking was designed and Figure 4.8(b) shows how the marking was carried out. For convenience, metallographic specimens are not more than about 12–25 mm in diameter because larger specimens are generally more difficult to prepare. This methodology was based on the work of Çetinarslan & Karaman Genç (2014), where the variation of mechanical properties was evaluated depending on the section thickness.
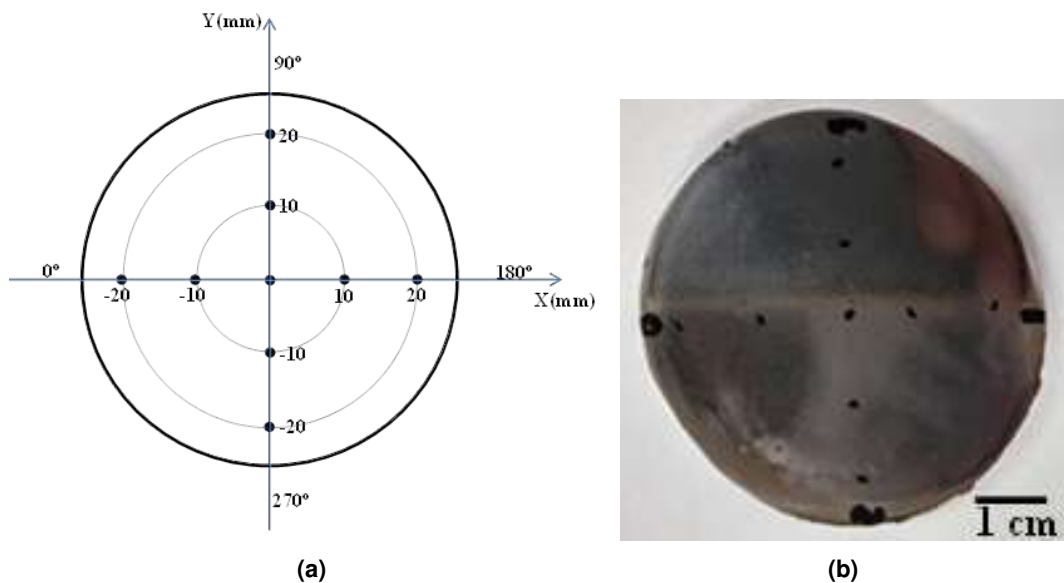
Figure 4.8. Round bar metalographic sample. (a) Marking demonstration. (b) Final sample marked.

In the case of the specimens removed from the block, with 10.4 mm diameter, to provide proper handling of the sample and to protect and preserve the extreme edges or surface defects during grinding and polishing, the sample should be mounted. There are various types of mounting, the most common being hot mounting and cold mounting (Meena & El Mansori, 2012). A self-polymerisable acrylic resin (FORTEL) was used for cold mounting in proportions of 2 parts of powder for 1 part of liquid. The sample was positioned in a silicone mould and the resin was poured. The cure time for this resin time varies from 10 to 15 minutes and the temperature peak could reach 72ºC (manufacturer information).

To ensure proper graphite retention, attention is needed to the loading applied over the specimen, and Radzikowska (2004) advises that the grinding of each step is done in the shortest possible time and with applied forces that decrease as the grit size increases. As soon as the specimen has scratches only in the current sanding direction, it is necessary to change the sandpaper and rotate the specimen by 90º, so as to make it possible to assess whether all the scratches of the previous grit have been removed. It is recommended to use a microscope during the grinding process in order to assess whether the surface is able to be sanded by a finer sandpaper.

The grinding process was performed in a POLIPAN Pantec metal grinding and polishing machine following the grit sequence: P80, P220, P320, P400, P600, P800, P1200 and P2000. The speed of the platen during grinding was always 300 rpm. During grinding, the paper was moistened with flowing tap water, and after each grinding step, the specimens were washed with running tap water and dried with compressed air.

Polishing must also be carried out with care and paying attention to the force applied on the specimen. Proper control of these factors influences the graphite retention. The polishing was performed in three steps, with $3\mu m$ diamond suspension on a napless cloth, with $1\mu m$ diamond suspension on a napped cloth and then with $1/4\mu m$ diamond suspension on a napped cloth. During the polishing procedure, it is recommended to make a counter-rotating motion to avoid pulling out graphite. The polishing cloth was moistened with an alcohol-based lubricant. The speed of the platen during polishing was 300 rpm, as for the grinding, and after each polishing step the specimens were washed with alcohol and dried with hot air from a hair dryer.

Examination of the material microstructure was performed with a Laborana LAB 226IT trinocular inverted metallographic microscope. The microscope was calibrated with a microscope calibration ruler calibrated by the Mitutoyo Metrology Calibration Lab (calibration number - 0031). Microstructural investigations should always begin by examining the as-polished specimen before etching. This is necessary, of course, for cast iron specimens, if one is to properly examine the graphite phase. As in Karaca & Şimşir (2019); Souza *et al.* (2014); Gonzaga (2013); Ceschini *et al.* (2015); Lucas *et al.* (2017), the specimens were etched with a 2% nital solution (alcohol + HNO_3), by immersion for up to 5 seconds.

4.4 COMPUTATIONAL IMAGE ANALYSIS

To perform a computational image analysis a routine in MATLAB was developed using the considerations given by ASTM E2567 (2015) and ASTM A247 (2020), which is the standard for determining the nodularity and nodule count in ductile cast iron using image analysis. The developed routine was used to evaluate the graphite nodule area density, graphite average area, percentage of nodular graphite, sphericity, compactness, eccentricity, graphite, ferrite and pearlite content percentage in etched samples. The developed routines are available on the web, for nodule counting and characterization (Fernandes, 2022b), and phase counting (Fernandes, 2022a).

The first step in this procedure is to load the image in MATLAB. For the nodule count and

characterisation, the image has to be converted from an RGB scale to a greyscale. Each of the pixels that represent an image carries values that describe how bright that pixel is. For a greyscale image, the pixel is a single number ranging from 0 to 255, where 0 is taken to be black and 255 is taken to be white. Subsequently, the image has to be binarised, in which step some adjustments can be made.

Figure 4.9 shows an input software image. The image is then converted from RGB scale to greyscale as represented in Figure 4.10 and finally binarised, and the analysis starts from this point, as shown in Figure 4.11.
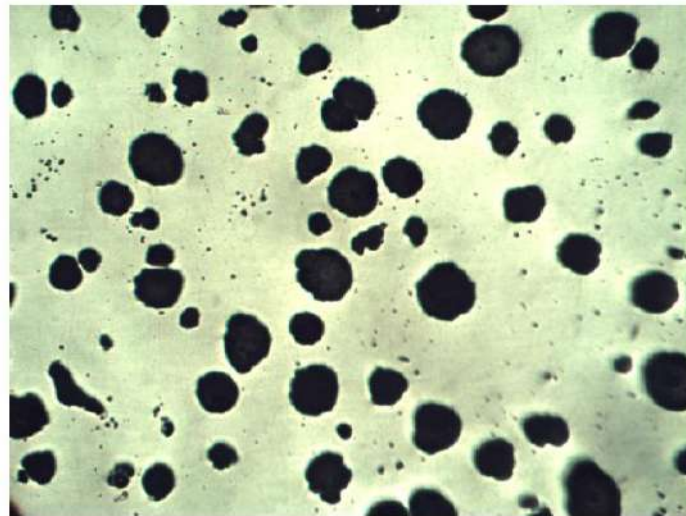
Figure 4.9. Sample microstructure image of ductile cast iron.
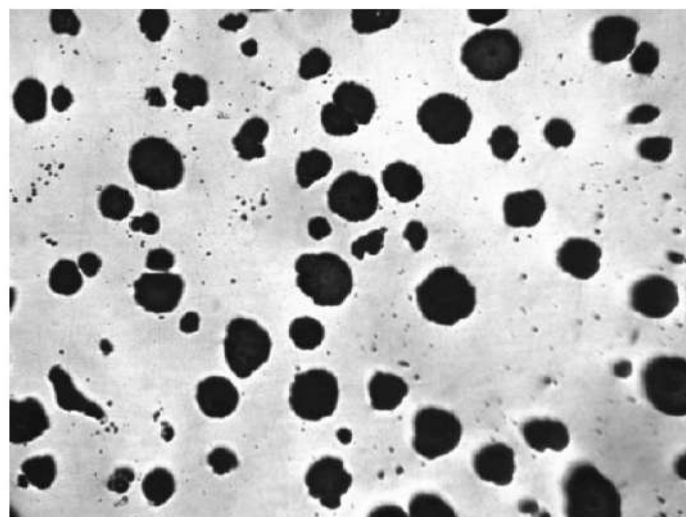
Figure 4.10. Sample microstructure image of ductile cast iron in greyscale.
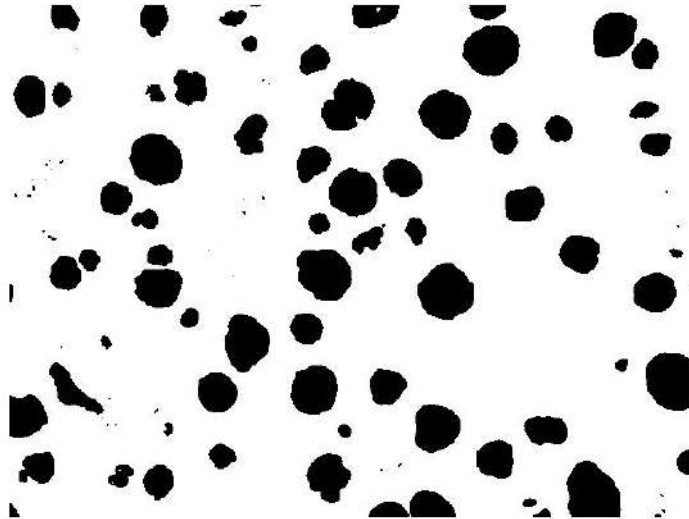
Figure 4.11. Segmentation of microstructure image shown in Figure 4.9

The graphite nodules have the characteristic of being darker than the metal. In this stage, the chemical attack was not carried out in order to identify the graphite nodules easily. If there no adjustments in this step, the software can binarise the areas that do not contain nodules and count as nodules. This is due to the threshold value, for which, as a rule, 50 was used, which means that every pixel that has information above 50 is considered white and every pixel that has information below 50 is considered black. As a result of the light adjustment when the micrograph image was achieved, some images may be darker than others. Adjustment of the threshold value must be done manually, so the software considers as black only the area that is graphite. Figure 4.12 outlines the total procedure for the nodule count.
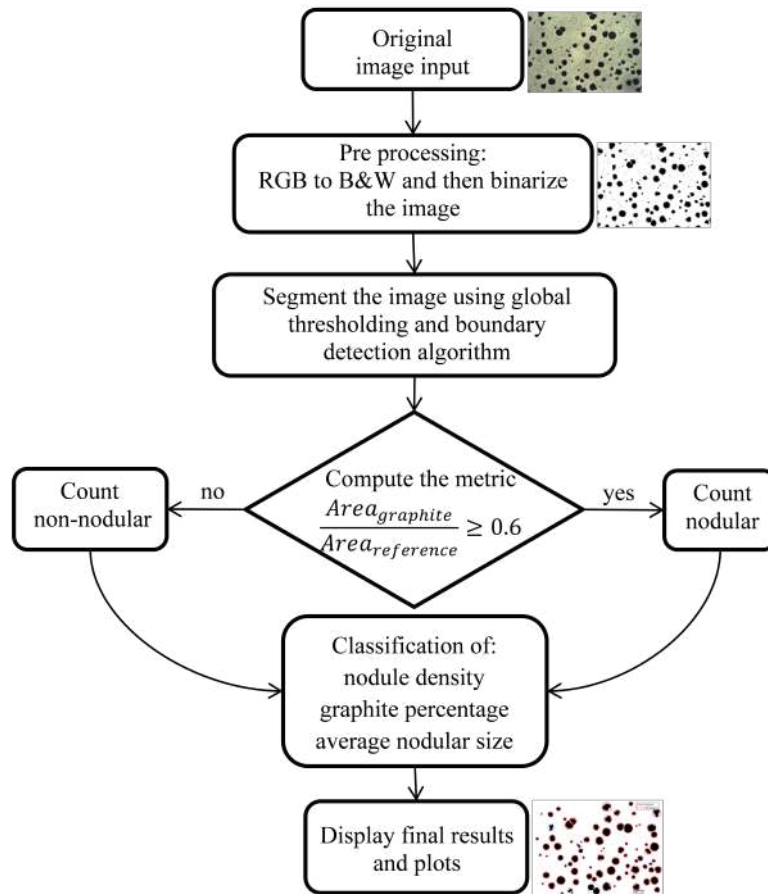
Figure 4.12. Nodule count algorithm flowchart.

After the binarization process, the image contains a white background with the sets of black pixels that form an object, in this case, a graphite particle. The standard recommends that particles smaller than 10μ should be excluded as a way to remove noise. Also, particles that touch the edges of the micrograph image are excluded and only particles that are complete in the image are considered for the evaluation process.

When the image is segmented, each nodule can be well identified and useful morphological properties can be easily identified, the set of black pixels is identified through the boundary detection algorithm.

The methodology used is similar to that of S.Hiremath *et al.* (2014), where a routine in MAT-LAB was also developed for calculating the graphite characterisation and quantification of the ferritic phase. With the binary image, the graphic nodules in black colour are identified as objects. It is possible to check the properties of these objects using the command "regionprops", as performed in Iacoviello *et al.* (2017). Other methodologies are also used for the analysis of nodular cast iron, such as by de Peixoto *et al.* (2015) who used Language C and the OpenCV library, applying two approaches to account for the nodules, one by region growing and the other using a watershed.

33

There are many methods to characterise whether a nodule is circular or not and, according to Grenier *et al.* (2014), a wide variety of analytical parameters can affect the final result of the nodule count. Parameters such as the Shape Factor (SF), magnification, number of fields analysed and trap size are very important factors in image analysis.

The nodule shape must be quantified in order to determine if a graphite particle is above the minimum size to qualify as a nodule. Circularity will be assessed by the use of the SF. For each particle, the area of a reference circle by means of Eq. 4.2.

$$Area\ of\ Reference\ Circle = \frac{\pi(Max.\ Feret)^2}{4} \tag{4.2}$$

The Roundness Shape Factor (RSF) is the ratio between the area of the graphite particle and area of the reference circle. For a perfect circle, the SF is equal to 1. As the particle shape becomes less round, the SF values approach zero. The SF for each graphite particle is calculated through:

$$Roundness_{SF} = \frac{Area\ of\ Graphite\ Particle}{Area\ of\ reference\ Circle} \tag{4.3}$$
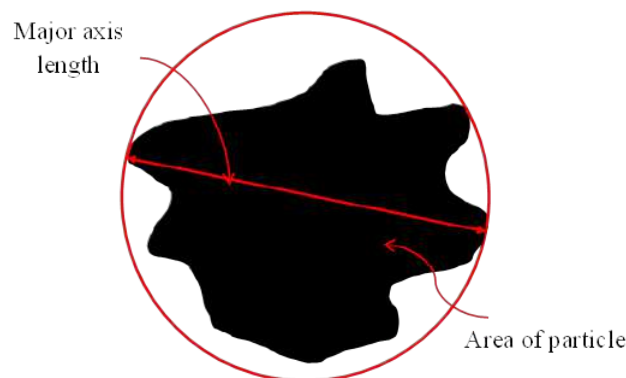
Figure 4.13. Schematic representation of the roundness shape factor (Adapted from Grenier *et al.* (2014)).

There are two other ways to evaluate whether a nodule is round enough to be considered nodular:

$$Compactness_{SF} = \frac{4\pi A_{particle}}{Convex\ perimeter^2} \tag{4.4}$$
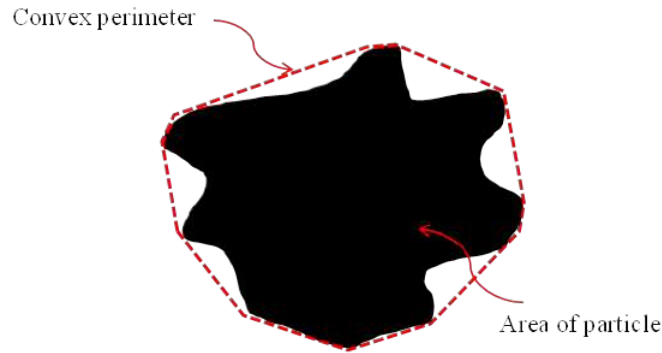
Figure 4.14. Schematic representation of the compactness shape factor (Adapted from Grenier *et al.* (2014)).

$$Sphericity_{SF} = \frac{4\pi A_{particle}}{Perimeter^2} \tag{4.5}$$
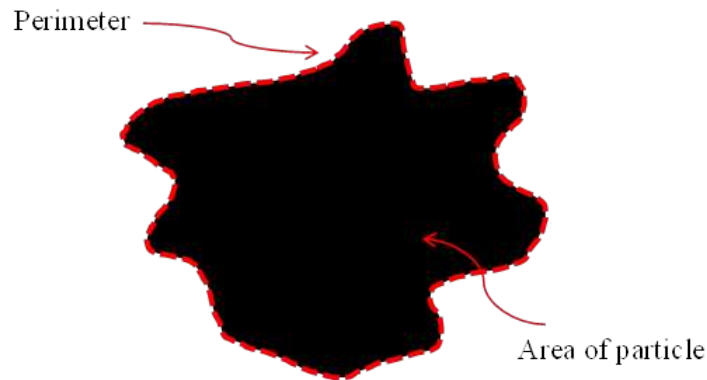
Figure 4.15. Schematic representation of the sphericity shape factor (Adapted from Grenier *et al.* (2014)).

The calculations was developed according to ASTM E2567 (2015). By following the standard parameters this work considering the RSF to defined with the graphite particle is nodular or not. The parameters Compactness Shape Factor (CSF) and Sprericity Shape Factor (SSF) are used as complementary turning the analysis for shape classification more complete.

Another parameter employed to classify the nodules shapes is Eccentricity Shape Factor (ESF). Unlike the roundness, compactness and sphericity, this parameter is much more sensitive and the range is set between 0 and 1 where 0 means perfect spherical shape.

The minimum required SF value to qualify a particle as being nodular is suggested by ASTM E2567 (2015)to be 0.60, and this is the threshold value used in this research. However, other values could be set, as presented in Malage *et al.* (2015), which considered as perfect those nodules with roundness more than 0.8. Prakash (2011), considered the particle circular if the grain SF was equal to or higher than 0.50.

The percent nodularity by area is the definition of the percentage of graphite present in the sample that is nodular. It is defined as the area of graphite features having satisfied the

threshold SF value divided by the area of all graphite features. All graphite particles are taken into account for this, except those that are at the edges of the image and are not complete in the evaluated section. This condition is assessed using Equation 4.6.

$$\%Nodularity\ by\ area = \frac{100(Area\ of\ all\ graphite\ particles \geq 0.6)}{(Area\ of\ all\ graphite\ particles)} \tag{4.6}$$

The nodule density is defined as the nodule count per area unit, that is, the number of particles defined as nodules with the required size and shape divided by the total area of the analysed image. Only whole particles were measured, and corrected for field edge intersection.

$$\%Nodule\ Density = \frac{100(\sum Nodule\ area)}{(Area\ of\ total\ image)} \tag{4.7}$$

5 RESULTS AND DISCUSSION

This chapter is organised following the order of the results obtained during the experimental tests. This section will present the research results and discuss them in detail.

First, the casted round bars are analysed by computational image analysis, where the nodule density and graphite percentage on certain areas of the round bar cross-section are verified.

The second part gives the results regarding the mechanical tests: tensile test, Bauschinger effect, and hardness test. From these results, an analysis of the nodule characteristics and quantity is performed. Also, the microstructure with chemical etching is analysed, complementing the discussion of the results.

Figure 5.1 shows the nodule count per mm^2 at specific points in the cast iron round bar cross-section. Two samples were analysed, one from the top and the other from the bottom, as explained in section 4.1. Figure 5.2 shows the percentage of nodular graphite in relation to all graphite particles. Both figures represent NCI GGG40 results.
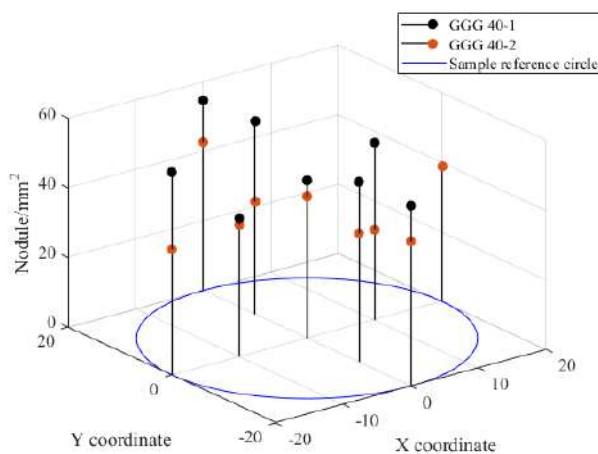
Figure 5.1. Nodule count in GGG40.
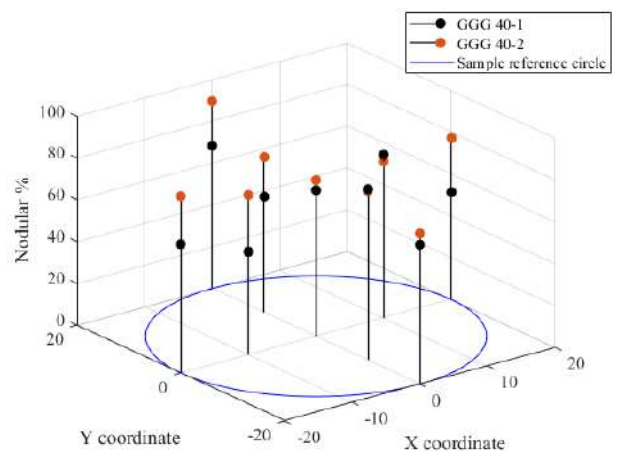
Figure 5.2. Graphite percentage in GGG40.

Figure 5.3 and 5.4 present the results for the nodule count and graphite percentage for NCI GGG60.
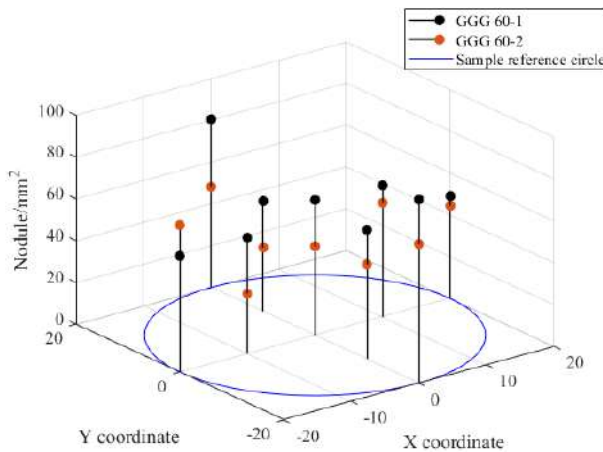
Figure 5.3. Nodule count in GGG60.
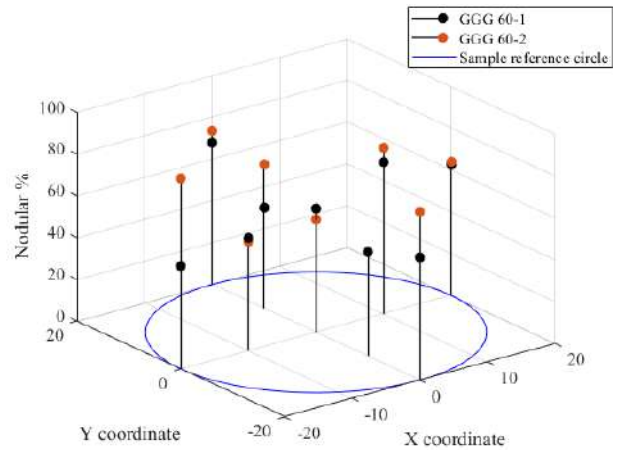
Figure 5.4. Graphite percentage in GGG60.

Figure 5.5 and 5.6 present the results for the nodule count and graphite percentage for NCI GGG70.
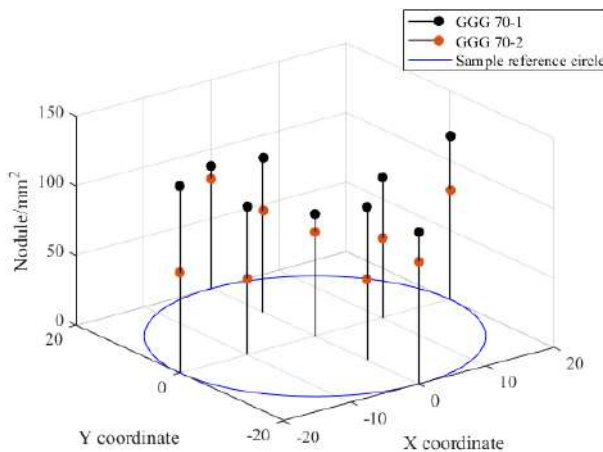
Figure 5.5. Nodule count in GGG70.
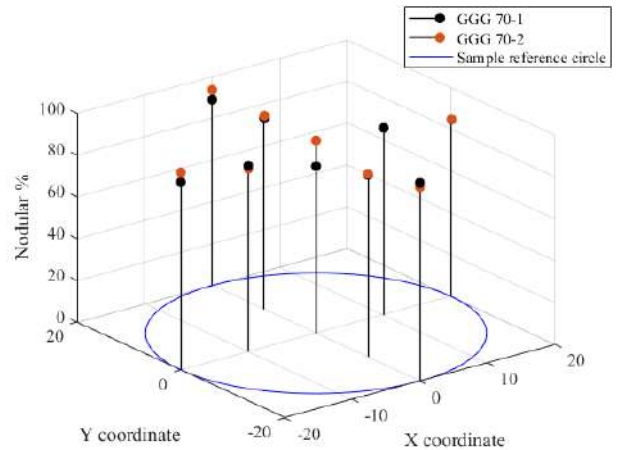
Figure 5.6. Graphite percentage in GGG70.

It is possible to observe a pattern of behaviour in the presented charts. The samples with index indicator -1 correspond to the specimen removed from the top of the round casted bar. This means that the graphite concentration is higher at the top of the casted material. As the graphite nodule is less dense than the material, the nodules tend to float to the surface, causing a higher nodule concentration per area unit in the sample. However, the percentage of graphite particles with a spherical shape was higher in the bottom samples.

The difference was slightly higher in the percentage of nodular graphite, and this phenomenon can be explained by the cooling rate being slightly higher than at the top (leakage of material), so at the bottom the cooling rate is lower, which helps in the nucleation of the graphite.

Another consideration is that the density of nodules recorded in the measurement at the centre of the sample is lower than that measured near the edge of the sample. The explanation is that in the geometry edges the cooling rate is higher than in the middle, so the time for graphite nucleation is not enough. As a logical explanation, the average graphite size tends to

be greater in the sample centre because of the low cooling rates, which enable the graphite nucleation. The greater the graphite nodule size, following a proportional logic, the lower will be the nodule density measured. The curious fact is that this phenomenon does not occur.

The average graphite nodule size was lower in the centre of the sample in comparison with the edges of the samples. It is possible to see that the nodular graphite percentage in the middle was lower than at the edges. The graphite nodules do not meet the circularity factors, which affects the count and the final size of the nodules of the analysis carried out in the centre of the sample. This effect can be explained by the shrinkage allowance, which is the contraction of the final volume after solidification. The analysed samples were taken from the tops of the bar where this phenomenon is more pronounced, affecting the formation of nodules in the centre of the sample.

Figure 5.7 to figure 5.9 show the hardness test results from the bar samples. The measurements were taken from the center, four points in the inner radius, and four points in the outer radius, as demonstrated in figure 4.8. Five measurements were performed at each point in order to obtain the average of the measurements and the final hardness result value at the given point.
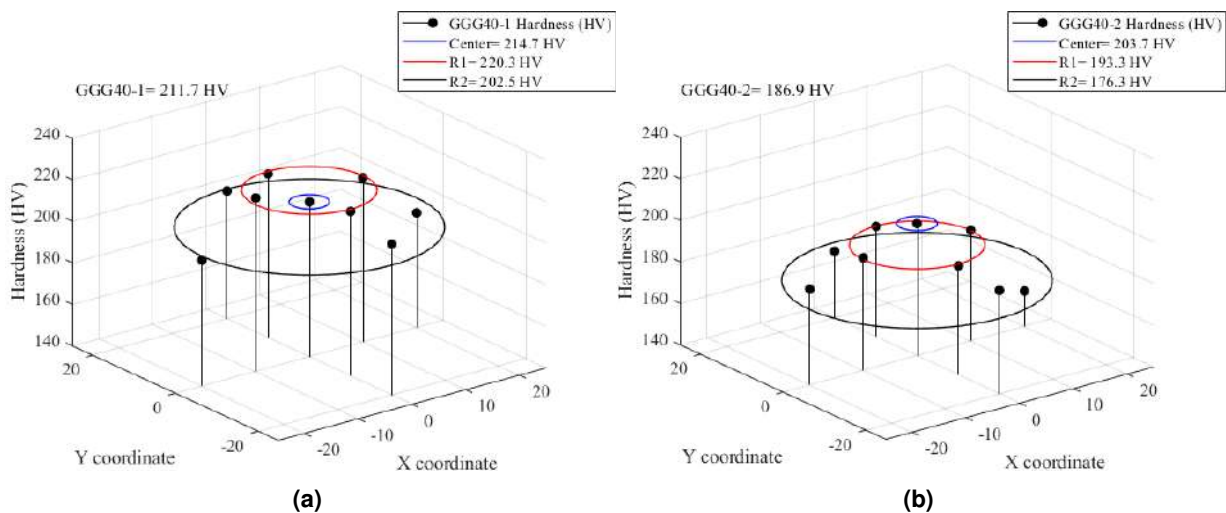
Figure 5.7. Hardness test round bar sample. (a) GGG40-1. (b) GGG40-2.
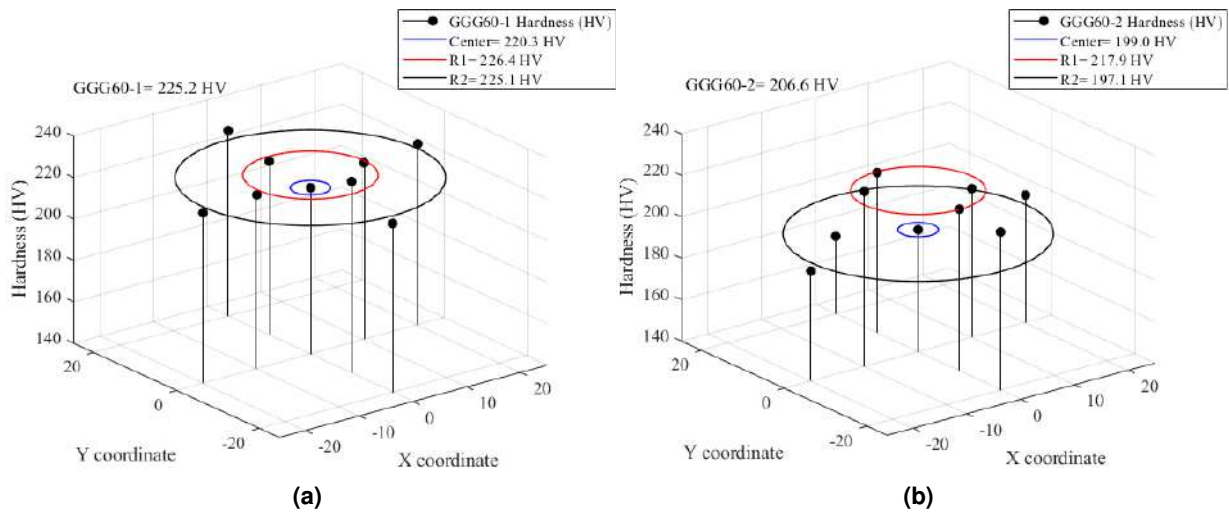
Figure 5.8. Hardness test round bar sample. (a) GGG60-1. (b) GGG60-2.
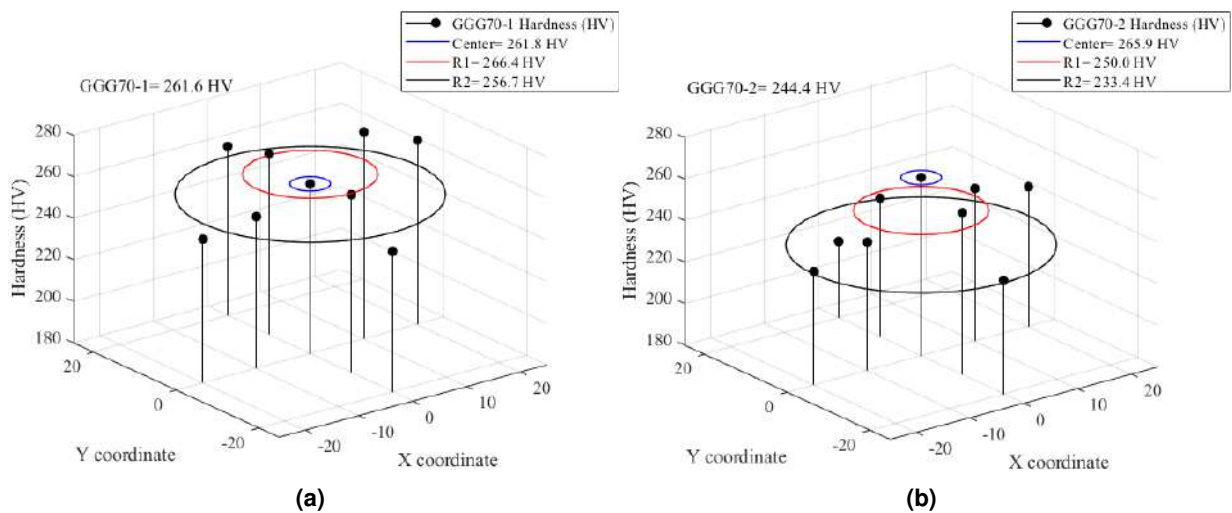
Figure 5.9. Hardness test round bar sample. (a) GGG70-1. (b) GGG70-2.

The results show that the samples with -1 index have higher hardness compared with the -2 index samples. This could be explained by the fact that -2 index samples have higher graphite nodules in the samples. The graphite particles are much softer than the ferrite or pearlite matrix, so bigger nodules could affect the material decreasing the hardness.

In GGG40-1 the average hardness was 211.7 HV and in GGG40-2 186.9 HV, which represents a 24.8 HV difference. In GGG60-1 the average hardness was 225.2 HV and in GGG60-2 206.6 HV, which represents an 18.6 HV difference. In GGG70-1 the average hardness was 261.6 HV and in GGG70-2 244.4 HV, which represents a 17.2 HV difference.

From Figure 5.10 to Figure 5.12 it is possible to see the analysed samples after image segmentation. The routine considered a nodular, graphite particle that fits the parameters established in section 4.3.
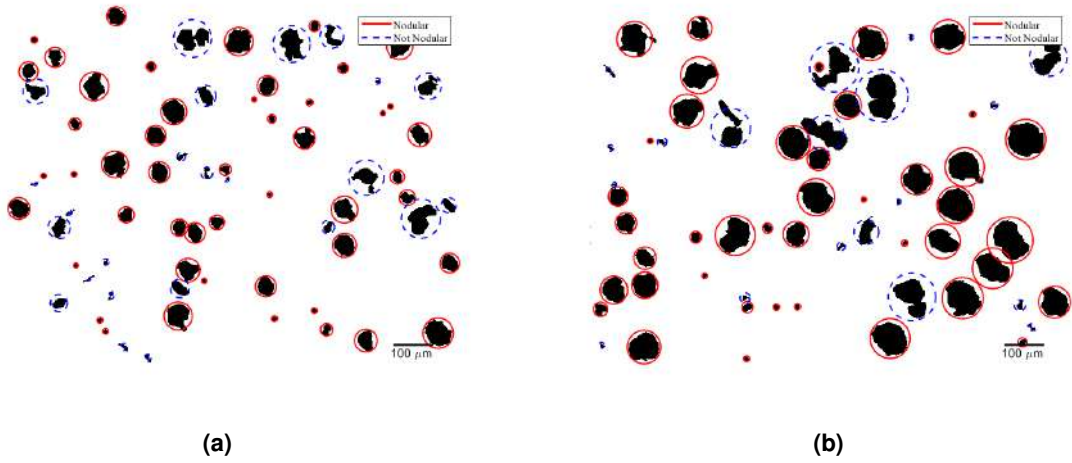
Figure 5.10. Computational image identification on GGG40. (a) GGG40-1. (b) GGG40-2.
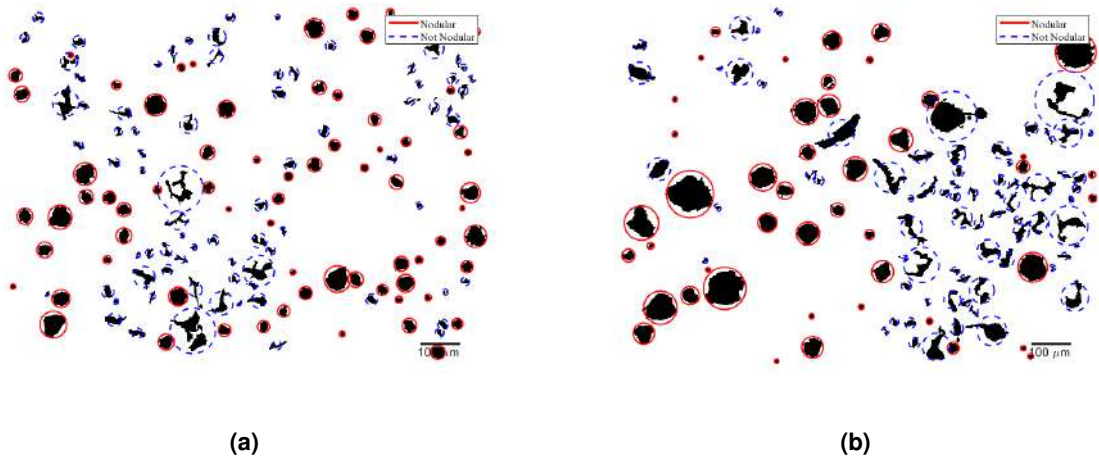
Figure 5.11. Computational image identification on GGG60. (a) GGG60-1. (b) GGG60-2.
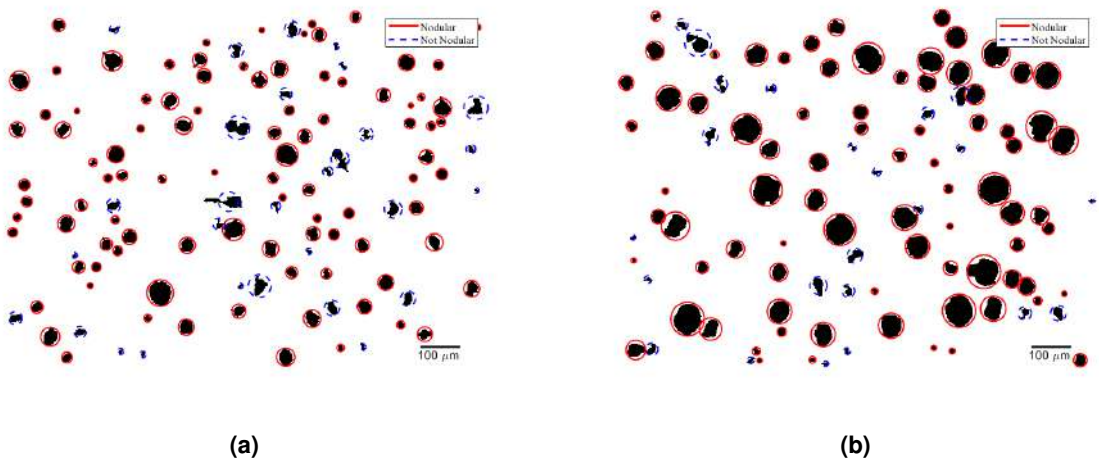
Figure 5.12. Computational image identification on GGG70. (a) GGG70-1. (b) GGG70-2.

From computational image identification figures, it is noticeable the difference between the nodule size in -1 and -2 index samples. For all materials the results were repeated, the index

-2 samples have bigger graphite nodules, which affect the mechanical properties. Another fact that could be analyzed from the image identification is the casting quality of GGG60. In comparison to GGG40 and GGG70, the GGG60 has a large number of vermicular particles, which indicates a possible problem in the casting procedure.

In GGG40 and GGG70 the nodules have a satisfactory, percentage and shape of graphite nodules. The index -2 samples have better roundness with a slight difference in the shape quality. The number can be verified by table 5.1.

Table 5.1 summarises the graphite characteristics analysed from round bar specimens.

Table 5.1. Round bar specimens graphite characteristics.

	GGG40-1	GGG40-2	GGG60-1	GGG60-2	GGG70-1	GGG70-2
Nodule/mm^2	49.63	36.99	63.40	47.88	107.17	70.59
Nod. Graphite (%)	64.71	78.33	58.03	68.21	88.39	90.62
Avg. Area	1.20	2.58	0.75	1.33	0.75	1.39
Sphericity	0.7991	0.8000	0.7534	0.7194	0.9027	0.9057
Compactness	0.8678	0.8762	0.8100	0.7920	0.9341	0.9356
Roundness	0.6543	0.6900	0.5926	0.5832	0.7454	0.7578
Eccentricity	0.6720	0.6396	0.7069	0.7083	0.5927	0.5776

From Table 5.1 it is noticeable that the top samples have higher nodule density, although the percentage of nodular graphite in the bottom samples is higher than in the top samples. In accordance with the nodular graphite percentage, the average area of nodular graphite is higher in the bottom samples too. This behaviour is repeated in other NCI samples. The parameters that indicate nodularity, such as sphericity, compactness, roundness, and eccentricity, are slightly close in their pair samples, but when compared overall the GGG70 specimens present a better cast quality, as can be visually confirmed in Figure 5.12. The GGG60 samples present a high percentile of graphite flakes (Figure 5.11), and the data from routine calculations confirms the poor quality through the sphericity and eccentricity.

Figures 5.13 to 5.17 present the stress–strain plot obtained from GGG40 tensile tests. In each graph, the Young's modulus has been explicit and a 0.2% strain relation was performed to obtain the yield stress. Figure 5.18 shows the comparison between each specimen.
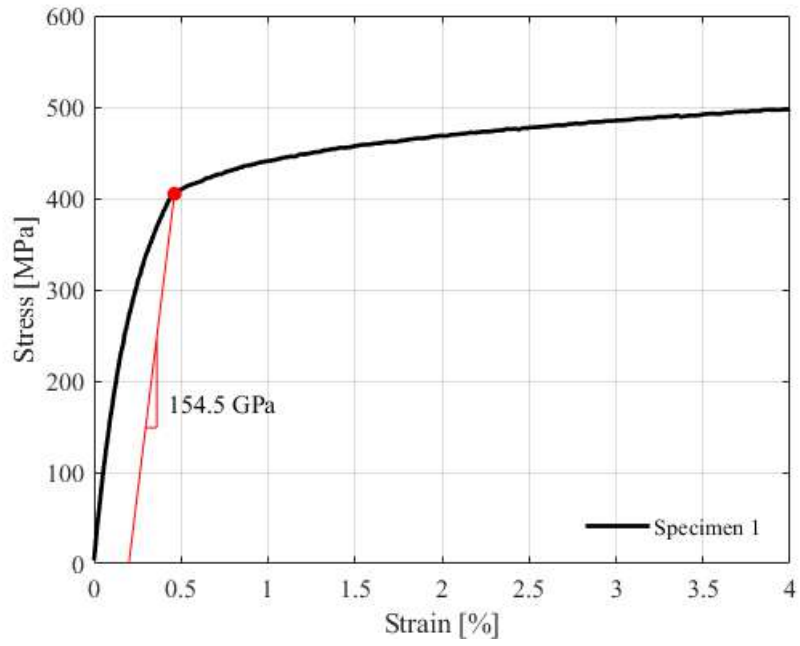
Figure 5.13. Traction test GGG 40 specimen 1.
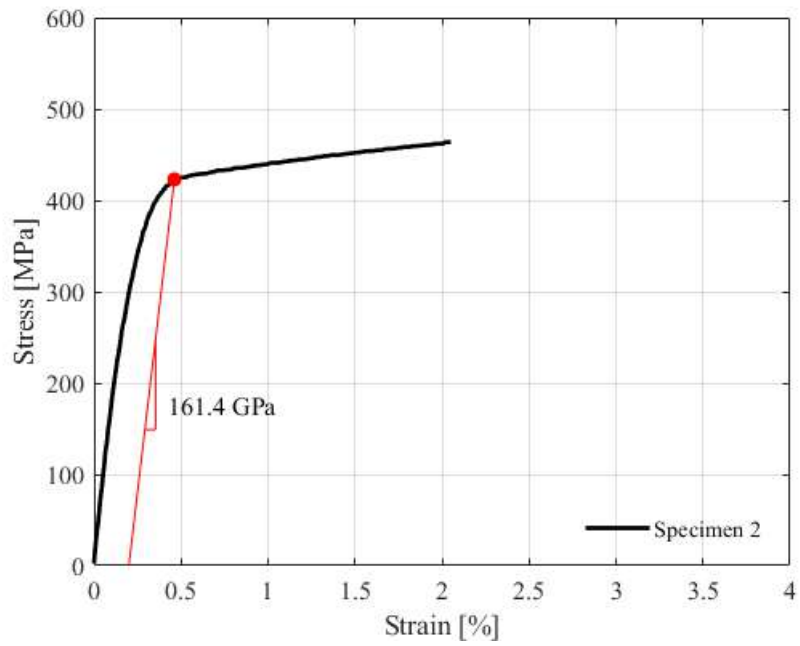
Figure 5.14. Traction test GGG 40 specimen 2.
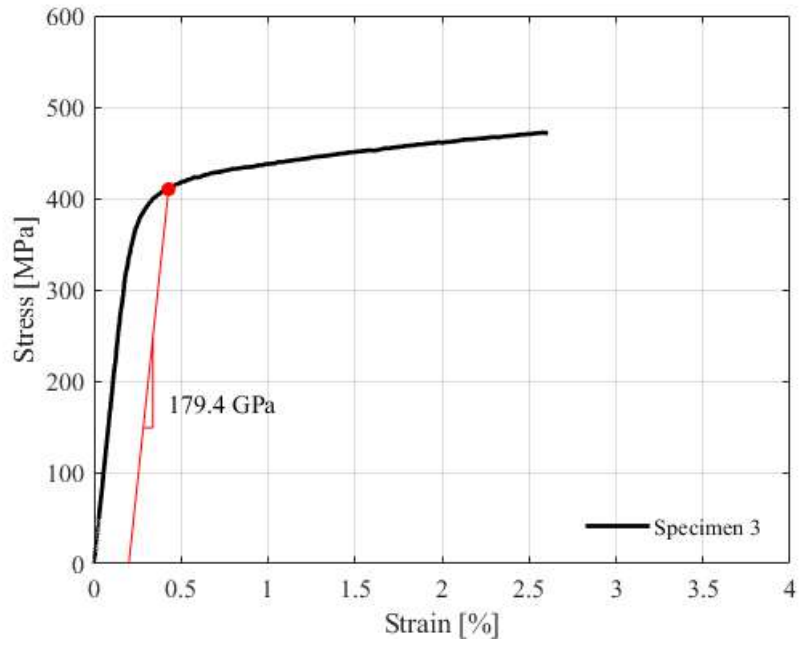
Figure 5.15. Traction test GGG 40 specimen 3.
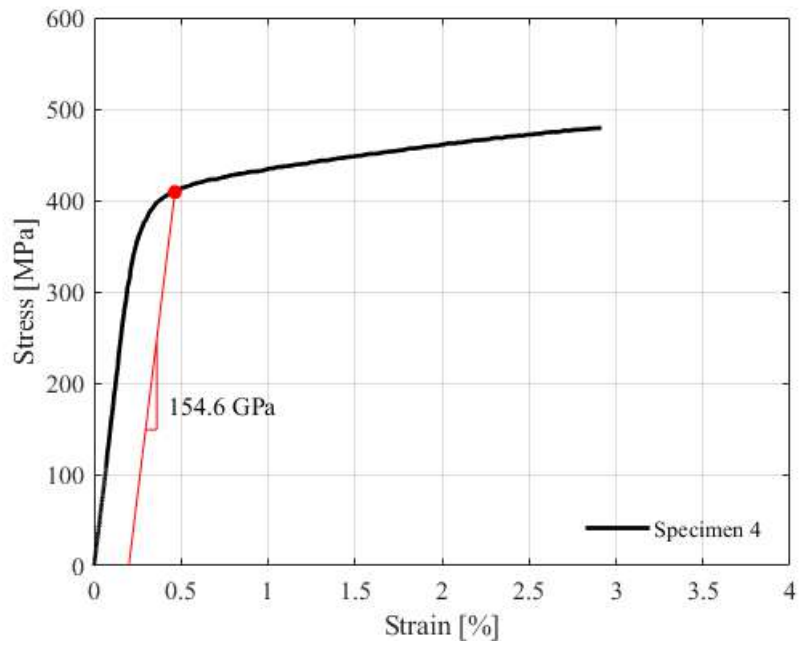
Figure 5.16. Traction test GGG 40 specimen 4.
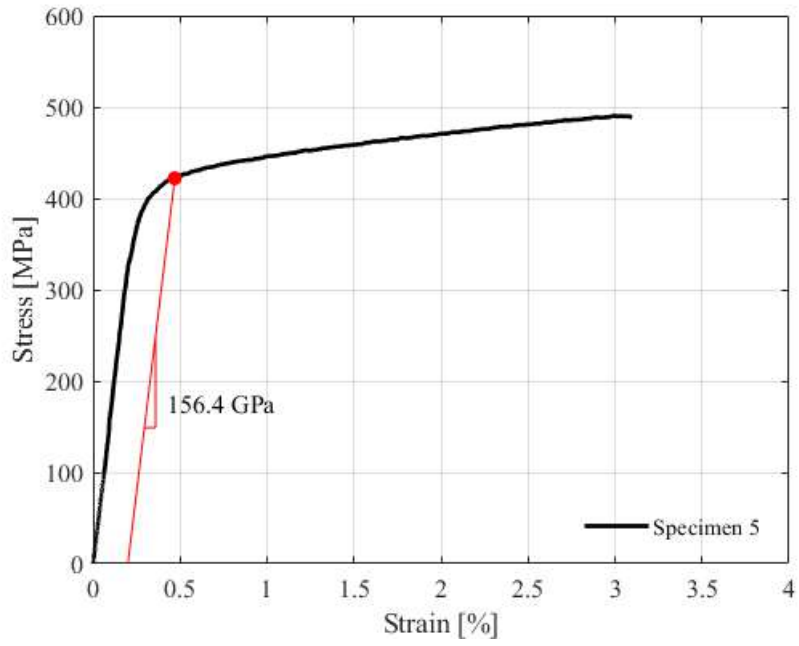
Figure 5.17. Traction test GGG 40 specimen 5.
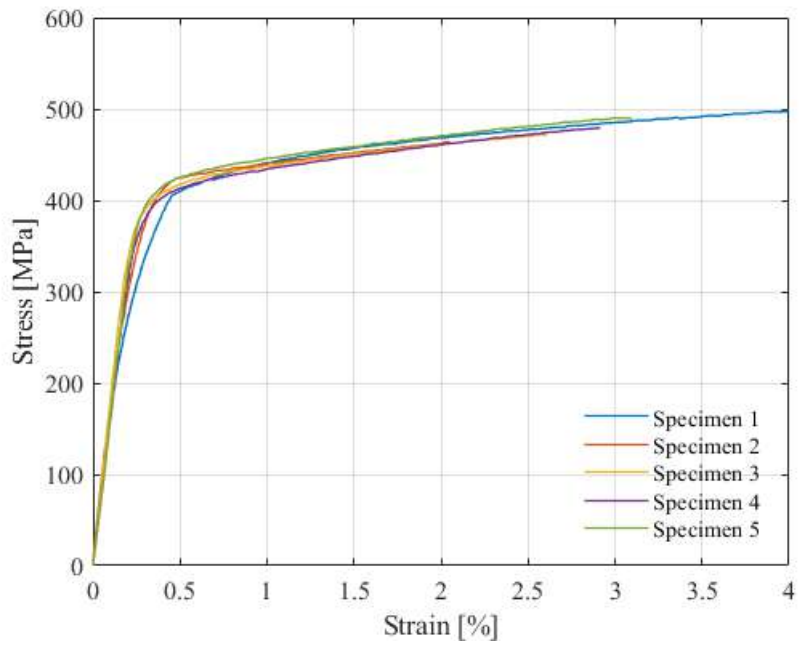
Figure 5.18. Traction test GGG 40; comparison of all specimens comparison.
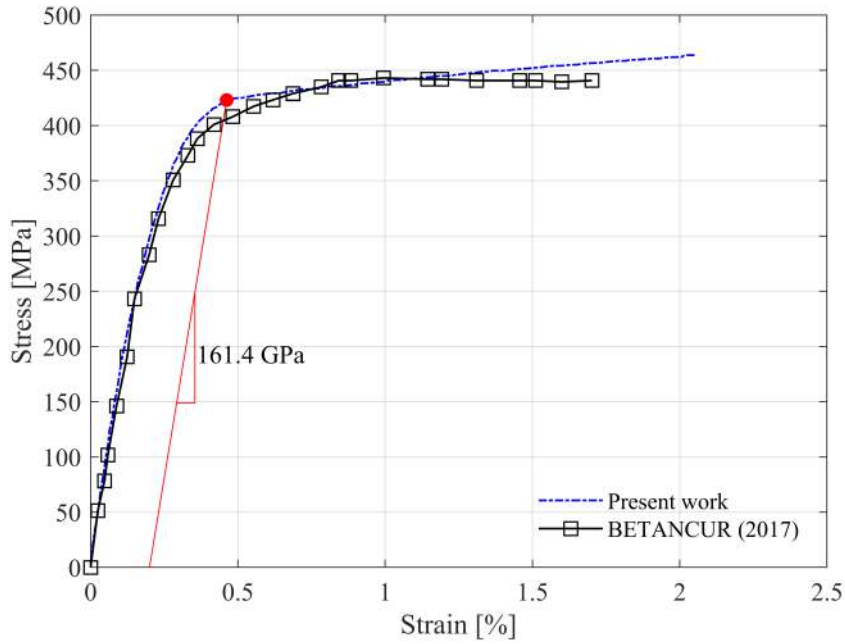
Figure 5.19. Comparison between obtained results.

All the tested specimens have similar behaviour, although the poor elongation in GGG40 was unexpected. Samples 1 (Fig. 5.13) and 5 (Fig. 5.17) have greater elongation and consequently higher ultimate strength. The ultimate strength of all samples was higher than the 400 MPa given by the literature data. The yield stress was significantly higher as well, around 400 MPa.

The elastic modulus fits in with the standard values between 154 GPa and 180 GPa. These different mechanical properties obtained in the data test could have resulted from the specimen extraction without Y-block and the lack of quality control. Table 5.2 summarises the tensile test results.

Table 5.2. GGG40 test results.

	Spec. 1	Spec. 2	Spec. 3	Spec. 4	Spec. 5	SD
σ_{yield} (MPa)	405	423	410	409	422	7.304
σ_{ut} (MPa)	513.4	463.6	471.4	479.4	488.9	17.217
E (GPa)	154.5	161.4	179.4	154.6	156.4	9.410
Max. Elong. (%)	5.843	2.05	2.609	2.916	3.098	1.318
Hardness (HV)	205.2	198.5	203.6	193.0	189.2	6.099

Table 5.3 summarizes GGG40 round bar test results.

Table 5.3. GGG40 round bar test results.

	Spec. 1	Spec. 2	Spec. 3	SD
σ_{yield} (MPa)	-	-	-	-
σ_{ut} (MPa)	368.2	339.3	386	19.244
E (GPa)	136.7	176	164.7	16.520
Max. Elong. (%)	0.3373	0.1829	0.2606	0.063
Poisson	0.2759	0.3838	0.1525	0.094
Hardness (HV)	278.8	277.4	260.8	8.182

The GGG40 specimens manufactured from the circular bar obtained very different results from the same material but manufactured from the block. None of the specimens was able to reach the yield stress with an offset of 0.2%. It was seen in the samples that the specimens from the bar had lower casting quality than the cast block. The specimens had small air inclusions, which caused the premature rupture of the material. An interesting fact is that the hardness proved to be much higher than that of specimens made from the block. The higher hardness is explained by the amount of pearlite in the bar samples.

Table 5.4 presents the GGG40 microindentation results for block and bar specimens.

Table 5.4. GGG40 microindentation test results.

	Hardness (HV)		
	Ferrite	Pearlite	Graphite
Block	212	306	114
Bar	222	383	94

From the results presented in table 5.4, one can note that the samples removed from the bar have pearlite hardness superior to the samples removed from the block, with a 77 HV difference. Due to the geometry section being thinner the cooling rate is lower. The cooling rate increase promotes pearlite hardness. As the cooling rate increase, the carbon diffusion rate decreases, and consequently the interlamellar distance decreases.

Figure 5.20 shows the influence of the graphite nodule density at maximum stress in GGG40. The plot demonstrates that the higher the nodule density, the higher will be the strength. This consideration means that smaller graphite nodules could contribute to the NCI mechanical strength.
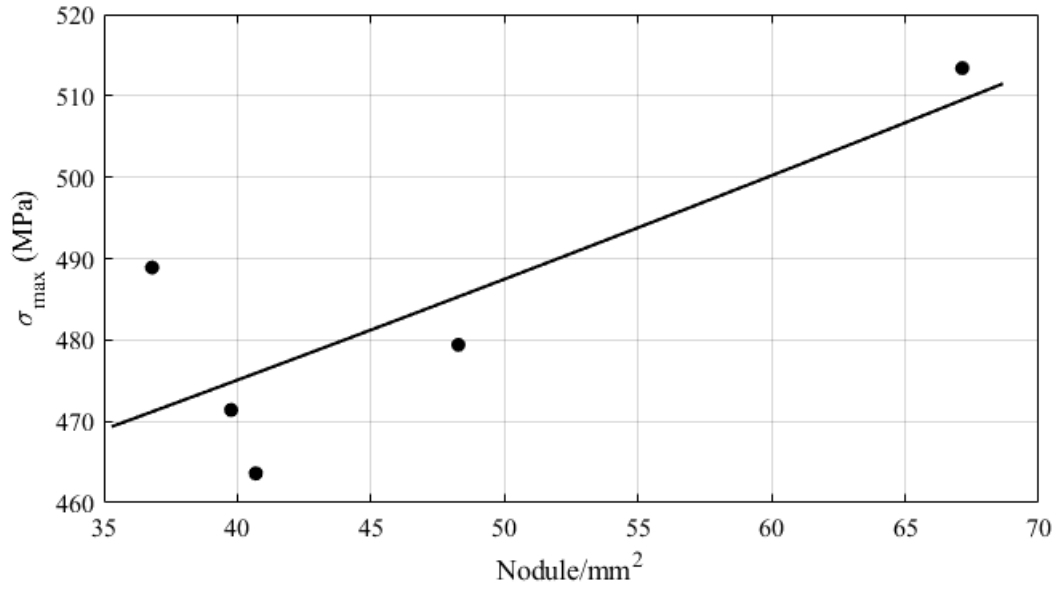
Figure 5.20. Relation between nodule density and maximum stress in NCI GGG 40.

Figure 5.21 to figure 5.26 show the Bauschinger effect tests results. The specimens were tested according to the standard and provided data for comparison with monotonic and cyclic tests (figure 5.27).
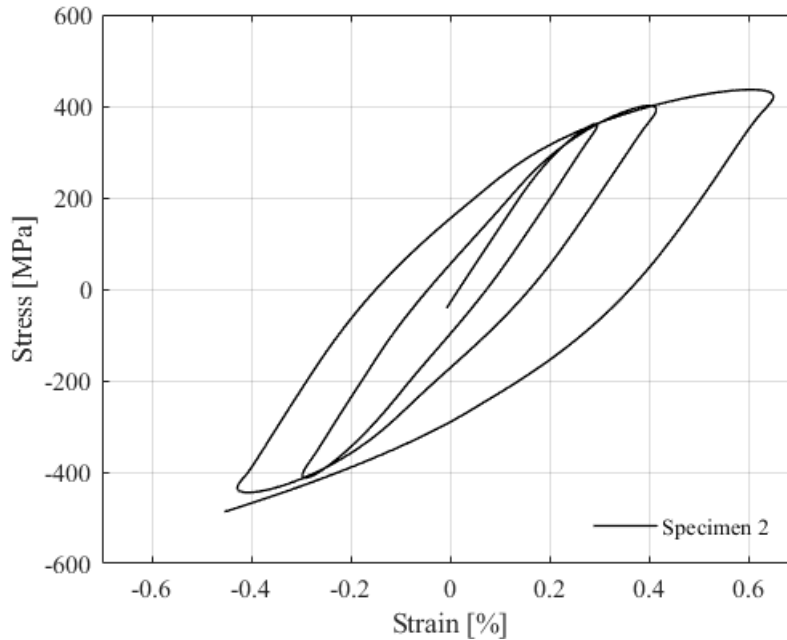
Figure 5.21. Bauschinger test GGG 40 specimen 2.
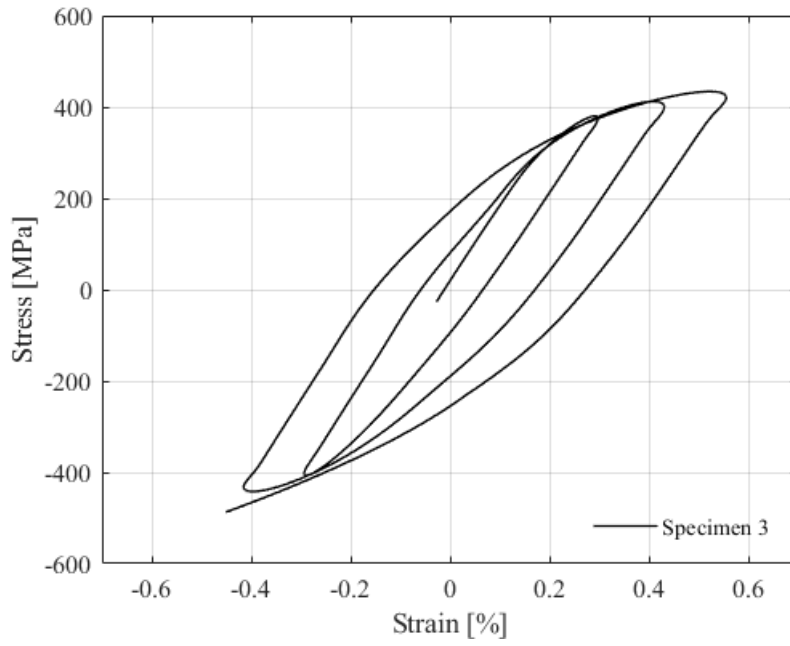
Figure 5.22. Bauschinger test GGG 40 specimen 3.
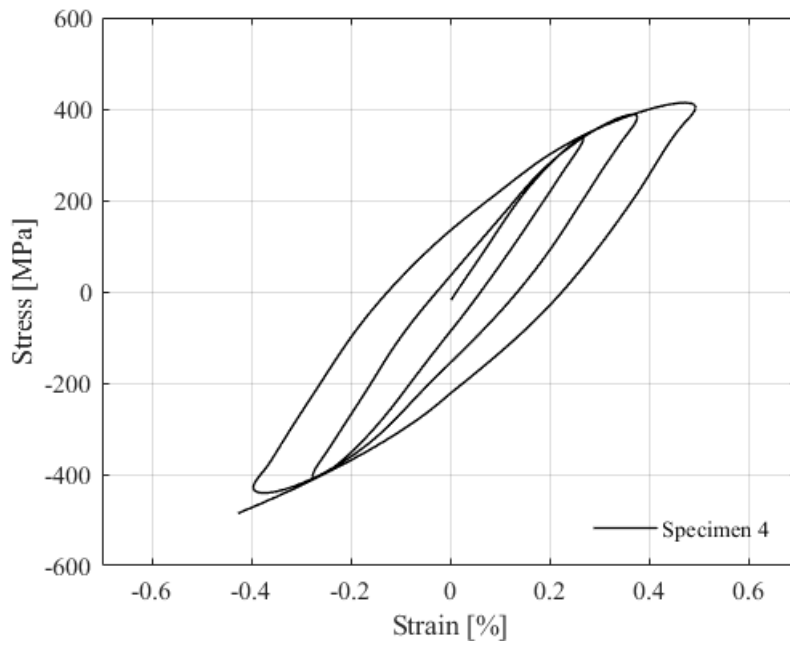
Figure 5.23. Bauschinger test GGG 40 specimen 4.
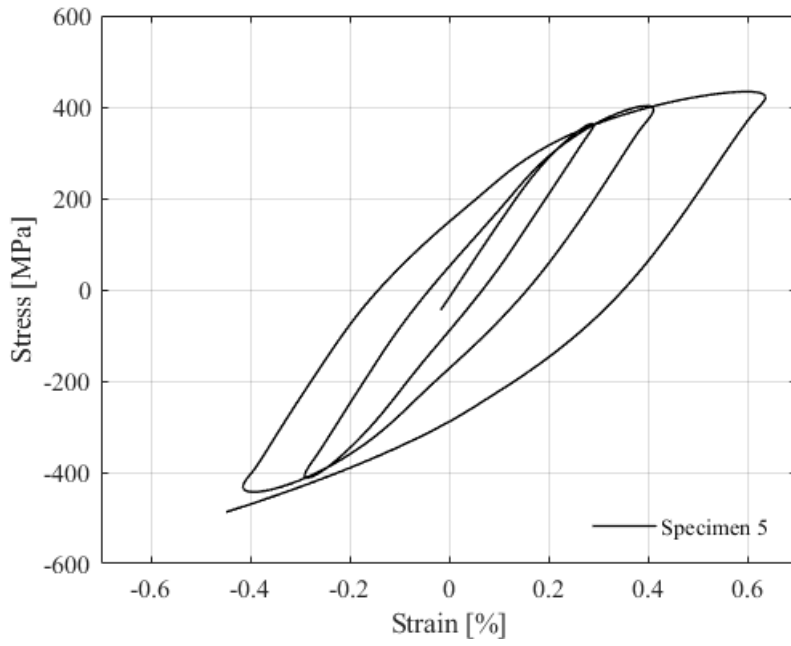
Figure 5.24. Bauschinger test GGG 40 specimen 5.

Figure 5.25. Bauschinger test GGG 40 round bar specimen 1.

Figure 5.26. Bauschinger test GGG 40 round bar specimen 2.
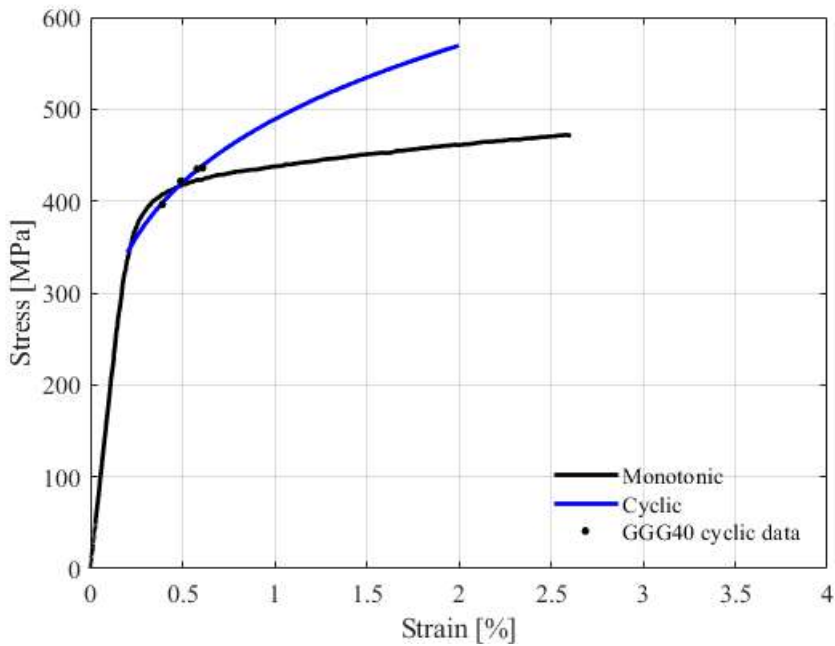
Figure 5.27. Cyclic and monotonic stress–strain curves for GGG40.

The Bauschinger effect analysis shows the GGG40 behavior when subject to tractive and compressive forces. The behavior in the 4 tested block specimens is similar, diverging from the round bar specimens. Due to the round bar specimens having a large amount of pearlite, the samples seem to be more resistant. Round bar samples reach forces 600MPa while block specimens 400MPa. Another behavior that is worth to mention that compressive stress was expected to be higher them tensile stress. Nodular cast iron in general has great capacity

under compressive forces. By the standard, the compressive limit is almost twice the limit for traction.

From the Bauschinger effect was extracted the data of the return points. One was performed an adjustment curve using the Ramberg-Osgood equation. The values returned for GGG40 were $K = 489$ and $n = 0.219$ with $R^2 = 0.9617$. Figure 5.27 shows that the GGG40 under cyclic conditions tends to have a hardening behavior.

Figures 5.28 to 5.32 show the GGG60 stress–strain curve and Figure 5.33 presents a comparison between all the GGG60 tested specimens. The elastic modulus is displayed in each plot. The Young's modulus is approximately the same as reported in the literature. The yield limits were analysed from a 0.2% elastic modulus offset. The greater elongation behaviour in specimens 1 and 5 was repeated as in the GGG40 test, although the elongation limit was still less than that available on the standard.
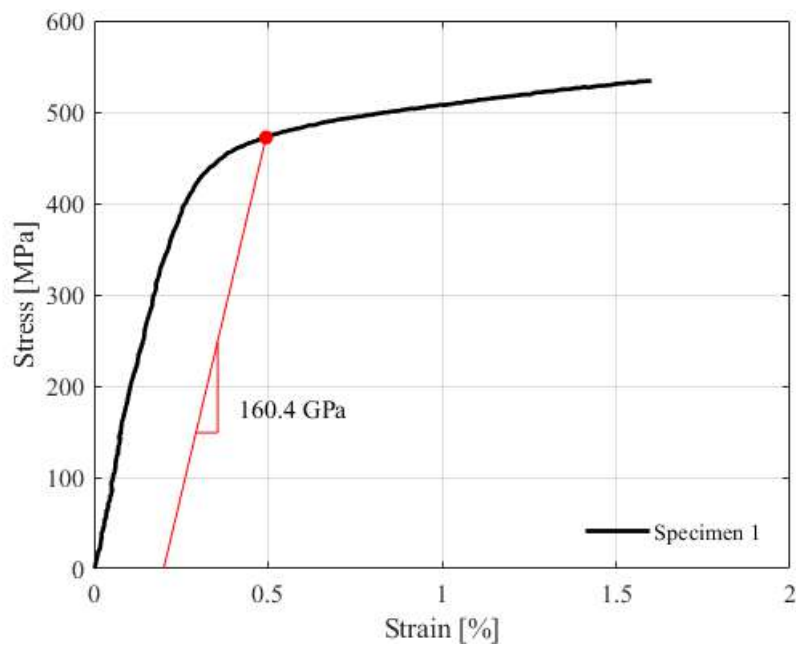
Figure 5.28. Traction test GGG60 specimen 1.
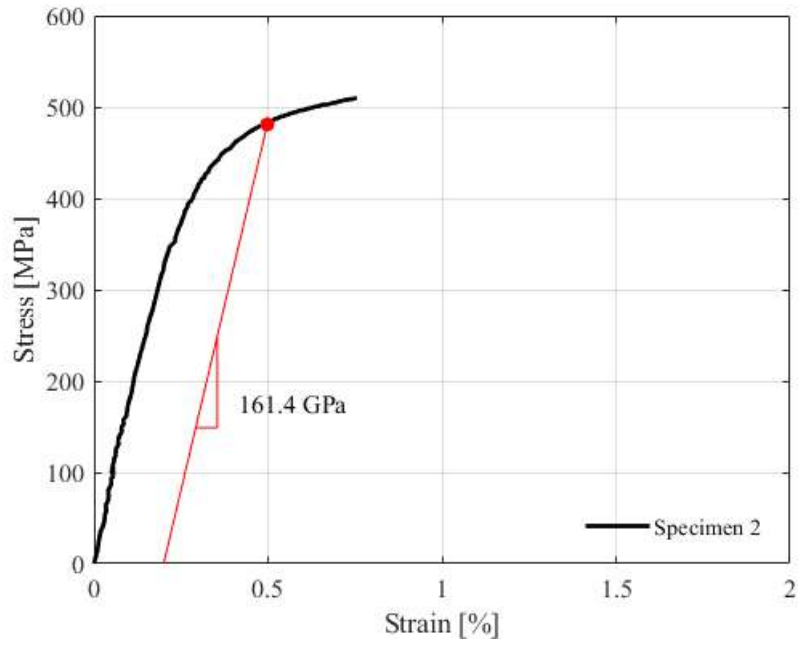
Figure 5.29. Traction test GGG60 specimen 2.
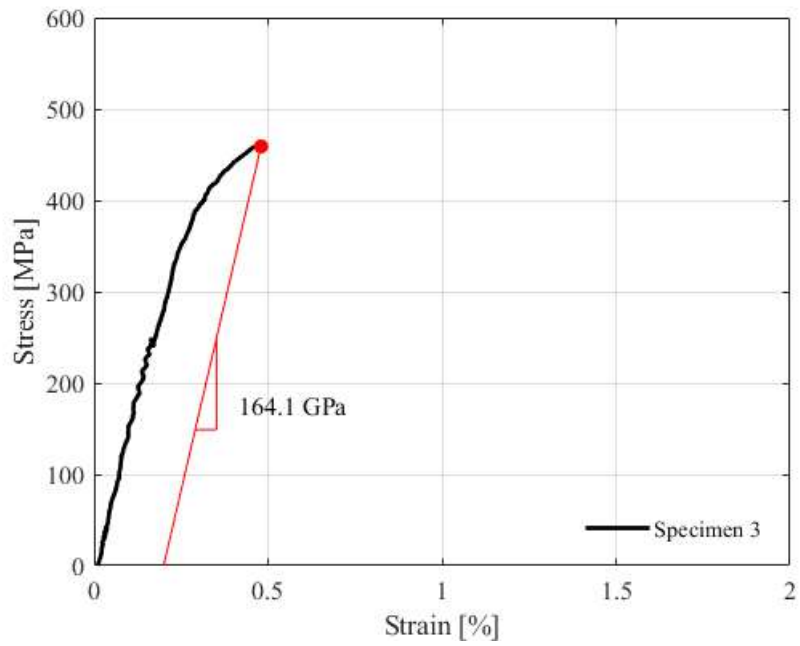
Figure 5.30. Traction test GGG60 specimen 3.
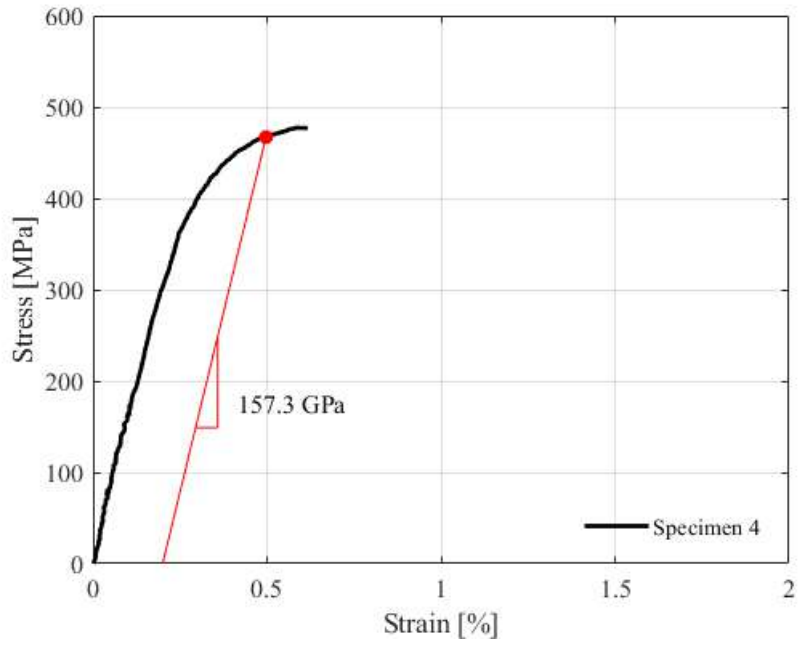
Figure 5.31. Traction test GGG60 specimen 4.
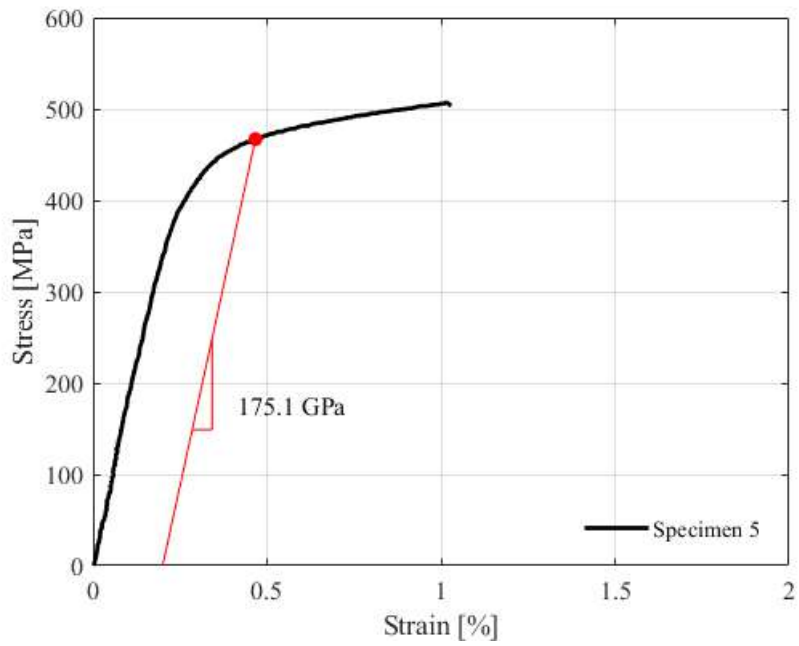
Figure 5.32. Traction test GGG60 specimen 5.

Figure 5.33. Traction test GGG60; comparison of all specimens.

Table 5.5 summarises the results obtained in the GGG60 tensile tests. As for the GGG40, the specimens located at the block edge have greater elongation. This phenomenon could be a result of the nodule density calculated in the sample. Specimens 1 and 5 have higher nodule density and nodular graphite with a smaller area. Additionally, samples 1 and 5 have high ferrite content levels.

Table 5.5. GGG60 test results.

	Spec. 1	Spec. 2	Spec. 3	Spec. 4	Spec. 5	SD
σ_{yield} (MPa)	472	481	459	467	467	7.980
σ_{ut} (MPa)	534.2	509.6	459	476.9	503.7	26.210
E (GPa)	160.4	161.4	164.1	157.3	175.1	6.119
Max. Elong. (%)	1.602	0.755	0.4799	0.6167	1.03	0.396
Hardness (HV)	227.4	254.1	227.0	255.6	239.3	12.393

Table 5.6 summarizes GGG60 round bar test results.

Table 5.6. GGG60 round bar test results.

	Spec. 1	Spec. 2	Spec. 3	SD
σ_{yield} (MPa)	-	427	530	51.500
σ_{ut} (MPa)	383.3	570.6	533.6	80.994
E (GPa)	142.1	148.4	148.9	3.094
Max. Elong. (%)	0.4112	4.528	0.5693	1.905
Hardness (HV)	218.5	225.7	274.0	24.666

GGG60 round bar samples have good elongation compared with GGG40 round bar. De-

spite the poor casting quality, sample 2 has great numbers reaching 4.5% of elongation. The other specimens have small air inclusion which affects the mechanical strength. The hardness values are quite similar in block and bar samples, which was unexpected in the first moment, but subsequently was discovered that round bars have a large amount of ferrite. Table 5.7 present the microindentation test results for GGG60.

Table 5.7. GGG60 microindentation test results.

	Hardness (HV)		
	Ferrite	Pearlite	Graphite
Block	230	339	69
Bar	226	386	87

The microindentation test reveals the high hardness of pearlite content in round bar samples due to the high cooling rate, similar to what occurs in GGG40. The general hardness of the GGG60 round bar however was not superior to block samples. These values could be explained by the material microstructure. Round bar samples have a large amount of ferrite, and graphite particles have a large amount with vermicular and non-nodular shapes, which was not expected in this type of material.

Figure 5.34 shows the influence of the graphite nodule density at maximum stress in GGG60. The plot demonstrates that the higher the nodule density, the greater will be the strength, in accordance with the related GGG40 trend plot. In GGG60 this effect was seen to be more aggressive, which could be related to the average nodule size in the sample.

Figure 5.34. Relation between nodule density and maximum stress in NCI GGG60 for 5 specimens tested.

Figure 5.35 to figure 5.41 show the Bauschinger effect tests results for GGG60. The specimens were tested in the same conditions GGG40. Figure 5.42 compares the monotonic

and cyclic behaviour in GGG60.
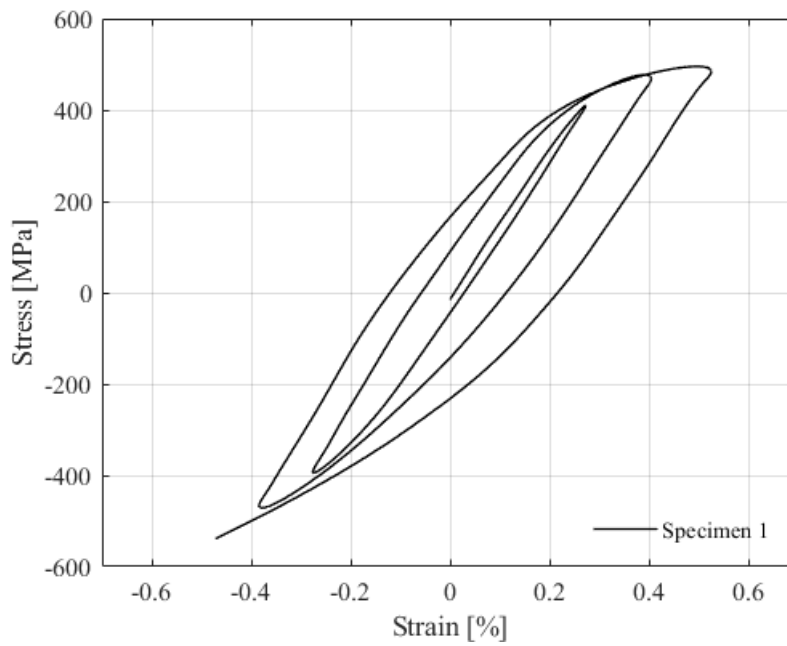
Figure 5.35. Bauschinger test GGG 60 specimen 1.
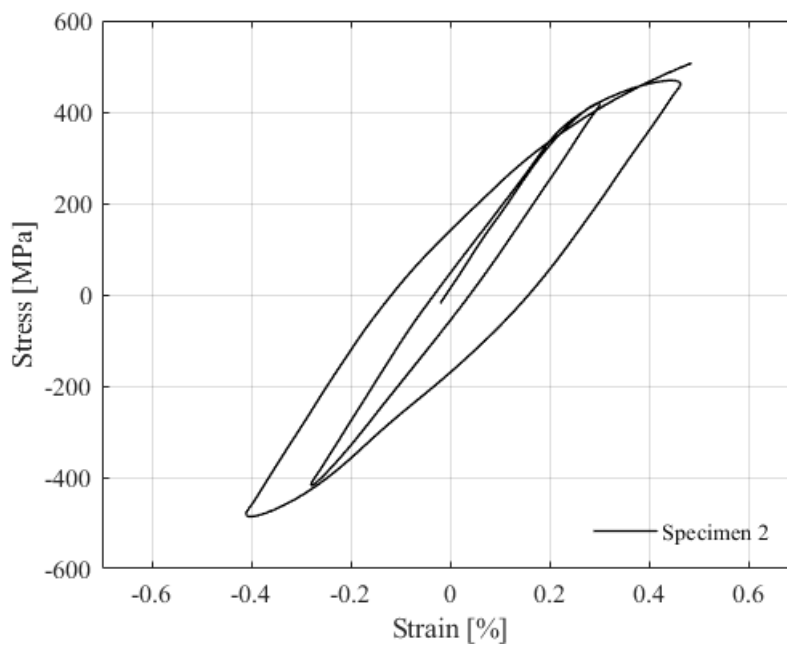
Figure 5.36. Bauschinger test GGG 60 specimen 2.
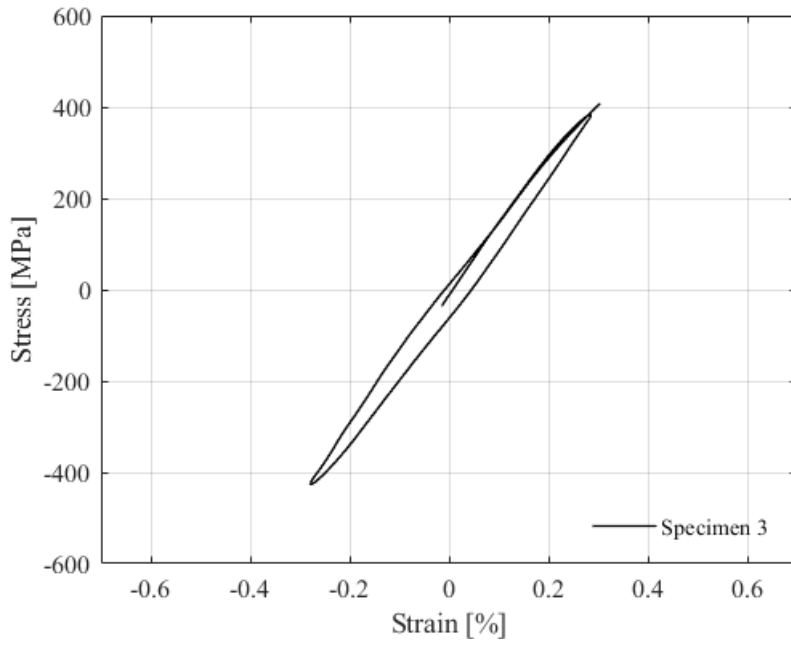
Figure 5.37. Bauschinger test GGG 60 specimen 3.
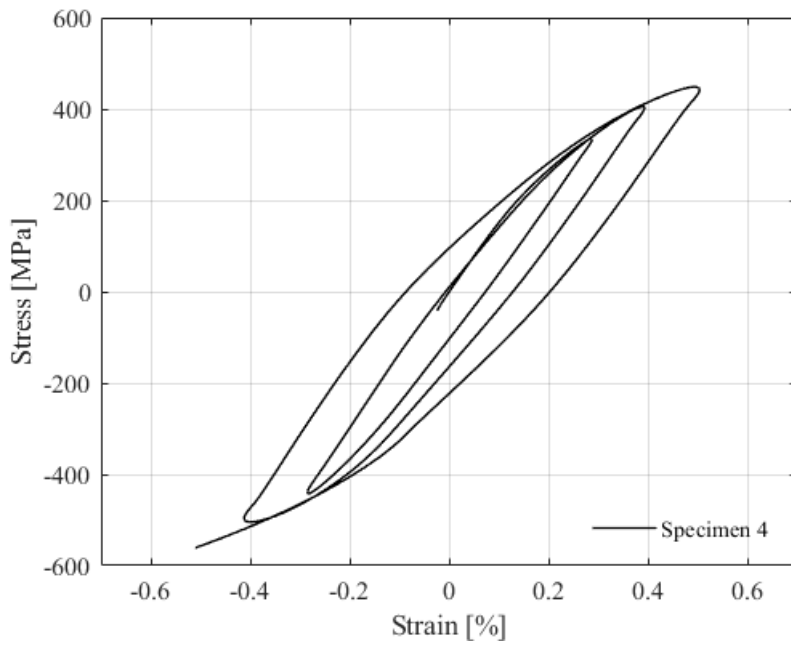
Figure 5.38. Bauschinger test GGG 60 specimen 4.
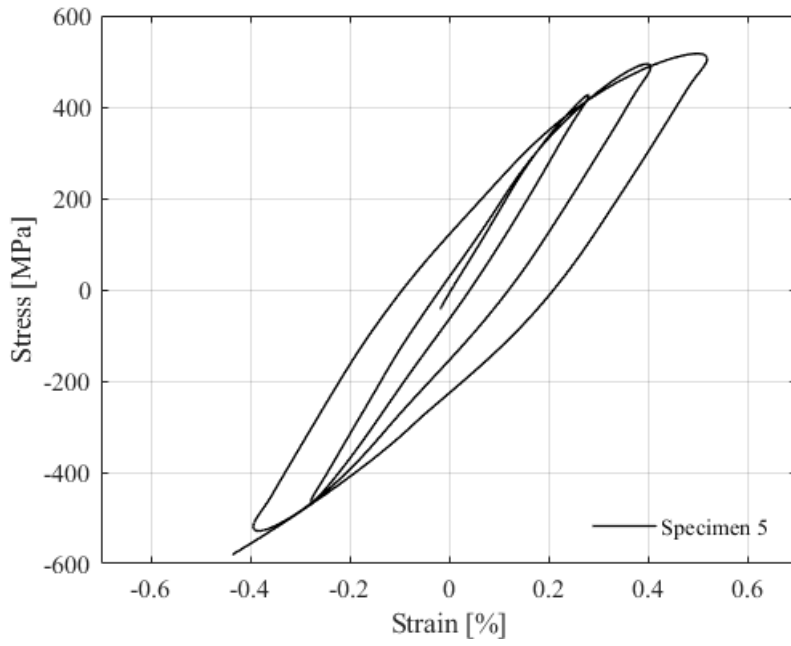
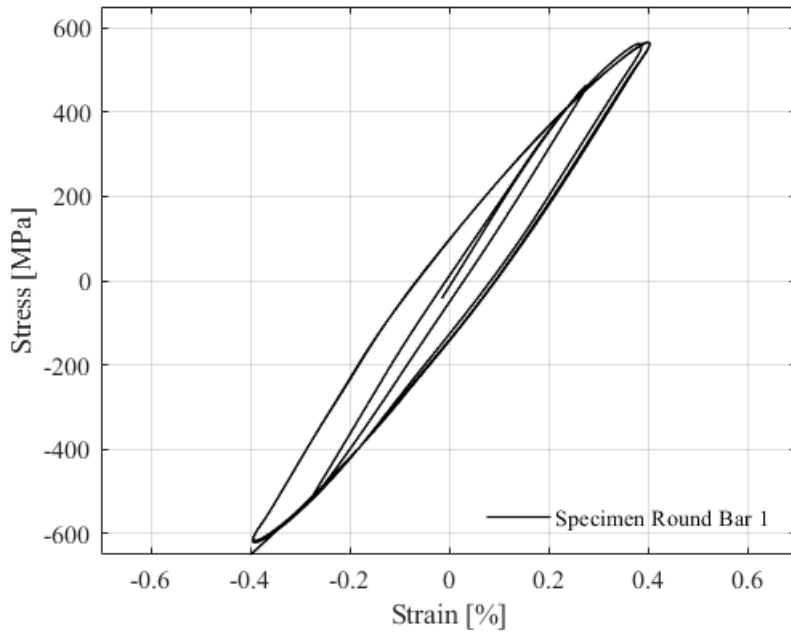**Figure 5.39.** Bauschinger test GGG 60 specimen 5.
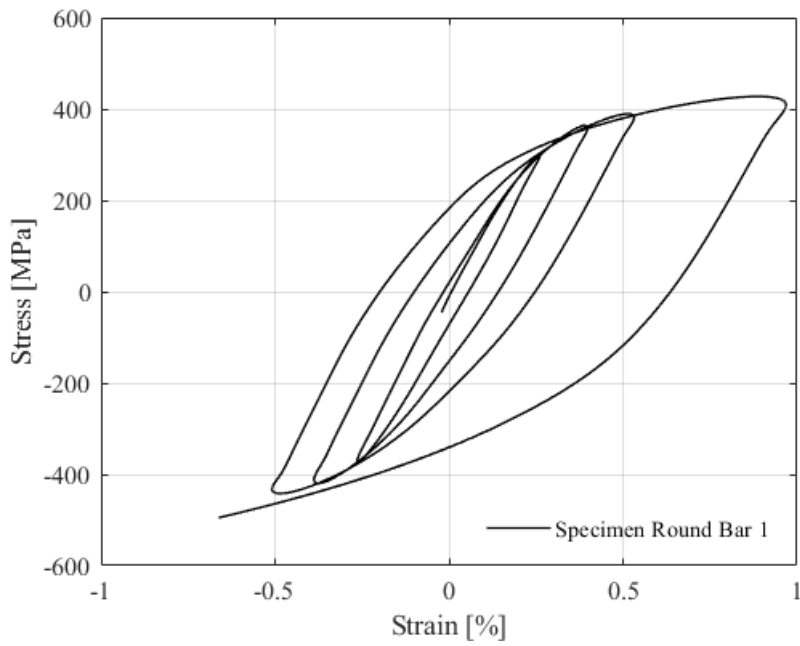
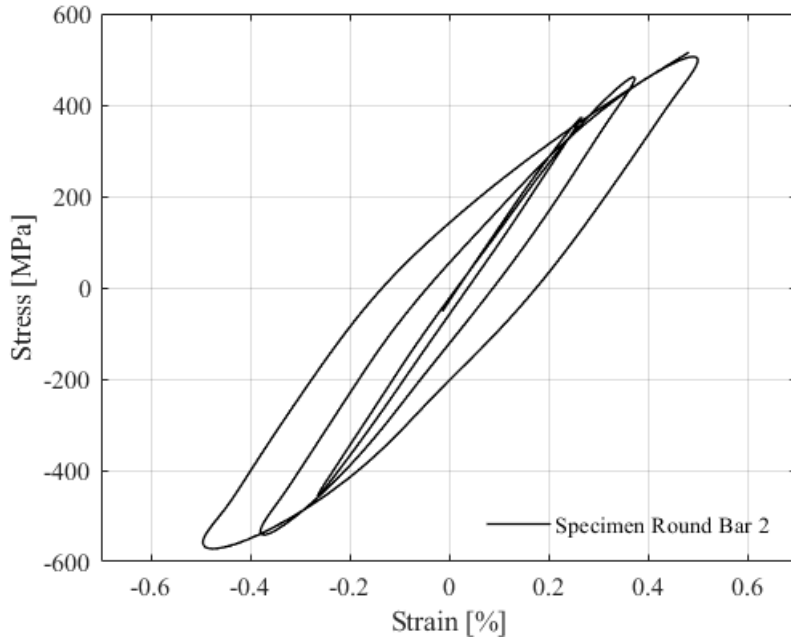**Figure 5.40.** Bauschinger test GGG 60 round bar specimen 1.
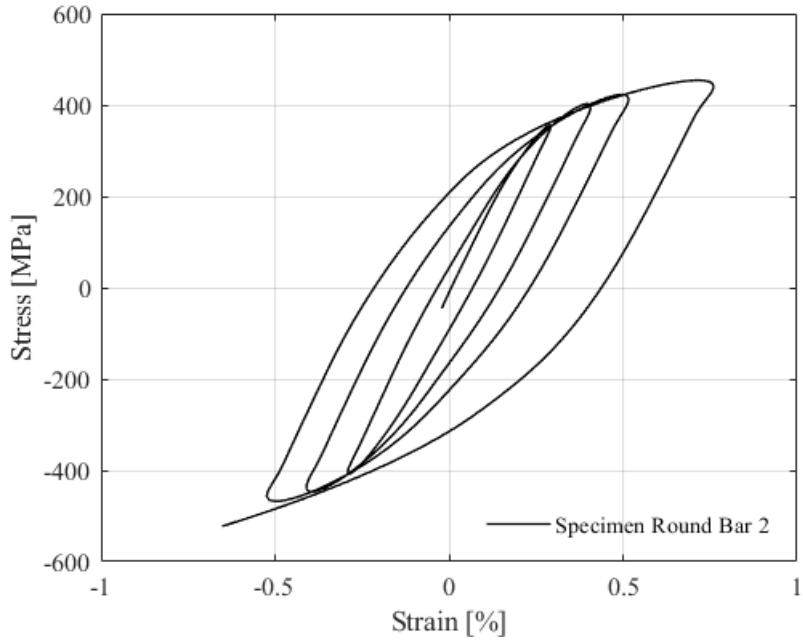
**Figure 5.41.** Bauschinger test GGG 60 round bar specimen 2.
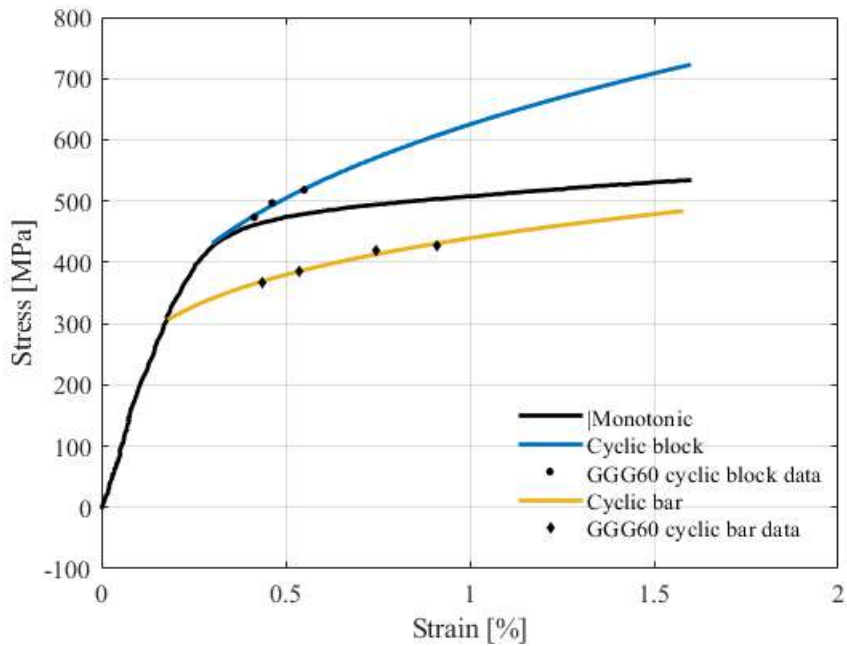
Figure 5.42. Cyclic and monotonic stress–strain curves for GGG60.

In the GGG60 Bauschinger effect, samples 2 and 3 do not complete the test. Sample 3 has an internal defect that leads to the premature rupture of the material until the same reaches plastic strain. Specimen 2 fracture before reaching 0.5% strain what also happened in a tensile test sample.

Samples 1, 4, and 5 had similar behavior reaching stress levels around 500MPa in tension and 500MPa in compression. The behavior of the stress level being similar in tension and

compression was also compatible with the GGG40 obtained result. The expected was the compressive stress levels were higher due to the capacity of the material to resist compressive loads.

The round bar samples had an unexpected behavior, where the stress levels were lower than in block specimens. This behavior occurs due to the amount of pearlite content in the round bar. From the figure 5.42 is possible to visualize the ferrite impact in the sample. In cyclic conditions, GGG60 has a tendency to hardening although round bar specimens soften under these conditions. For block samples $K = 625.1$, $n = 0.309$, $R^2 = 0.9617$. For round bar specimens $K = 439.4$, $n = 0.2106$, $R^2 = 0.9776$.

Figures 5.43 to 5.47 present the tensile test results for GGG70. Figure 5.48 presents a comparison between all the GGG70 test results.
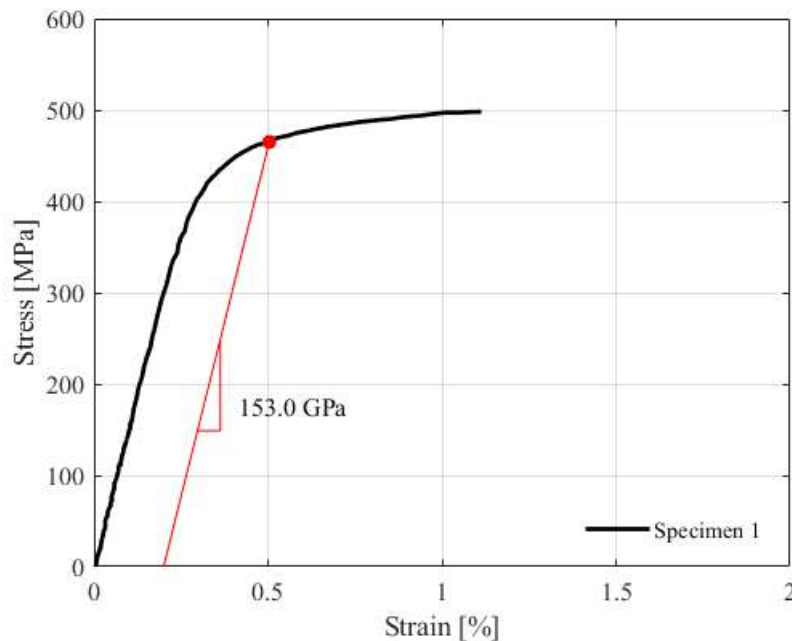
Figure 5.43. Traction test GGG70 specimen 1.
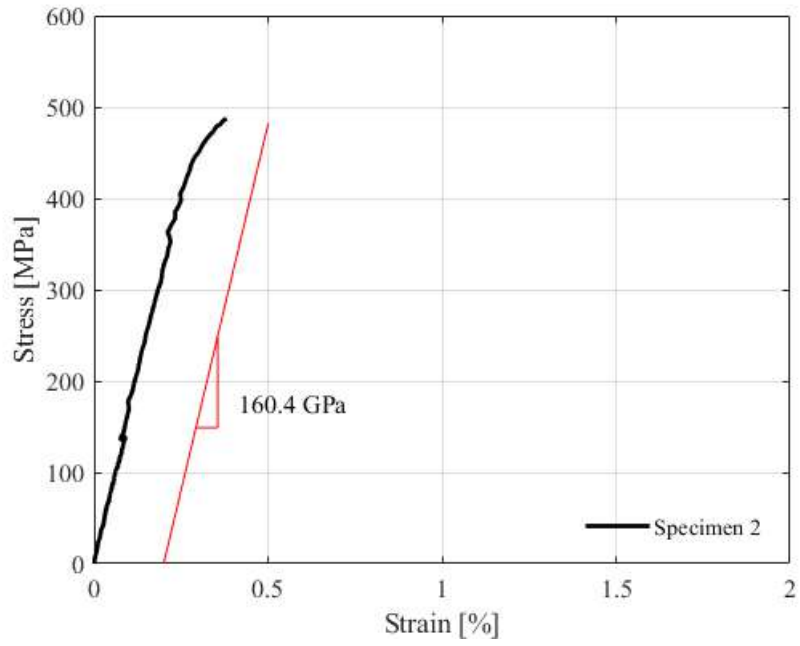
Figure 5.44. Traction test GGG70 specimen 2.
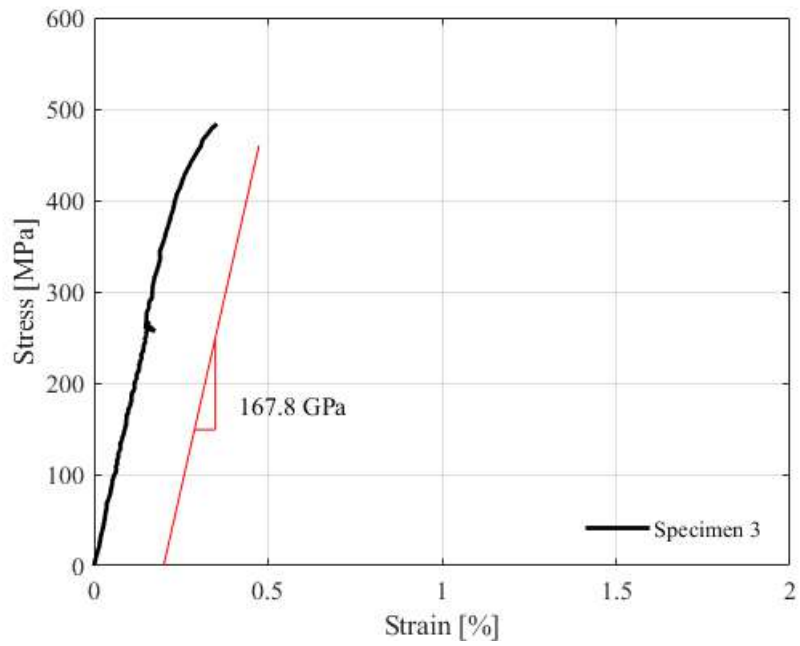
Figure 5.45. Traction test GGG70 specimen 3.
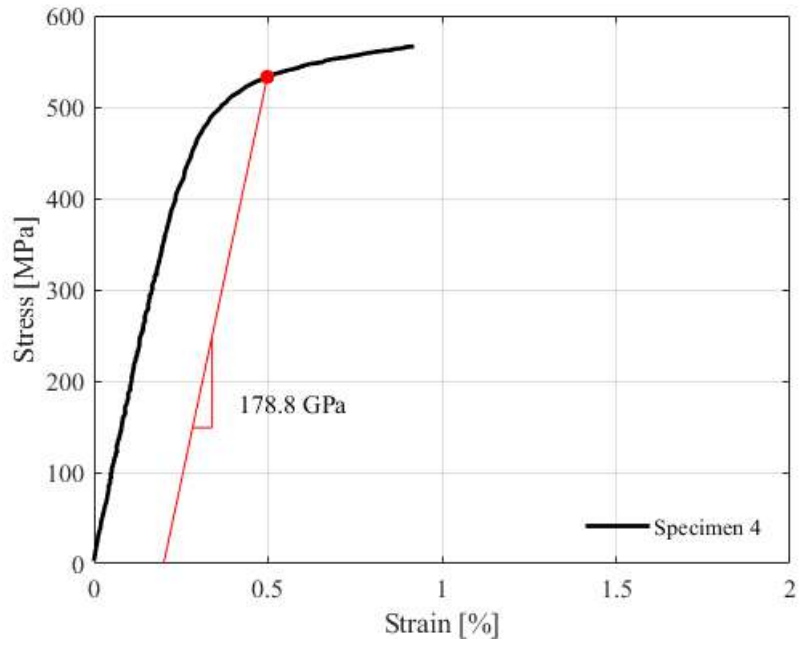
Figure 5.46. Traction test GGG70 specimen 4.
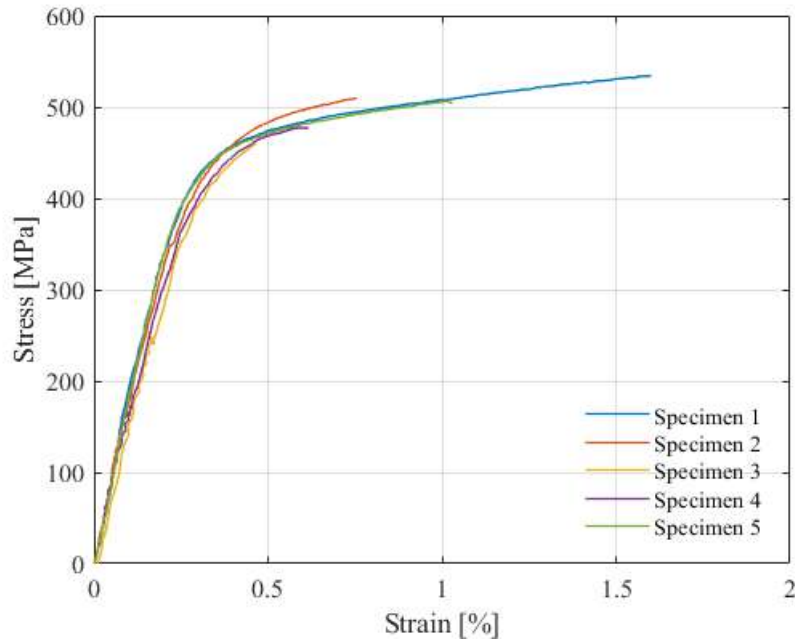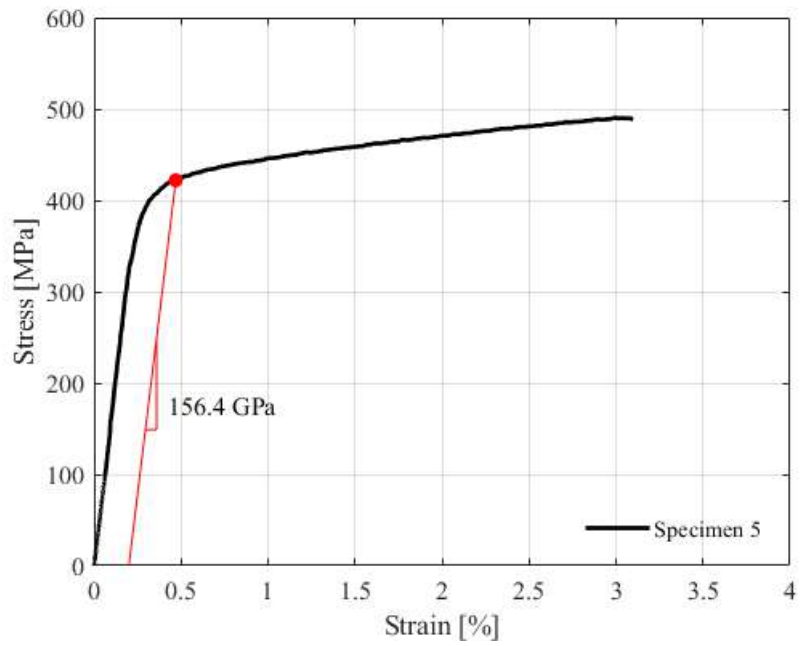

Figure 5.47. Traction test GGG70 specimen 5.
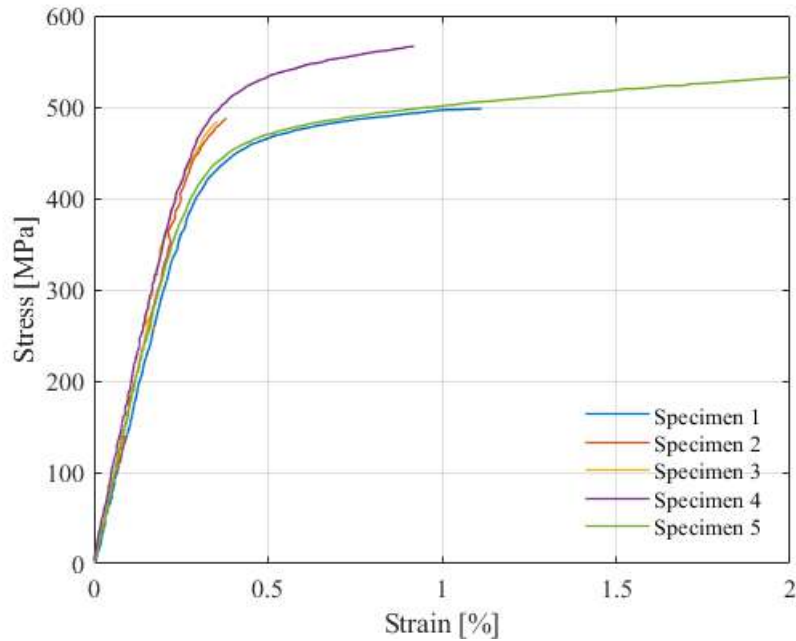
Figure 5.48. Traction test GGG70; comparison of all specimens.

In the GGG70 tensile tests, samples 2 and 3 fractured before reaching the yield limit. There was found to be a casting defect in the sample. Small air bubbles in the specimens caused a stress concentration point that caused the premature break. Specimens 2, 3, and 4 tend to show a similar behaviour, but with higher yield points and ultimate strength.

Table 5.8 summarises the GGG70 tensile test results. It is possible to observe that the edge specimens (1 and 5) have good elongation, in agreement with the literature data. This behaviour seems to be very present in NCI specimens. The elastic modulus varies between 150 GPa and 180 GPa, even in the samples with internal defects.

Table 5.8. GGG70 test results.

	Spec. 1	Spec. 2	Spec. 3	Spec. 4	Spec. 5	SD
σ_{yield} (MPa)	465	-	-	533	467	31.594
σ_{ut} (MPa)	498.1	487.6	483.7	566.3	539.1	24.333
E (GPa)	153.0	160.4	167.8	178.8	163.7	8.541
Max. Elong. (%)	1.113	0.3808	0.353	0.9196	2.276	0.699
Hardness (HV)	242.1	260.7	275.3	250.3	244.0	12.287

Table 5.9 summarizes GGG70 round bar test results.

Table 5.9. GGG70 round bar test results.

	Spec. 1	Spec. 2	Spec. 3	SD
σ_{yield} (MPa)	-	-	562	-
σ_{ut} (MPa)	223.3	444.9	650.2	174.324
E (GPa)	136.4	162.3	154.4	10.838
Max. Elong. (%)	0.1762	0.3189	1.579	0.630
Hardness (HV)	277.4	272.2	275.2	2.0102

The GGG70 round bar samples have not obtained satisfactory results only specimen 3 exceed the yield limit. The round bar casting has poor quality when compared to block casting. The round bar casting leads to internal defects and material embrittlement. Round bar specimen 3 has ultimate stress greater than all block specimens due to the amount of pearlite in the bar samples. One noted that the hardness results are in agreement with the GGG40. Due to the bar cross-section being thinner the cooling rate is higher than in the block, which causes the material hardening. Table 5.10 presents the GGG70 microindentation results.

Table 5.10. GGG70 microindentation test results.

	Hardness (HV)		
	Ferrite	Pearlite	Graphite
Block	246	372	65
Bar	224	444	100

By the microindentation test, the phenomenon of pearlite content being harder in round bar samples than in block samples is confirmed one more time. As explained in GGG40, the high cooling rate promotes the pearlite hardness by the decreases of interlamellar distance. One noted that graphite particles are also harder in round bar samples than in block samples, the effect is the same in pearlite, the carbon diffusion decrease, and graphite becomes harder.

Figure 5.49 plots the relation between the nodule density and maximum stress in GGG70. The obtained data have some dispersion due to specimens 2 and 3 failing before reaching the yield limit. Even with the dispersion of data, the tendency to have greater resistance with a greater density of nodules was repeated.
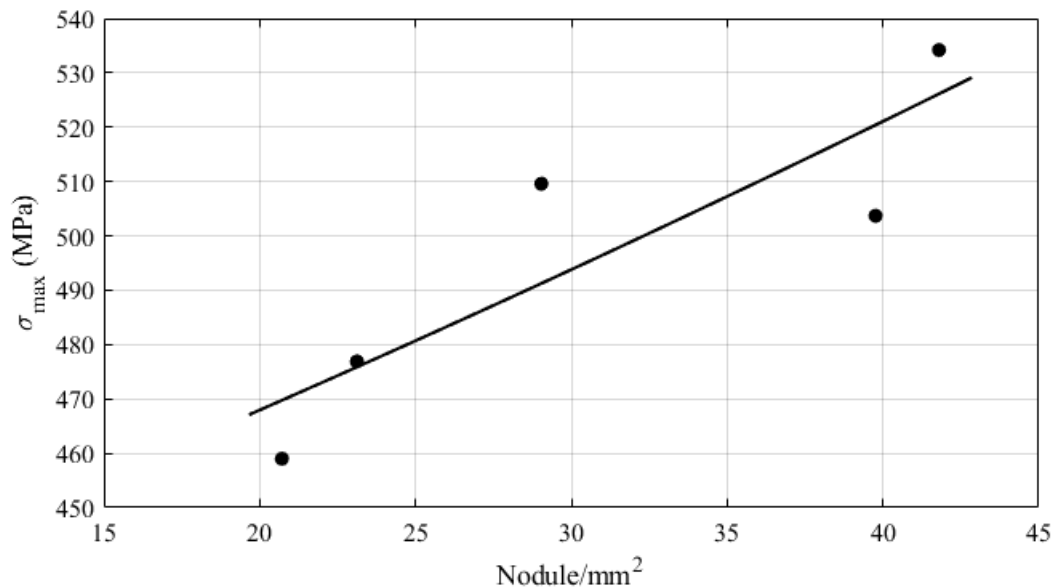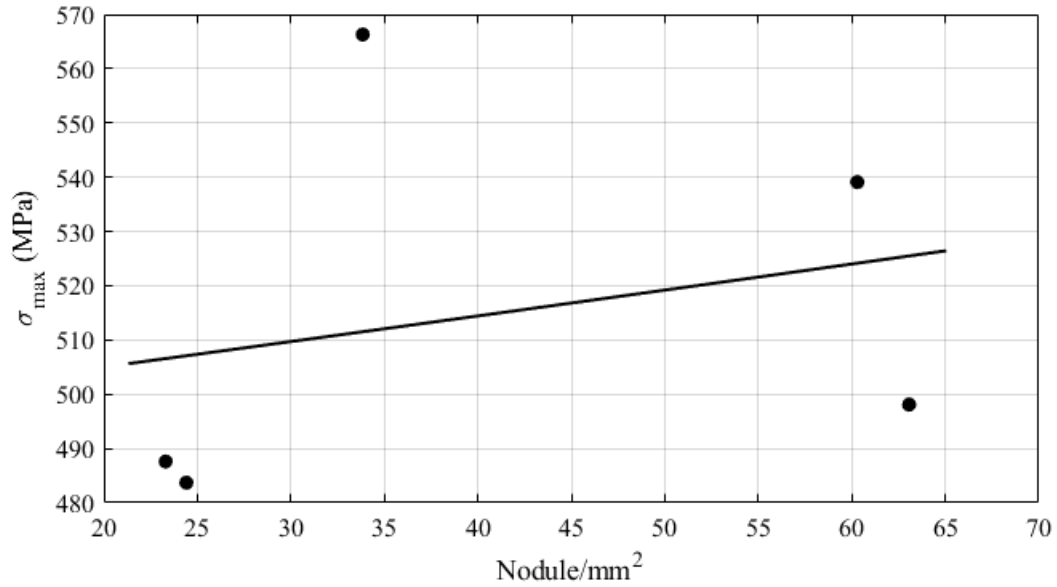
Figure 5.49. Relation between nodule density and maximum stress in NCI GGG 70.

Figure 5.50 to figure 5.56 show the Baushinger effect test for GGG70 block and round bar specimens. The tests followed the standard rules and have been performed in the same conditions as GGG40 and GGG60. Figure 5.57 compares the monotonic and cyclic behavior for GGG70 specimens.
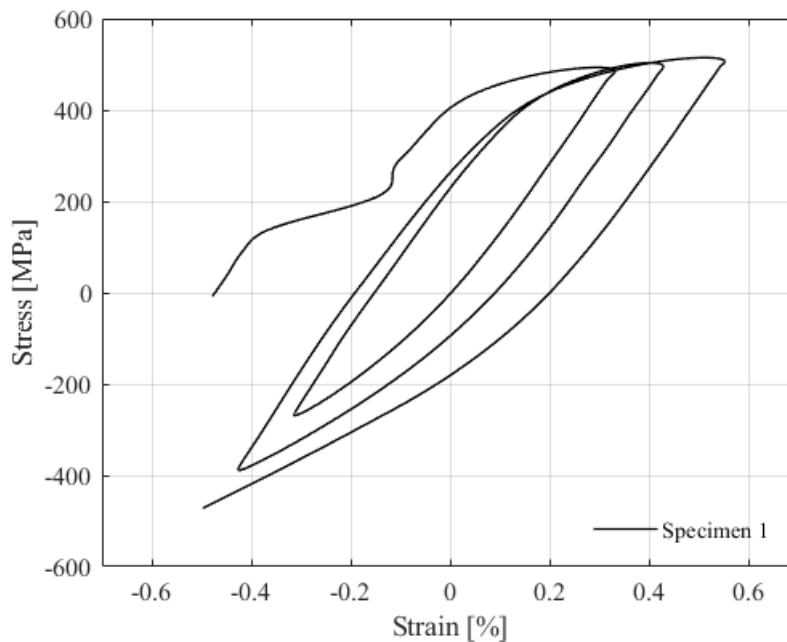
Figure 5.50. Bauschinger test GGG 70 specimen 1.
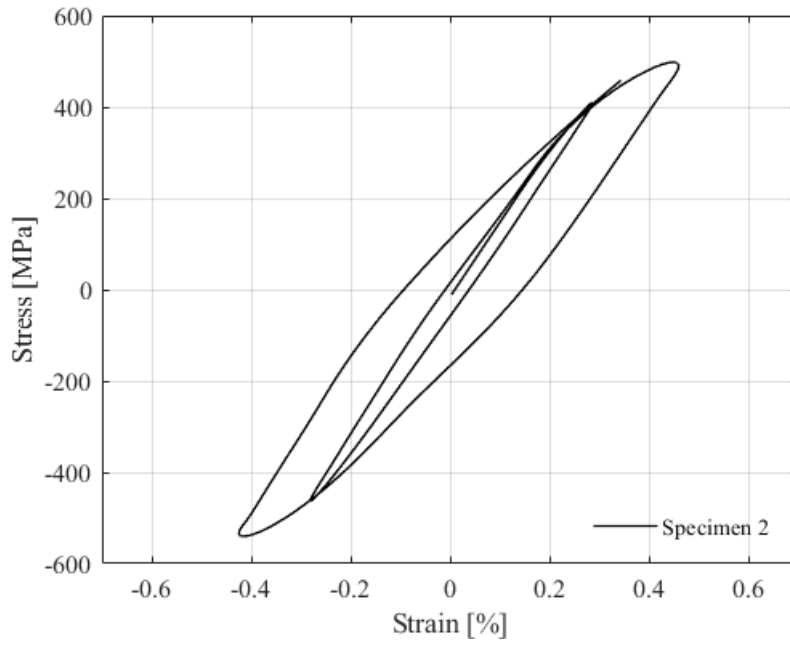
Figure 5.51. Bauschinger test GGG 70 specimen 2.
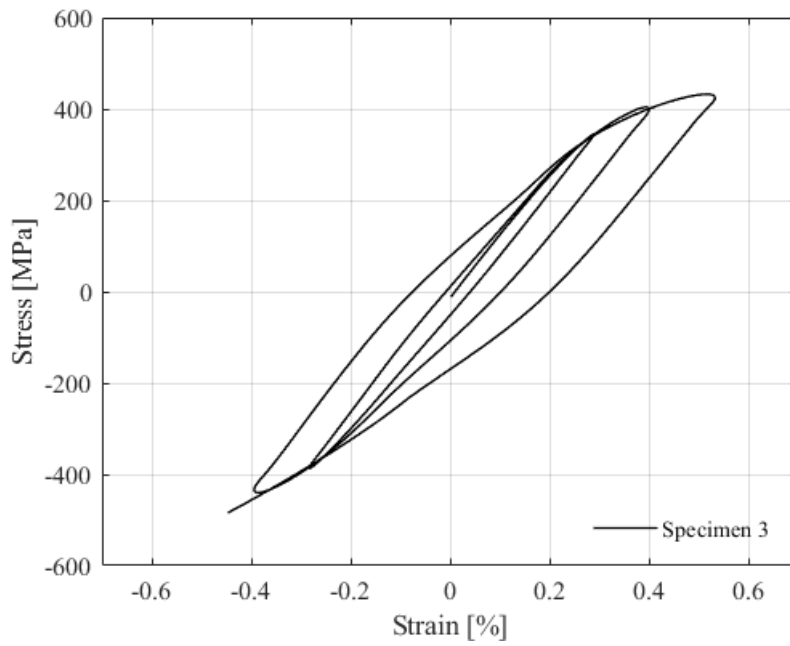
Figure 5.52. Bauschinger test GGG 70 specimen 3.
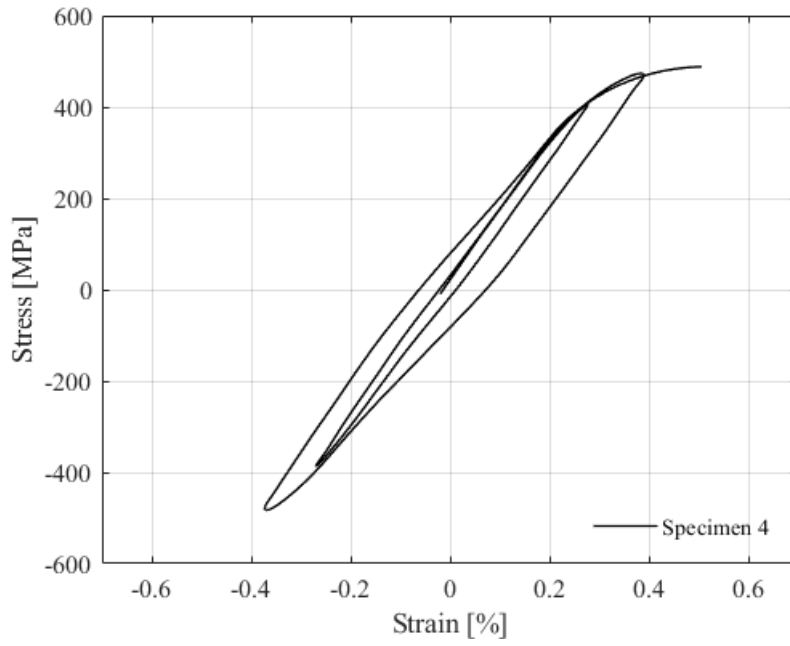
Figure 5.53. Bauschinger test GGG 70 specimen 4.
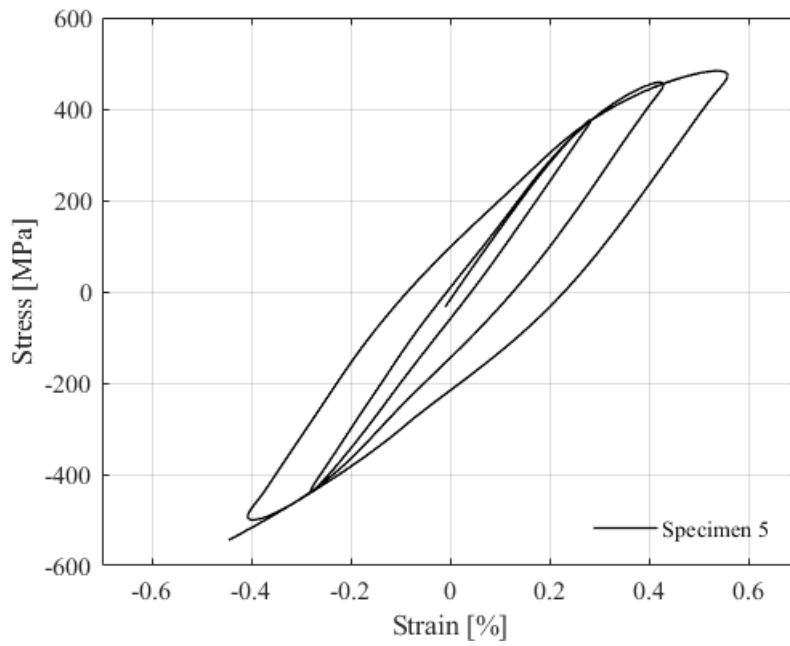
Figure 5.54. Bauschinger test GGG 70 specimen 5.
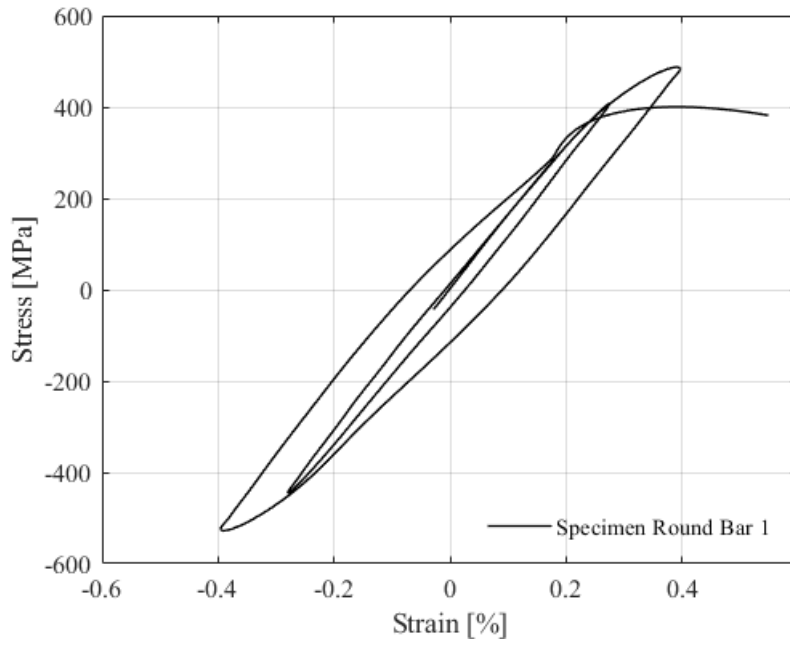
Figure 5.55. Bauschinger test GGG 70 round bar specimen 1.
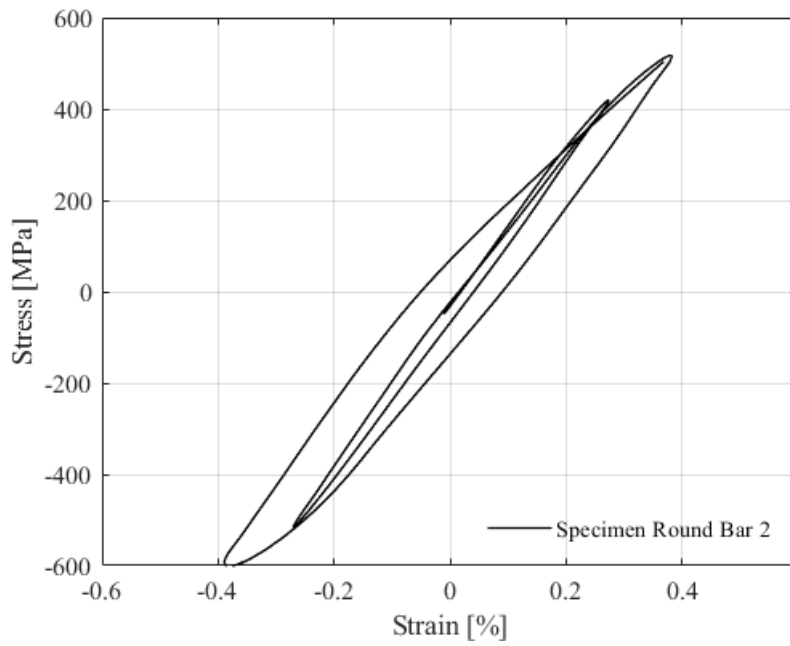
Figure 5.56. Bauschinger test GGG 70 round bar specimen 2.
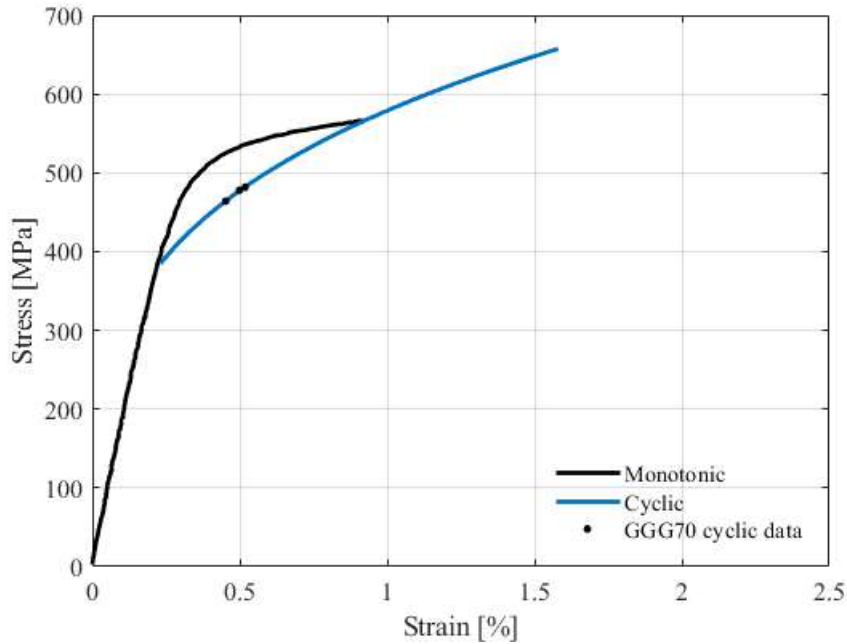
Figure 5.57. Cyclic and monotonic stress–strain curves for GGG70.

Bauschinger effect specimen 1 had a strain gage slippery what causes the uncommon graph. The slippage invalidates the obtained data in this test. Specimens 3 and 5 were capable to perform the complete test. The behavior between the samples is a bit different concerning the stress levels reached. By the tensile test, block specimen 3 does not reach the yield stress which indicates a possible internal problem in this block region that could affect the Bauschinger effect specimen 3. Round bar specimens seems to be more resistant in the first cycle but had a fracture before completing the test.

The Bauschinger effect test returns specific data points that possibilities for the comparison between cyclic and monotonic behavior. The values returned for GGG70 were $K = 578.9$ and $n = 0.2782$ with $R^2 = 0.9921$. GGG70 under cyclic conditions tends to have a hardening behavior.

Figure 5.58 show the samples of NCI GGG40 etched with 2% nital with an image magnification of 100x and 400x to evaluate the details of the microstructure.
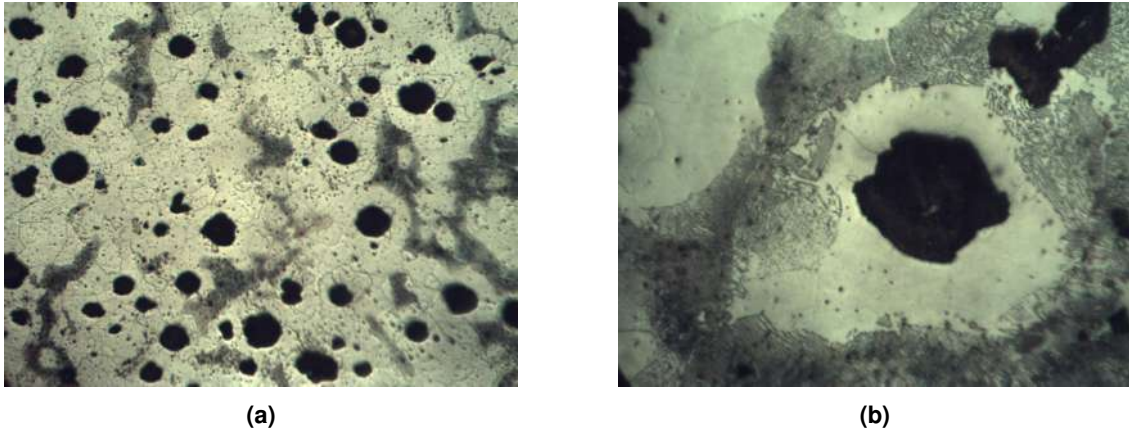
Figure 5.58. Microstructure of NCI GGG40 etched with 2% nital. (a) 100x magnification. (b) 400x magnification.

It is possible to observe the ferrite/pearlite ratio in the GGG40, where the ferrite volume is predominant. There is also an alignment of the nodules, which can be seen in other samples of GGG40. The main consequence of this defect is the drastic reduction in elongation, since the fracture facilitates this preferential distribution of the nodules. Leakage at high temperatures can accentuate this trend.

In the 400x magnification image, an undesirable phase in the microstructure is visible. Undesirable phases usually come from the chemical composition and inadequate processing, constituting mainly particles of high hardness and non-metallic inclusions. In Figure 5.58b it is possible to see the presence of cementite. The sample was taken from a section close to the block edge, so the formation of cementite may be associated with a high cooling rate. Despite the aforementioned defects, the material analysed reached stress levels higher than expected according to the literature. This high level of strength can be explained by the addition of copper, which promotes the hardening of the ferrite.

Figure 5.59 shows the computational image analysis of GGG40 block sample and figure 5.60 shows the computational image analysis of GGG40 round bar sample.

Figure 5.59. Computational image analysis of NCI GGG40 with graphite, ferrite and pearlite identification.

Figure 5.60. Computational image analysis of NCI GGG40 with graphite, ferrite and pearlite identification for round bar specimens.

Comparing the figures 5.59 and 5.60, the microstructural differences in the samples are remarkable. Even being the same material, casting in different geometries is a significant factor in obtaining the desired microstructure and mechanical properties. The formation of nodules in the cast bar is affected by the cooling rate. The round bar has small graphite nodules but in greater quantity, while the block samples have larger graphite nodules. The amount of the pearlite identified in the circular bar samples was higher than expected. Pearlite values are around 70%. These values can be observed in the x tables for the GGG40 samples taken from the block and in the x table for the samples taken from the circular bar.

Tables 5.11 to 5.12 summarise the results obtained from the developed routine.

Table 5.11. GGG40 computational image analysis results.

	sample 1	sample 2	sample 3	sample 4	sample 5
Nodule/mm^2	67.14	40.69	39.77	48.27	36.81
Nod. Graphite %	87.06	81.33	80.15	83.88	82.74
Avg. Area (μm^2)	2039.94	3253.46	2816.68	2227.60	3680.56
Sphericity	0.8975	0.8175	0.8977	0.9168	0.8829
Compactness	0.9376	0.9011	0.9359	0.9460	0.9419
Roundness	0.7375	0.6532	0.7118	0.7272	0.6998
Eccentricity	0.6165	0.6688	0.6337	0.6187	0.6405
Graphite %	13.93	13.76	11.93	12.72	14.53
Ferrite %	62.39	61.04	68.74	73.02	73.39
Pearlite %	23.68	25.20	19.33	14.26	12.07

Table 5.12. GGG40 round bar samples computational image analysis results.

	Sample 1	Sample 2	Sample 3
Nodule/mm^2	85.26	75.65	69.73
Nod. Graphite %	90.96	91.70	90.05
Avg. Area (μm^2)	13767.78	1608.02	1677.54
Sphericity	0.9586	0.9549	0.9350
Compactness	0.9752	0.9755	0.9607
Roundness	0.7857	0.7774	0.7583
Eccentricity	0.5535	0.5668	0.5832
Graphite %	12.30	15.55	13.97
Ferrite %	15.90	13.51	22.22
Pearlite %	71.80	70.94	63.81

Figure 5.61 presents the GGG60 microstructure etched with 2% nital.

(a)   (b)
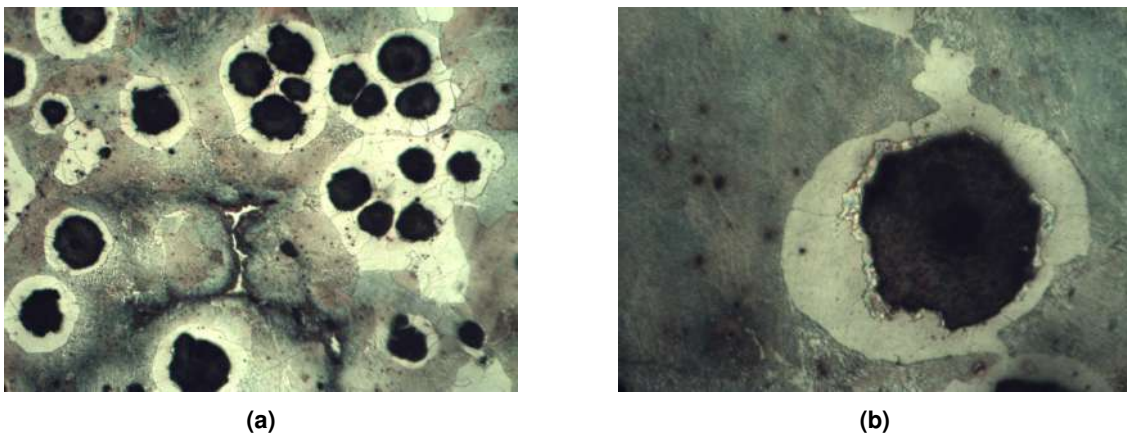
Figure 5.61. Microstructure of NCI GGG60 etched with 2% nital. (a) 100x magnification. (b) 400x magnification.

The matrix is predominantly pearlitic, with ferrite arranged around graphite nodules, in accordance with Jost *et al.* (2017). The microstructure is composed of a graphite conglomerate, which in this case could mean a weak material point.

Figure 5.62 shows the phase separation for GGG60 in the developed routine, which has identified a majority of pearlite content, and the graphite conglomerate particles are surrounded by ferrite.
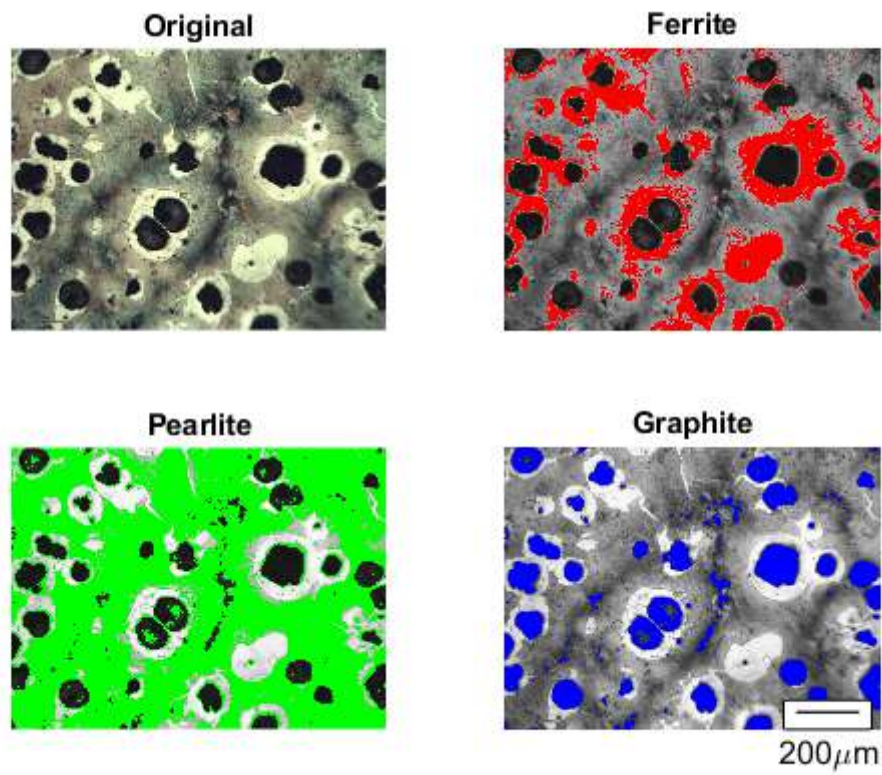
Figure 5.62. Computational image analysis of NCI GGG60 with graphite, ferrite and pearlite identification.
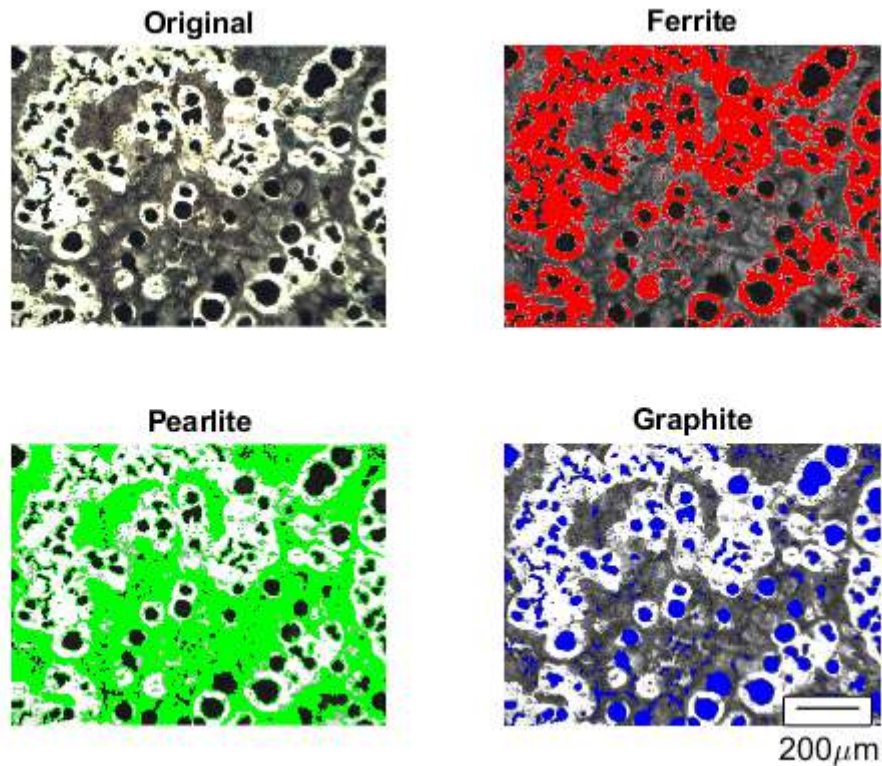
Figure 5.63. Computational image analysis of NCI GGG60 with graphite, ferrite and pearlite identification for round bar specimens.

In the specimens removed from the block, the majority of the graphite particles are considered nodular, which is different from the samples manufactured from round bars that contain a large number of vermicular graphite particles. The round bar microstructure obtained was unforeseen due to the graphite shape and the amount of pearlite in the sample. Table 5.13 presents the results obtained by the image analysis for GGG60 block specimens and table 5.14 for GGG60 round bar specimens.

Table 5.13. GGG60 computational image analysis results.

	sample 1	sample 2	sample 3	sample 4	sample 5
Nodule/mm^2	41.80	29.04	20.71	23.12	39.77
Nod. Graphite %	93.05	90.32	97.03	96.20	92.07
Avg. Area (μm^2)	3101.20	4029.84	6441.04	4916.48	2985.96
Sphericity	0.9118	0.8876	0.8916	0.8765	0.8881
Compactness	0.9383	0.9341	0.9389	0.9324	0.9279
Roundness	0.7558	0.7346	0.7711	0.7557	0.7471
Eccentricity	0.5842	0.6097	0.5714	0.5861	0.5937
Graphite %	15.10	14.02	14.55	13.30	14.36
Ferrite %	25.42	19.06	31.02	25.60	34.82
Pearlite %	59.48	66.92	54.43	61.10	50.82

Table 5.14. GGG60 round bar samples computational image analysis results.

	Sample 1	Sample 2	Sample 3
Nodule/mm^2	63.44	81.93	64.18
Nod. Graphite %	62.86	69.17	87.88
Avg. Area (μm^2)	1285.24	963.88	1619.82
Sphericity	0.7984	0.8466	0.8663
Compactness	0.8555	0.8913	0.9120
Roundness	0.6328	0.6712	0.7357
Eccentricity	0.6809	0.6531	0.5960
Graphite %	14.46	13.68	13.63
Ferrite %	33.46	32.42	6.35
Pearlite %	52.07	53.90	80.02

The GGG70 microstructure is presented in Figure 5.64a with 100x magnification and with 400x magnification in Figure 5.64b.

(a)

(b)
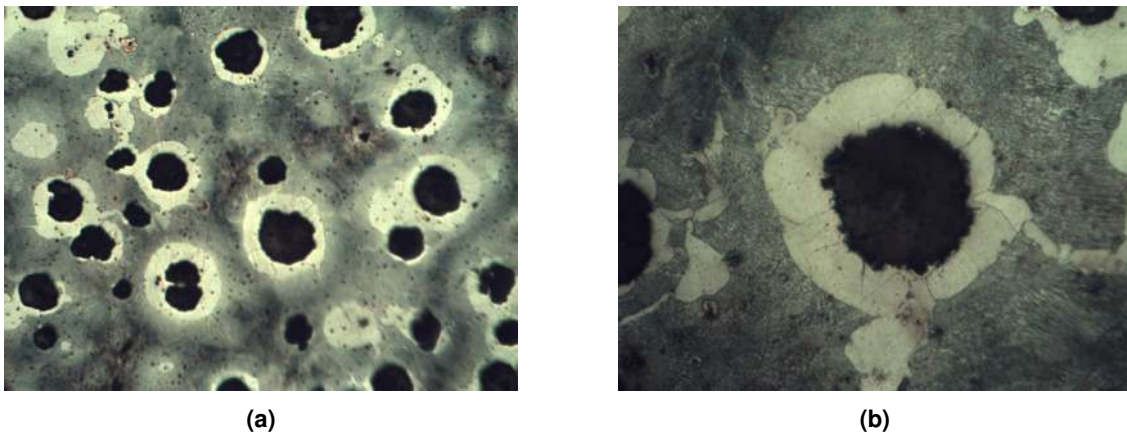
Figure 5.64. Microstructure of NCI GGG70 etched with 2% nital. (a) 100x magnification. (b) 400x magnification.

The matrix is predominantly pearlitic. This sample clearly shows the bull's eye structure. The graphite nodules are surrounded by ferritic content. The distribution of graphite nodules seems to be better than in the GGG60 samples, without nodule conglomeration that could embrittle the sample.

Figure 5.65 and figure 5.66 shows the phase counting by the developed routine.
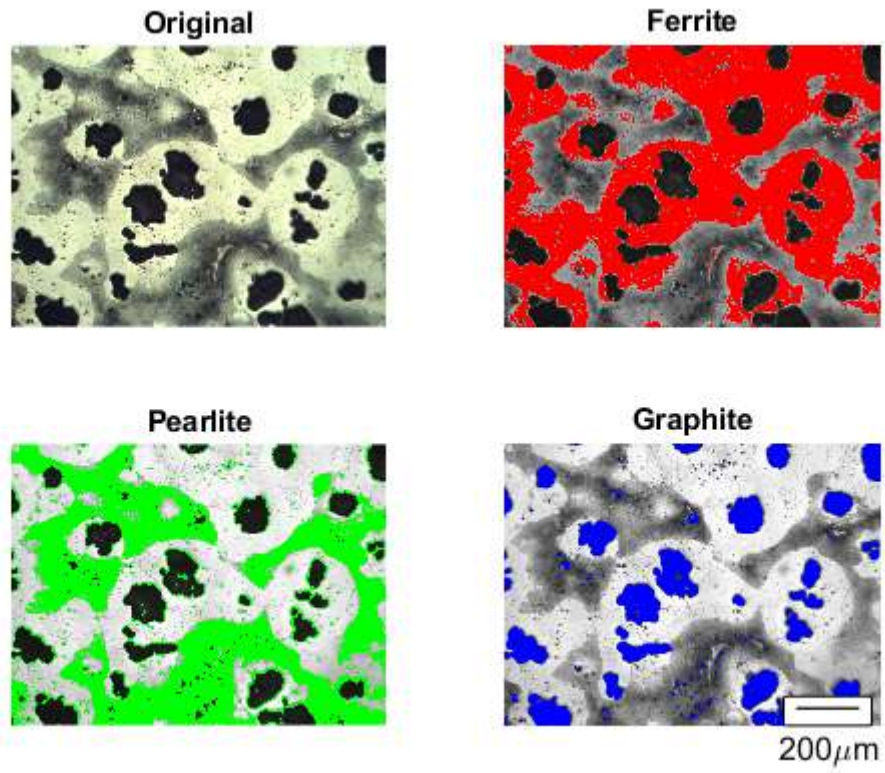
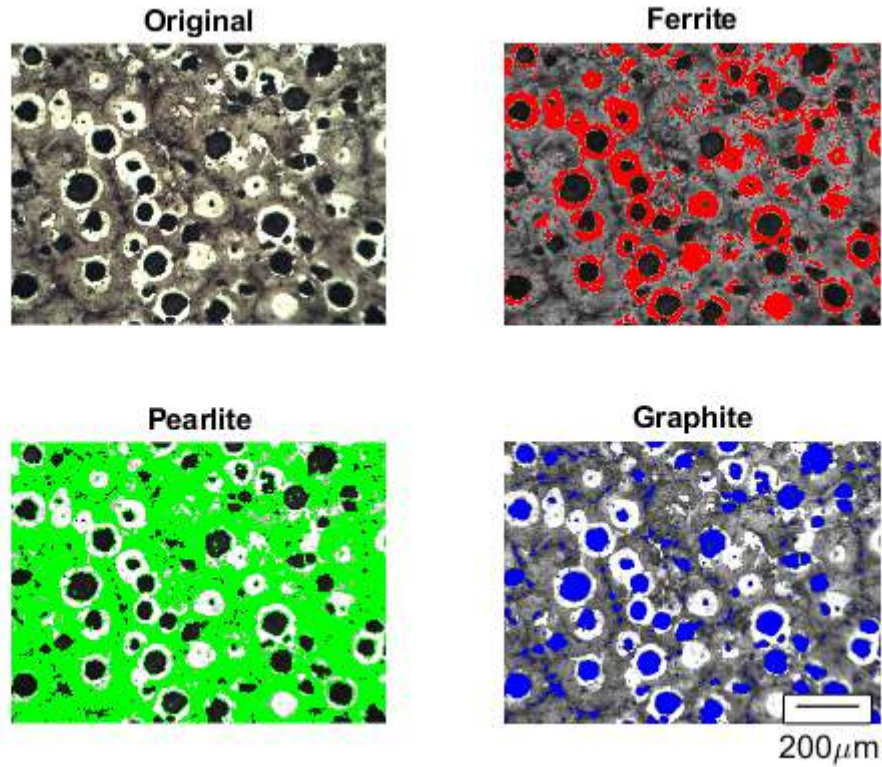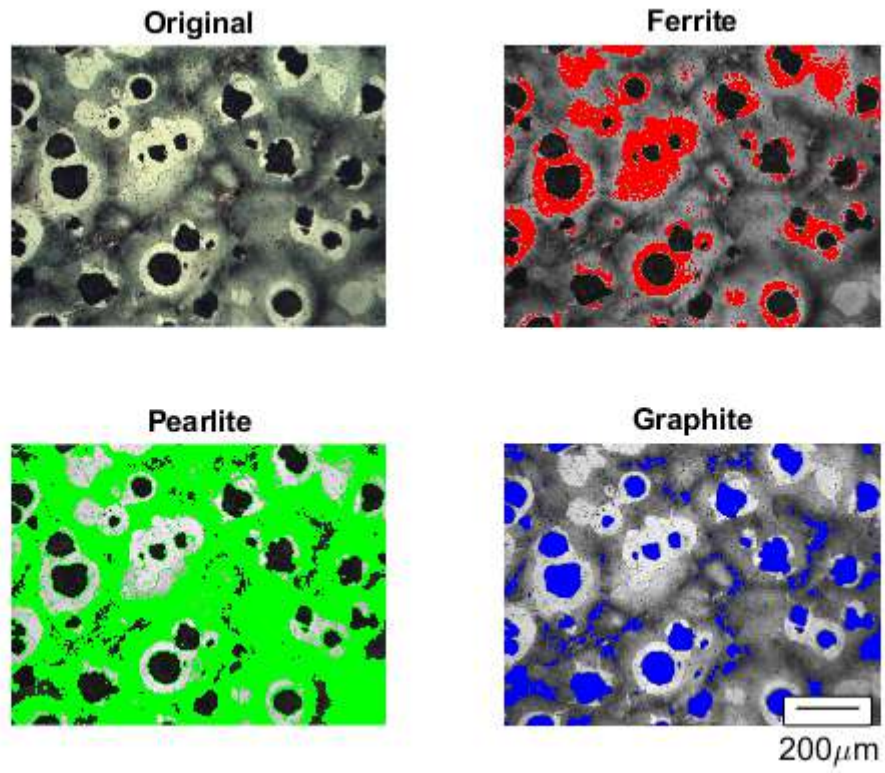**Figure 5.65.** Computational image analysis of NCI GGG70 with graphite, ferrite and pearlite identification.
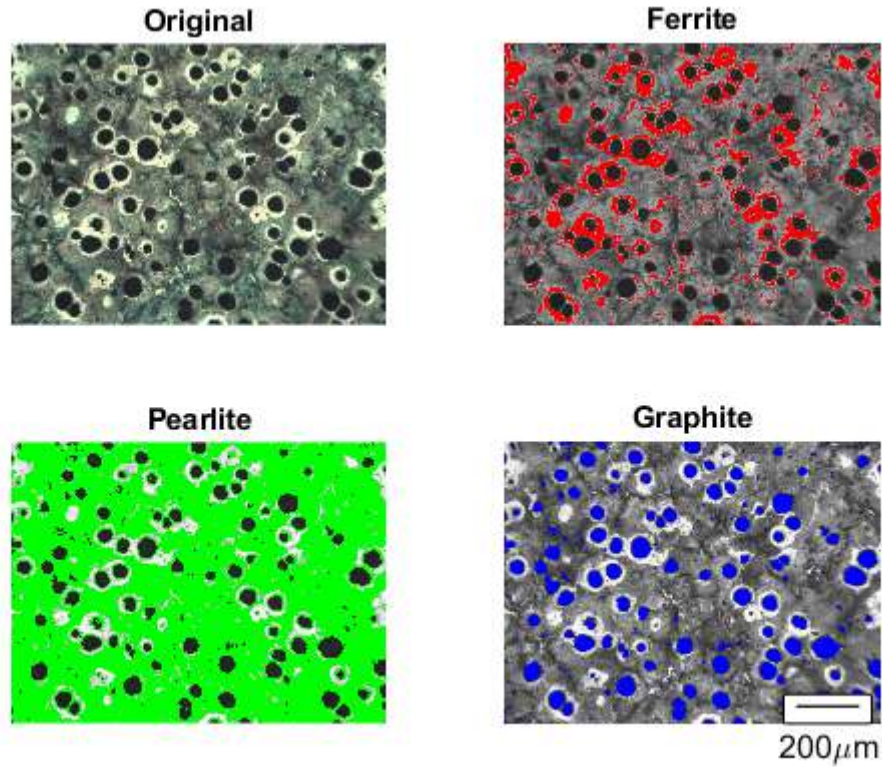
Figure 5.66. Computational image analysis of NCI GGG70 with graphite, ferrite and pearlite identification for round bar specimens.

In GGG70 the majority of the graphite particles have a nodular shape, and the ferrite content is identified around the graphite particles. The green area presents the pearlitic phase and it is clear that the presence of pearlite is greater in the sample, in agreement with the tested material. The ferrite amount in round bar samples is less than in block specimens. This behavior has been seen in other material samples. Round bar samples have more nodular particles with a large number of nodules. Table 5.15 and 5.16 present the results obtained from the developed routine for GGG70 block specimens and round bar specimens respectively.

Table 5.15. GGG70 computational image analysis results.

	sample 1	sample 2	sample 3	sample 4	sample 5
Nodule/mm^2	63.07	23.30	24.41	33.85	60.29
Nod. Graphite %	92.58	89.21	95.18	90.34	93.15
Avg. Area (μm^2)	1900.14	4049.86	3927.24	2692.12	1784.82
Sphericity	0.9037	0.8226	0.8710	0.8776	0.8931
Compactness	0.9397	0.9220	0.9318	0.9299	0.9291
Roundness	0.7711	0.7185	0.7595	0.7332	0.7632
Eccentricity	0.5661	0.6090	0.5808	0.6106	0.5713
Graphite %	17.69	13.63	15.84	15.46	18.74
Ferrite %	22.41	16.53	11.16	17.00	25.42
Pearlite %	59.90	69.84	73.00	67.54	55.84

Table 5.16. GGG70 round bar samples computational image analysis results.

	Sample 1	Sample 2	Sample 3
Nodule/mm^2	71.95	72.13	69.91
Nod. Graphite %	90.66	93.10	88.92
Avg. Area (μm^2)	1512.64	1547.04	1629.04
Sphericity	0.9643	0.9605	0.9442
Compactness	0.9802	0.9779	0.9665
Roundness	0.7951	0.7965	0.7813
Eccentricity	0.5434	0.5443	0.5581
Graphite %	12.03	12.01	14.80
Ferrite %	12.33	9.31	15.68
Perlite %	75.64	78.68	69.52

It is important to note that specimens 1 and 5 for all the NCI evaluated herein, as shown in Tables 5.2, 5.5 and 5.8, presented a significantly superior elongation when compared to the remaining specimens, located at the cast iron block edges.

Through the EDS analysis, one could note that Fe was homogeneously distributed between ferrite and pearlite. Also, a small amount of Fe was noticeable in the center of the graphite nodules. Carbon was seen to be concentrated almost entirely on the graphite nodules. The presence of C was also perceptible on the ferrite, pearlite but only in small amounts.

Table 5.17 and 5.18 present the results obtained from the developed routine for block specimens and round bar specimens respectively.

Table 5.17. Final results average for NCI GGG40, 60 and 70 block specimens.

	GGG40	GGG60	GGG70
Hardness (HV)	197.9±3.0%	240.7±5.1%	254.7±4.8%
Nodule/mm^2	46.53±23.5%	30.89±27.7%	40.99±42.2%
Nod. Graphite (%)	83.03±2.9%	93.74±2.7%	92.09±2.3%
Avg. Area (μm^2)	2813.85±21.5%	4294.90±29.8%	2870.84±33.6%
Sphericity	0.8825±3.9%	0.8911±1.3%	0.8736±3.2%
Compactness	0.9325±1.7%	0.9343±0.4%	0.9305±0.6%
Roundness	0.7059±4.2%	0.7529±1.6%	0.7491±2.7%
Eccentricity	0.6356±3.0%	0.5890±2.1%	0.5875±3.2%
Graphite (%)	13.37±7.0%	14.26±4.2%	16.27±11.0%
Ferrite (%)	67.71±7.7%	27.18±19.8%	18.50±26.8%
Pearlite (%)	18.91±27.0%	58.54±9.5%	65.22±9.8%

Table 5.18. Final results average for NCI GGG40, 60 and 70 bar specimens.

	GGG40	GGG60	GGG70
Hardness (HV)	272.4±3.0%	239.4±10.2%	275.0±0.7%
Nodule/mm^2	76.88±8.3%	69.85±12.2%	71.33±1.4%
Nod. Graphite %	90.90±0.7%	73.30±14.5%	90.89±1.9%
Avg. Area (μm^2)	1551.11±8.6%	1289.65±20.8%	1562.91±3.1%
Sphericity	0.9495±1.1%	0.8371±3.4%	0.9563±0.9%
Compactness	0.9705±0.7%	0.8863±2.6%	0.9749±0.6%
Roundness	0.7738±1.5%	0.6799±6.2%	0.7910±0.9%
Eccentricity	0.5678±2.1%	0.6433±5.5%	0.5486±1.2%
Graphite %	13.94±9.5%	13.92±2.7%	12.95±10.1%
Ferrite %	17.21±21.3%	24.08±52.1%	12.44±20.9%
Perlite %	68.85±5.2%	62.00±20.6%	74.61±5.1%

According to Grenier *et al.* (2014), roundness, sphericity, and compactness are shape factors that can be used as valid methods for estimating the degree of "roundness" of a graphite particle. These data can provide valid support for a standard classification and routine quality control in ductile iron production. An eccentricity parameter can also aid in the nodule characterization, together with the sphericity shape factor. The eccentricity is a property of the ellipse that best fits the spheroid, as it has values that vary between 0 and 1, describing how far is the graphite element shape from being circular. Eccentricity and sphericity are the parameters most influenced by varying magnification.

The differences between block-shaped and bar-shaped cast iron are notable as shown in tables 5.17 and 5.18. The microstructure of bar casting classes has more circular graphite patterns than block casts because the nodules are smaller and do not have enough time to nucleate. GGG60 showed different behavior because it contained a large number of vermicular-shaped graphite particles. A major impact factor was also the percentage of pearlite found in bar-casted samples, being much higher than block samples, especially in GGG40.

A coefficient of variation was used to analyze the dispersion of the results with respect to their mean value. The largest variations found in the measurements resulting from the specimens obtained from the block occurred in the following parameters: nodule density per area, average nodule size, and the pearlite and ferrite phases. For all NCI evaluated herein those dispersions are justifiable due to the specimen position in the casted block. The specimens located on the block edge tend to have a higher cooling rate, which affects the nodule size and promotes the pearlite formation.

In the bar specimens, the largest variation occurs in the average nodule size, and also in graphite, ferrite, and pearlite amount. This phenomenon was noted in both cases, when using block samples and also when using bar samples. It is worth mentioning that the transversal section of the bar sample is thinner when compared to the transversal section of the block sample, resulting in a higher cooling rate for the case of the bar sample. This particular characteristic of the bar sample results in the fact that the shape and sizes of the nodules were more similar, regardless of the sample position on the bar. However, the samples located in

the middle of the bar showed higher ferrite levels than the ones obtained at the extreme ends of the bar, as well as slightly larger sizes of the graphite nodules in these central samples.

Table 5.19 presents the tensile test results for specimens manufactured from the block and the bar.

Table 5.19. Final tensile test results average for NCI GGG40, 60 and 70 bar and block specimens.

		σ_{yield} (MPa)	σ_{ut} (MPa)	E (GPa)	Max. Elong. (%)	ν
GGG40	Block	413.8 $\pm$1.8%	483.3 $\pm$3.6%	161.3 $\pm$5.8%	3.30	0.22
	Bar	-	364.5 $\pm$5.3%	159.1 $\pm$10.4%	0.26	0.20
GGG60	Block	471.7 $\pm$1.5%	506.1 $\pm$5.2%	163.5 $\pm$3.7%	1.00	0.23
	Bar	478.5 $\pm$8.8%	552.1 $\pm$2.7%	146.5 $\pm$2.1%	1.84	0.21
GGG70	Block	488.3 $\pm$6.5%	534.5 $\pm$6.1%	165.2 $\pm$5.2%	1.44	0.23
	Bar	562.0 $\pm$2.4%	650.2 $\pm$3.8%	151.0 $\pm$7.2%	0.69	0.23

The differences in mechanical properties obtained in GGG40, 60, and 70 are noticeable, due to the final casting geometry. The specimens of the block presented more uniform mechanical properties when compared to the bar samples. The elasticity modulus values obtained for the block casting material showed good agreement with the literature. On the other hand, the bar samples showed an increased strength behavior, due to the fact that, in most of the samples, the amount of pearlite obtained was higher in the bar samples.

Table 5.20 shows a comparison between the test data obtained and the results from other authors. The table shows the standard mechanical properties for each nodular cast iron class evaluated in this work.

Table 5.20. NCI mechanical properties comparison.

		σ_{yield} (MPa)	σ_{ut} (MPa)	E (GPa)	ε (%)	Hardness (HB)
	current work	413.80	483.34	161.26	3.303	197
GGG40	Betancur *et al.* (2018)	325	437	181.9	1.6	-
	DIN 1693 (DE)	250	400	169	15	135-180
	current work	471.75	506.10	163.55	1.001	240
GGG60	DIN 1693 (DE)	380	600	174	3	190-270
	current work	488.33	534.50	165.17	1.436	254
GGG70	Karaca (2019)	427.53	795.37	-	5.2	261
	DIN 1693 (DE)	440	700	176	2	225-305

The results obtained in this work were important to understand the nodular cast iron behavior and mechanical properties in heat treatment absence and without cast Y block procedure. Comparing the results with other authors and standards is seen that exist some differences in the obtained results.

The NCI GGG40 does not reach the expected elongation that was approximately 15% according to the German standard DIN 1693. Although the results are quite similar to the obtained by Betancur *et al.* (2018).

GGG60 has results more closer to the established by the standard. Once again the elongation was not expected, however in order to the poor GGG40 elongation, this result was expected.

The GGG70 has as the main difference the yield stress that was greater than the expected and the premature rupture before reaching the ultimate stress expected that was 700 MPa as embodied in standard. It is seen by Karaca & Şimşir (2019) work that the material used by him exceeds the standard limits. This difference is relative to the nodular cast iron. This material has a great range in mechanical properties, varying the values depending on the casting process and material quality control.

An important difference between the properties obtained in the tests and the standard properties was noticed in this work. The tests performed reinforce the fact that there is a difference in nodular cast iron properties when obtained from small and medium-sized foundries, with respect to available standard data. This finding shows the importance of the present study with regard to this class of nodular cast iron materials.

6 CONCLUSION

The present work proposed the analysis and characterization of the commercial nodular cast iron in absence of heat treatment. The methodology aims to study the influence of the specimen geometry position in the NCI block in relation to the mechanical properties. It was also possible to analyze the material quality when cast in blocks or bars without using the block Y process. The study has also proposed a routine development capable to perform nodule count and characterization. In addition, the developed routine has also been able to count the phase content in each chemically-etched sample.

The methodology was based on the ASTM standards and in previous works. Previous works were used as a benchmark in order to compare the influence of the specimen position on mechanical properties.

NCI GGG40, GGG60, and GGG70 presented similar behavior during the tests. It was clear in the results that specimens removed from the edge have higher strength limits than others. This condition is explained by the fact that these areas have more graphite nodules, but with a smaller average size than the others.

The trend graph presents the relation between the nodule density and the ultimate stress. For all NCI classes analyzed herein, the behavior was similar with respect to the material tends to resist higher stress levels when the nodule density was greater. The increase in the number of nodules leads to a reduction in their size, thereby improving tensile, fatigue, and fracture properties. Inoculation methods used to increase the number of nodules usually make the nodules more spherical. Therefore, a high number of nodules are usually associated with improved nodularity. According to the literature, the higher the density of the nodules, the greater the strength and elongation capacity of the material. In the bar samples, even with a higher density of nodules, there was only an increase in the strength limit, indicating that this increase was enhanced by the pearlite structure identified in the samples.

The mechanical test performed has evidenced the importance of evaluating the NCI mechanical properties before the material application. It is important to highlight the strong influence of block Y casting methodology in NCI mechanical properties, especially in the capacity of resisting plastic deformations. NCI has a large variation in mechanical properties from one material to another. In this sense is evidenced the importance of evaluating the NCI batch before the material application. The cast conditions must be very well controlled in order to obtain a material with the specified properties.

The obtained results in this work show that the mechanical properties did not fully match

those available in the specific NCI standards. GGG40 in particular which has large elongations and lower yield strengths compared to the other NCI resulted in a small strain and high yield strength.

It was evidenced by the analysis that material cast in circular bars shapes have different mechanical properties than material cast in the block. The cooling rate is a preponderant factor in obtaining the desirable characteristics. The specimens cast in round bars have a higher pearlite percentage and higher hardness in pearlite and graphite due to the decrease in carbon diffusion.

The routine developed in MatLab was capable to quantify the phase content in each sample to help understand the different mechanical behavior between the samples. The routine also could quantify and characterize the graphite nodules in each sample. The graphite nodules are crucial elements in NCI characterization. In this way, the routine aided the trend graph elaboration and the material behavior interpretation in relation to nodule characteristics.

The Bauschinger effect helps to better understand the NCI behavior under cyclic conditions. One can note that compressive stress levels are less under cyclic conditions than the compressive standard limits. The values are near to tensile stress levels, while the material only compressed could reach twice the stress level. The Bauschinger effect has also concluded that the NCI tends to hardening under cyclic conditions.

Finally, it can be inferred that the methodology used in this work allows obtaining the NCI GGG40, 60, and 70 characteristics in absence of heat treatment and cast Y block procedure. The procedures aid the material behavior comprehension concerning the microstructure. The stipulated objectives were reached in addiction the developed routine that seems to be efficient in NCI characterizing will be available on the web.

6.1 FUTURE STUDY

Over the course preparation of this work, some topics arose that can be developed in future research.

- Development with the aid of artificial intelligence (convolutional neural networks, genetic algorithm) a model capable of estimating the material mechanical properties based on computational image analysis.

- Evaluate the mechanical properties and the influence of the specimen position in cast block considering high cycle fatigue.

- Study the different heat treatments and applications in NCI: impact in graphite nodules structure and microstructure characterization.

- Analyze the microstructure and mechanical properties of the NCI cast in block Y and the effect of alloy elements in NCI.

- Perform crack propagation and fracture toughness comparing the NCI classes and positions in a casted block, evaluating the nodule influence in fracture mechanics properties.

6.2 PRESENTED WORK

During the development period of this master thesis the following works have been developed.

- Application of discretization error estimators in stepped column buckling problems - Revista Internacional de Metodos Numericos para Calculo y Diseno en Ingenieria.

- Predição de crescimento de trinca por fadiga com carregamento de amplitude constante usando integração numérica. REVISTA INTERDISCIPLINAR DE PESQUISA EM ENGENHARIA.

- Análise numérica de vibrações em um pórtico com e sem protensão: Estudo de caso Grua treliçada. REVISTA INTERDISCIPLINAR DE PESQUISA EM ENGENHARIA.

- Error Interpolation for Reference Value Characterization for Complex Column Buckling Problems. In: XLI Ibero-Latin-American Congress on Computational Methods in Engineering (CILAMCE).

- Chaboche single model calibration for Bauschinger Effect. In: XLI Ibero-Latin-American Congress on Computational Methods in Engineering (CILAMCE)

- Richardson Error Estimator and Convergence Error Estimator applied in a buckling analysis by Finite Difference Method (FDM). In: XLI Ibero-Latin-American Congress on Computational Methods in Engineering (CILAMCE)

- Static Analysis and Optimization of stiffened plates under pressure loading. In: XLI Ibero-Latin-American Congress on Computational Methods in Engineering (CILAMCE)

- Respirador dinâmico com propriedades multifuncionais para impedir doenças infecciosas com propriedades de proteção autolimpante e drug delivery. 2021, Brasil. Patente: Privilégio de Inovação

REFERENCE LIST

Al-Ghonamy, A. I., Ramadan, M., Fathy, N., Hafez, K. M., e El-Wakil, A. A. (2008). Effect of Graphite Nodularity on Mechanical Properties of Ductile Iron for Waterworks Fittings and Accessories. *International Journal of Civil & Environmental Engineering*, 10(3):1–5.

Askeland, D. R., Fulay, P. P., e Wright, W. J. (2010). *The Science and Engineering of Materials*, volume 6.

ASTM A247 (2020). ASTM A247 - 17 Standard Test Method for Evaluating the Microstructure of Graphite in Iron Castings. páginas 1–13.

ASTM E2567 (2015). ASTM E2567 - Standard Test Method for Determining Nodularity And Nodule Count In Ductile Iron. i:4–7.

ASTM E3, A. S. (2012). Standard Guide for Preparation of Metallographic Specimens Standard Guide for Preparation of Metallographic Specimens. *ASTM International*, 03.01(July):1–12.

ASTM E394 (2017). Standard Test Method for Microindentation Hardness of Materials. *Annual book of ASTM Standard*, 14:1–24.

ASTM E606 (2013). Strain-Controlled Fatigue Testing 1. *ASTM Standards, E606*, 92(2004):1–16.

ASTM E8 (2010). ASTM E8/E8M standard test methods for tension testing of metallic materials 1. *Annual Book of ASTM Standards 4*, (C):1–27.

ASTM E92 (2017). Standard Test Methods for Vickers Hardness and Knoop Hardness of Metallic Materials BT - Standard Test Methods for Vickers Hardness and Knoop Hardness of Metallic Materials. i:1–27.

Audebert, N., Le Saux, B., e Lefèvre, S. (2017). Segment-before-detect: Vehicle detection and classification through semantic segmentation of aerial images. *Remote Sensing*, 9(4).

Behnam, J., Davami, P., e Varahram, N. (2010). Effect of cooling rate on microstructure and mechanical properties of gray cast iron. *Materials Science and Engineering: A*, 528(2):583 – 588.

Benedetti, M., Fontanari, V., e Lusuardi, D. (2019). Effect of graphite morphology on the fatigue and fracture resistance of ferritic ductile cast iron. *Engineering Fracture Mechanics*, 206(October):427–441.

Betancur, A., Anflor, C., Pereira, A., e Leiderman, R. (2018). Determination of the effective elastic modulus for nodular cast iron using the boundary element method. *Metals*, 8(8):1–17.

Bočkus, S., Venckunas, A., e Žaldarys, G. (2008). Relation between section thickness, microstructure and mechanical properties of ductile iron castings. *Medziagotyra*, 14(2):115–118.

Bulgarevich, D. S., Tsukamoto, S., Kasuya, T., Demura, M., e Watanabe, M. (2018). Pattern recognition with machine learning on optical microscopy images of typical metallurgical microstructures. *Scientific Reports*, 8(1):3–9.

Callister, W. D. e Rethwisch, D. G. (2009). *MATERIALS SCIENCE AND ENGINEERING AN INTRODUCTION*.

Ceschini, L., Morri, A., Morri, A., Salsi, E., Squatrito, R., Todaro, I., e Tomesani, L. (2015). Microstructure and mechanical properties of heavy section ductile iron castings: Experimental and numerical evaluation of effects of cooling rates. *International Journal of Cast Metals Research*, 28(6):365–374.

Çetinarslan, C. S. e Karaman Genç, S. (2014). Study in the variation of mechanical properties of nodular cast iron depending upon section thickness. *Materialwissenschaft und Werkstofftechnik*, 45(2):106–113.

Chaboche, J. L. (2008). A review of some plasticity and viscoplasticity constitutive theories. 24:1642–1693.

Chiaverini, V. (2008). *Aços e ferros fundidos*. Abm, São Paulo, 7 edição.

de Albuquerque, V. H. C., de Alexandria, A. R., Cortez, P. C., e Tavares, J. M. R. (2009). Evaluation of multilayer perceptron and self-organizing map neural network topologies applied on microstructure segmentation from metallographic images. *NDT and E International*, 42(7):644–651.

de Peixoto, F. M., de Rebouças, E. S., de Xavier, F. G. L., e Rebouças Filho, P. P. (2015). Desenvolvimento de um Software para cálculo da densidade de nódulos de grafita em ferro fundido nodular através de Processamento Digital de Imagens. *Revista Materia*, 20(1):262–272.

De Santis, A., Di Bartolomeo, O., Iacoviello, D., e Iacoviello, F. (2008). Quantitative shape evaluation of graphite particles in ductile iron. *Journal of Materials Processing Technology*, 196(1-3):292–302.

De Santis, A., Iacoviello, D., Di Cocco, V., e Iacoviello, F. (2017). Classification of ductile cast iron specimens: A machine learning approach. *Frattura ed Integrita Strutturale*, 11(42):231–238.

de Souza Neto, E. A., Peric, D., e Owen, D. R. (2008). *Computational methods for plasticity: theory and applications*. John Wiley & Sons.

Dowling, N. E. (2013). *Mechanical behavior of materials*, volume 1. Pearson Education Limited, fourth edição.

Fernandes, D. O. (2022a). Nci phase counter (`https://www.mathworks.com/matlabcentral/fileexchange/107659-nci-phase-counter`), matlab central file exchange. retrieved march 10, 2022.

Fernandes, D. O. (2022b). Nodule counter (`https://www.mathworks.com/matlabcentral/fileexchange/107654-nodule-counter`), matlab central file exchange. retrieved march 10, 2022..

Filho, P. P., da Silva Barros, A. C., Almeida, J. S., Rodrigues, J. P., e de Albuquerque, V. H. C. (2019). A new effective and powerful medical image segmentation algorithm based on optimum path snakes. *Applied Soft Computing Journal*, 76:649–670.

Gangasani, P. R. (2007). Evaluation of Fatigue strengths of continuously cast ductile irons. *International Journal of Metalcasting*, 1(1):41–55.

Gonzaga, R. A. (2013). Influence of ferrite and pearlite content on mechanical properties of ductile cast irons. *Materials Science and Engineering A*, 567:1–8.

Goodrich, G. (2003). Metallurgy of cast irons. *Iron castings engineering handbook, AFS, Prited in the United States of America*, páginas 47–61.

Greggio, N., Bernardino, A., e Santos-Victor, J. (2010). Image segmentation for robots: Fast self-adapting Gaussian mixture model. *Lecture Notes in Computer Science (including subseries Lecture Notes in Artificial Intelligence and Lecture Notes in Bioinformatics)*, 6111 LNCS(PART 1):105–116.

Grenier, S., Labrecque, C., Bhattacharjee, A., Gundlach, R., Kroka, B., e Riabov, M. (2014). Inter-laboratory study of nodularity and nodule count of ductile iron by image analysis. *International Journal of Metalcasting*, 8(2):51–63.

Guesser, W. L. (2019). *Mechanical properties of the cast iron*, volume 335. Blucher, São Paulo, 2 edição.

Guillemer-Neel, C., Bobet, V., e Clavel, M. (1999). Cyclic deformation behaviour and Bauschinger effect in ductile cast iron. *Materials Science and Engineering A*, 272(2):431–442.

Guillemer-Neel, C., Feaugas, X., e Clavel, M. (2000). Mechanical behavior and damage kinetics in nodular cast iron: Part I. Damage mechanisms. *Metallurgical and Materials Transactions A: Physical Metallurgy and Materials Science*, 31(12):3063–3074.

Guzel, E., Yuksel, C., Bayrak, Y., Sen, O., e Ekerim, A. (2014). Effect of section thickness on the microstructure and hardness of ductile cast iron. *Materialpruefung/Materials Testing*, 56(4):285–288.

Han, K., Van Tyne, C. J., e Levy, B. S. (2005). Effect of strain and strain rate on the Bauschinger effect response of three different steels. *Metallurgical and Materials Transactions A: Physical Metallurgy and Materials Science*, 36(9):2379–2384.

hua Wang, Z., Zhang, X., long Xu, F., cai Qian, K., e min Chen, K. (2019). Effect of nodularity on mechanical properties and fracture of ferritic spheroidal graphite iron. *China Foundry*, 16(6):386–392.

Hütter, G., Zybell, L., e Kuna, M. (2015). Micromechanisms of fracture in nodular cast iron: From experimental findings towards modeling strategies – a review. *Engineering Fracture Mechanics*, 144:118 – 141.

Iacoviello, F., Iacoviello, D., Di Cocco, V., De Santis, A., e D'Agostino, L. (2017). Classification of ductile cast iron specimens based on image analysis and support vector machine. *Procedia Structural Integrity*, 3:283–290.

Jiang, Y. e Zhang, J. (2008). Benchmark experiments and characteristic cyclic plasticity deformation. *International Journal of Plasticity*, 24(9):1481–1515.

Jost, B., Klein, M., Beck, T., e Eifler, D. (2017). Temperature dependent cyclic deformation and fatigue life of EN-GJS-600 (ASTM 80-55-06) ductile cast iron. *International Journal of Fatigue*, 96:102–113.

Karaca, B. e Şimşir, M. (2019). The effects of heat treatment on the tensile properties of camshaft made of GGG70 series spherical graphite cast iron. *Acta Physica Polonica A*, 135(4):811–818.

Karaman, S. e Çetinarslan, C. S. (2010). Manufacturing Process of GGG40 Nodular Cast Iron. *Unitech 10*, páginas 117–122.

Kelly, P. (2020). Mechanics lecture notes: An introduction to solid mechanics.

Keough, J. e Hayrynen, K. (2017). Heat Treatment of Malleable Irons. In *Cast Iron Science and Technology*. ASTM International.

Koerich, A. L. e Al-Rubaie, K. S. (2012). Efeito Combinado Do Antimônio E Cobre Nas. *ABM International Congress Proceedings*, páginas 975–989.

Kohout, J. (2001). A simple relation for deviation of grey and nodular cast irons from Hooke's law. *Materials Science and Engineering A*, 313(1-2):16–23.

Lee, Y. L. e Barkey, M. E. (2012). Fundamentals of Cyclic Plasticity Theories. *Metal Fatigue Analysis Handbook*, páginas 253–297.

Lemaitre, L. e Chaboche, J.-L. (1990). *Mechanics of solid materials*, volume 1.

Lemoine, X. e Aouafi, A. (2008). Bauschinger effect correspondence of experimental tests. *International Journal of Material Forming*, 1(SUPPL. 1):241–244.

Li, M., Zhang, T. H., Gan, C. H., e Liang, N. G. (2002). Hardness testing on surface layer of material and results analyzing contrastively. *Chinese Journal of Aeronautics*, 15(2):82–89.

Lou, Y. e Yoon, J. W. (2017). *Anisotropic ductile fracture criterion based on linear transformation*, volume 93.

Lucas, L., Boneti, T., Hupalo, M. F., Junior, S. V., e Rosário, A. M. (2017). Influence of casting heterogeneities on microstructure and mechanical properties of austempered ductile iron (ADI). (stage II).

Lukhi, M., Kuna, M., e Hütter, G. (2018). Numerical investigation of low cycle fatigue mechanism in nodular cast iron. *International Journal of Fatigue*, 113(April):290–298.

Malage, A., Rege, P. P., e Rathod, M. J. (2015). Automatic quantitative analysis of microstructure of ductile cast iron using digital image processing. *Metallurgical and Materials Engineering*, 21(3):155–166.

Mataya, M. C. e Carr, M. J. (1983). The Bauschinger Effect in a Nitrogen-strengthened Austenitic Stainless Steel. 57:205–222.

Meena, A. e El Mansori, M. (2012). Drilling performance of green austempered ductile iron (ADI) grade produced by novel manufacturing technology. *International Journal of Advanced Manufacturing Technology*, 59(1-4):9–19.

Megahed, H., El-Kashif, E., Shash, A. Y., e Essam, M. A. (2019). Effect of holding time, thickness and heat treatment on microstructure and mechanical properties of compacted graphite cast iron. *Journal of Materials Research and Technology*, 8(1):1188–1196.

Mocellin, F., Melleras, E., Guesser, W. L., e Boehs, L. (2004). Study of the Machinability of Compacted Graphite Iron for Drilling Process. *Journal of the Brazilian Society of Mechanical Sciences and Engineering*, 26(1):22–27.

Mohammadnezhad, M., Javaheri, V., Shamanian, M., Naseri, M., e Bahrami, M. (2013). Effects of vanadium addition on microstructure, mechanical properties and wear resistance of ni-hard4 white cast iron. *Materials & Design*, 49:888 – 893.

Pattillo, P. (2018). *Yield and Inelastic Behavior*.

Plumtree, A. (1987). Correlation between Microstructure and Cylic Behaviour. (6):19–30.

Prakash, P. (2011). Digital Microstructure Analysis System for Testing and Quantifying the Ductile Cast Iron. *International Journal*, 19(3):22–27.

Radzikowska, J. (2004). Metallography and microstructures of cast iron.

Rebouças, E. S., Braga, A. M., Marques, R. C., e Rebouças Filho, P. P. (2016). A new approach to calculate the nodule density of ductile cast iron graphite using a Level Set. *Measurement: Journal of the International Measurement Confederation*, 89:316–321.

Šamec, B., Potrč, I., e Šraml, M. (2011). Low cycle fatigue of nodular cast iron used for railway brake discs. *Engineering Failure Analysis*, 18(6):1424–1434.

S.Hiremath, P., Sadashivappa, A., e Pattan, P. (2014). Microstructure Image Analysis for Estimating Mechanical Properties of Ductile Cast Iron. *International Journal of Computer Applications*, 107(17):32–35.

Singh, R. (2016). Chapter 7 - cast iron. In Singh, R., editor, *Applied Welding Engineering (Second Edition)*, páginas 65 – 81. Butterworth-Heinemann, second edition edição.

Sofue, M., Okada, S., e Sasaki, T. (1978). High-quality ductile cast iron with improved fatigue strength. In *82 nd Annual Meeting*, páginas 173–182.

Souza, T. N. F., Nogueira, R. A. P. S., Franco, F. J. S., Aguilar, M. T. P., e Cetlin, P. R. (2014). Mechanical and microstructural characterization of nodular cast iron (nci) with niobium additions. *Materials Research*, 17(5):1167–1172.

Sparavigna, A. (2017). An image segmentation for the measurement of microstructures in ductile cast iron. *Philica*, 2017(1159).

Sund, T. e Eilertsen, K. (2003). An algorithm for fast adaptive image binarization with applications in radiotherapy imaging. *IEEE Transactions on Medical Imaging*, 22(1):22–28.

Toribio, J., Kharin, V., Ayaso, F. J., Lorenzo, M., González, B., Matos, J. C., e Aguado, L. (2020). Analysis of the bauschinger effect in cold drawn pearlitic steels. *Metals*, 10(1):21–23.

Vaško, A., Belan, J., e Tillová, E. (2019). Static and dynamic mechanical properties of nodular cast irons. *Archives of Metallurgy and Materials*, 64(1):185–190.

Vokál, V., Nilsson, K. F., e Minnebo, P. (2008). Characterization of defects and graphite types in ductile cast iron by image processing and its relation to mechanical properties. *Kovove Materialy*, 46(1):39–49.

Wilson, D. V. (1965). REVERSIBLE WORK HARDENING IN ALLOYS OF CUBIC METALS *. 13(July):807 814.

Ye, D., Matsuoka, S., Nagashima, N., e Suzuki, N. (2006). The low-cycle fatigue, deformation and final fracture behaviour of an austenitic stainless steel. *Materials Science and Engineering A*, 415(1-2):104–117.

Yescas-González, M. A. C. (2001). *Modelling the Microstructure and Mechanical Properties of Austempered Ductile Irons*. PhD thesis, University of Cambridge.